Sintering and electrical properties of proton conducting BSZCY151020

Synthesized via solid-state reactive sintering

Sjur Storhaug

Master Thesis
Inorganic Chemistry
60 credits

Department of Chemistry
Faculty of Mathematics and Natural Sciences

UNIVERSITY OF OSLO

06 / 2022

Preface

This thesis represents part of the required work for the degree of Master of Science (M.Sc.) at the Department of Chemistry, Faculty of Mathematics and Natural Sciences, University of Oslo. The work was carried out at the group of Electrochemistry under the supervision of Professor Reidar Haugsrud and Dr. Amir Masoud Dayaghi during the period from August 2020 to June 2022.

I would like to thank my main and co-supervisor Professor Reidar Haugsrud and Amir Masoud Dayaghi for the support and encouragement throughout my M.Sc. work. Thanks to all at electrochemistry for lending a helping hand when needed.

Tempus fugit

Oslo, June 2022

Sjur Storhaug

Abstract

In the present work $Ba_{0.85}Sr_{0.15}Zr_{0.7}Ce_{0.1}Y_{0.2}O_{3-\delta}$ have been extensively studied as an electrolyte contender with increased TEC for use in PCFCs. BSZCY151020 was fabricated by roll-mill mixing of precursors, followed by solid-state reactive sintering. The SSRS method is put under scrutiny by investigating effects of temperature, time and amounts of sintering additive on densification, microstructure, and proton concentrations. YSZ has also been investigated as a replacement for binary oxides in the starting mixture, with the hypothesis of increasing effective acceptor concentrations. Furthermore, AC characterisation in the form of EIS was used to obtain data for total-, bulk- and GB- conductivity in humid argon, dry air and under varying p_{O_2}. Which in turn were modelled with mobility expressions in combination with ionic charge carrier concentrations obtained by thermogravimetric analysis. In addition, EIS data were utilized to extract space charge potentials of grain boundaries with Schottky-barrier theory applied for protons.

Sintering additives in amounts of 1wt.% and 0.5wt.% revealed a small decrease with regards to proton conductivity, and a significant effect on densification. Furthermore, sintering profiles were investigated in combination with HT-XRD to expose phase transitions and reactions with and without YSZ, CuO and NiO.

Space charge phenomena were also estimated by means of solving Schottky-barriers for protons, where the potential was solved numerically. The dielectric loss (ε'') and its relation to dielectric loss tangent ($\tan(\delta)$) were briefly introduced and investigated with respect to relaxation phenomena in BSZCY151020. The contribution of energy loss was inherent grain boundary and bulk mechanisms, and their activation energies were extracted by Arrhenius expressions. The bulk association energies were proposed to be related to the relaxation of protons in relation to an yttria octahedra (trap).

Overall, this work contributes to several aspects in the understanding of electrochemical transport in BSZCY151020. However, the broadness of the study also reveals areas that need further investigation and understanding, such as dielectric loss and relaxation phenomena. In addition, small contributions to the understanding of SSRS have been made.

List of Abbreviations

BZY – Yttrium doped barium zirconate

BLM – Brick Layer model

YSZ – Yttria stabilized zirconate

XRD – X-ray Diffraction

HT-XRD – High temperature X-ray Diffraction

PDF – Powder diffraction file

SEM – Scanning electron microscopy

GB – Grain boundary

Harmix – 5% H_2 / Argon mixture

TG – Thermogravimetry

SSRS – Solid-state reactive sintering

SSR – Solid state reaction

TEC – Thermal expansion coefficient

PCFC – Proton ceramic fuel cell

SOFC – Solid oxide fuel cell

Table of Contents

1 Introduction

1.1 Background & Motivation

The climate crisis is this generations great challenge, it poses a series of necessary changes from everyday life to global energy transition to reach the goal of the Paris agreement. This involves replacing fossil fuels with circular energy carriers that can fulfil the same needs in transportation, energy storage and overall energy safety. As of today, batteries are the main source of storing energy for later use, for example for computers, phones, and cars. However, batteries have not proven to be efficient for storing large quantities of energy and the technology is not transparent enough to replace fossil fuels. Hydrogen conversion technologies however have the luxury of excluding the fuel itself from the operating cell, which means that it can be stored in steel tanks, solids or as a cryogenic liquid. This a property that we are accustomed to from fossil fuels, they are relatively light, meaning easy to transport and suitable for use in vehicles. The crux of the matter is that we are not limited to one state of hydrogen but can apply different compounds with high hydrogen content in a circular energy system with few technological adjustments. This includes energy carriers such as hydrogen gas, ammonia, or hydrocarbons. A major benefit is that hydrogen can be produced by electrolysis of water from renewable energy sources, and when the energy is extracted there is no pollution since water is the sole residual product. To retrieve the energy stored in hydrogen gas, fuel cells have proven to be the most efficient technology. Solid oxide fuel cells are a subgroup which is highly relevant.

In general terms, a fuel cell converts chemical energy into electric energy without combustion. Specifically, for hydrogen fuel cells, research has been focused on solid oxide materials as fuel cells with an oxide as the electrolyte. Ideally the electrochemical cells operate at temperatures between 300 and 500 °C and are amongst the most viable fuel cell technologies [1]. Solid oxide fuel cells (SOFCs) can be categorized according to the ionic charge carrier of fuel cell electrolyte, oxide ion conducting and proton ceramic fuel cell (PCFC)[2]. The latter will be the focus in the present master project.

A fuel cell consists of two key components: the electrolyte and the electrodes. The electrodes, the positrode and negatrode, need different transport properties pending on the type of fuel cell, but should generally be a mixed ion-electron conductor. For a PCFC, the electrolyte material needs to exhibit high proton conductivity since protons from hydrogen at the anode, migrate through the electrolyte, and react with oxygen at the cathode. The electrons pass through the

external circuit in the opposite direction. A PCFC is illustrated in Figure 1 with applicable electrode reactions.

For each of these components there is a range of parameters that must be optimized to create an efficient PCFC. The components in the fuel cell assembly are in direct contact meaning their thermal properties should be equal posing little strain on the interface. One challenge is therefore to develop materials with the required transport properties, where the thermal expansion coefficient is relatively close for the individual components. The latter is essential to avoid stress at the component interfaces upon thermal cycling leading to crack formation and delamination. Yttrium doped $BaZrO_3$ (BZY) has proven to be a contender as an electrolyte for PCFCs because of its high proton conductivity at intermediate temperatures (400-600°C). However, BZY has significantly lower TEC than state of the art electrode materials, making the interconnection between the electrolyte and electrode fragile and resulting in cell cracking under thermal cycling and at operating temperatures. Consequently, it is desirable to develop cathode candidates with lower TEC or alternatively to increase the TEC of BZY without degrading the functional properties, or both.

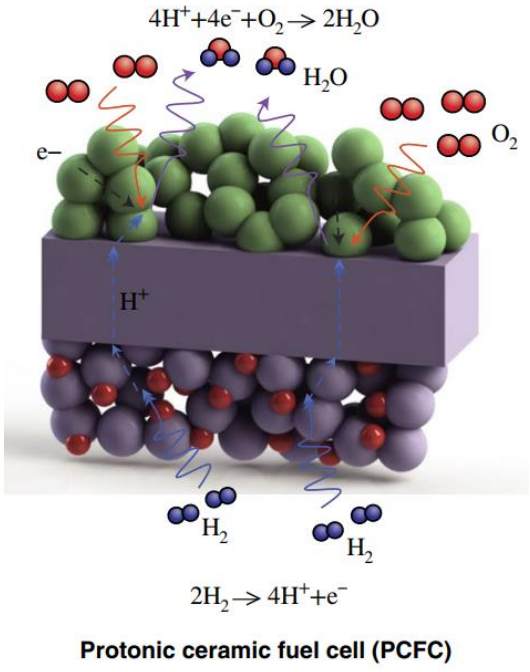

Figure 1: Proton ceramic fuel cell, with anode (bottom), electrolyte (middle) and cathode (top) [3].

1.2 Aims & contents

During recent years, a new electrolyte composition has been developed by the electrochemistry group based on BZY, where the TEC has been increased compared to BZY. The increased TEC was achieved by substituting some of the Ba and Zr with Sr and Ce, respectively [4]. The actual composition is $(Ba_{0.85}Sr_{0.15})(Zr_{0.7}Ce_{0.1}Y_{0.2})O_{2.9}$ (BSZCY151020). The transport properties of this composition have so far not been widely investigated. Accordingly, there is a need for detailed knowledge and understanding of the defect chemistry and transport properties of this composition. A further comparison with other BZY based materials published in the literature is also necessary. Literature on the electrical conductivity of BZY based materials has revealed relatively large variations in the proton conductivity with composition, synthesis, and fabrication, and also more recently with the addition of sintering aid. The solid-state reactive sintering method, which has proven reliable for the production of dense proton ceramics, will be used for means of fabrication. The effects of sintering additives have been studied for BZY variants, which show that hydration and conductivity decrease relative to the pristine compositions [5-7]. Thus, the disadvantages of sintering additives will be evaluated for BSZCY151020.

The original composition (BSZCY151020) with and without the use of NiO and CuO as sintering aid will be synthesized and characterized. Moreover, precursor mix, sintering time and temperature will be evaluated by means of hydration studies to determine effects on proton concentration. A matrix of samples with different additive concentrations and sintering parameters will therefore be synthesised according to the one temperature step, SSRS method. TG is used to extract enthalpies and entropies of hydration, while SEM is used to describe the microstructure and thus possible segregations, grain size and grain boundaries. It has been observed that the conductivity of electrolyte materials containing sintering aid generally is lower and with relatively higher contributions of p-type electronic conductivity in the temperature window of operation for PCFCs [8]. Contributing to outline these disadvantages with the addition of sintering aids will be in focus during the investigation.

The experiments will form the basis to derive thermodynamic and transport parameters that represent the material properties. These can be compared to the corresponding parameters for other BZY-based electrolytes. This will serve as a means to evaluate the electrolyte candidates and can together with the data on thermal expansion [4] be important for the choice of electrodes, give strategies to which stoichiometry and synthesis route is the better, and which potentially would produce the most viable PCFC electrolyte candidate.

The general goal is to derive conductivity models for this electrolyte contender, outlining transport numbers, mobilities and formation thermodynamics of the different charge carriers.

Newer and deeper theoretical aspects of proton conductors will also be touched upon, respectively trapping of protons at yttrium octahedra [9] and grain boundary space charge layers [10].

2 Theory

2.1 Defect chemistry

Defect chemistry explains irregularities in a periodic crystalline structure. Defects are categorised according to their dimension: zero-, one- and two-dimensional defects, which relates to point defects, line defects and plane defects (grain-boundaries), respectively. All defect reactions must follow the three laws of neutrality or balance: conservation of mass, conservation of charge and conservation of the ratio of structure sites.

2.1.1 Kröger Vink

The Kröger Vink notation is specifically tailored to describe reactions of point defects in equilibriums with the surroundings. The element or vacancy (v) in question, has an effective charge (superscript), either positive ($\cdot$), negative ($'$) or neutral (x). Its position (subscript) is either on a structural site or an interstitial site (i). In general:

$$Species_{site}^{effective\ charge} \tag{2.100}$$

Intrinsic electronic defects are also included as e and h, electrons and holes.

2.1.2 Associated defects in proton conductors

Barium zirconate is substituted with a lower valence cation on the B-site to induce defect properties that enhance proton conducting abilities. Doping yttrium on B-site in barium zirconate introduces an effective negative charge which is compensated by oxygen vacancies in dry conditions at intermediate temperatures. The substitution can be presented in Kröger-Vink notation as:

$$Y_2O_3 = 2Y_{Zr}' + 3O_O^x + v_O^{\cdot\cdot} \tag{2.101}$$

Here Y_{Zr}' is yttrium on zirconium site with the effective charge of -1, O_O^x an oxide ion on an oxygen site with neutral charge, and $v_O^{\cdot\cdot}$ is a vacancy on an oxygen site with an effective charge of +2.

Under humid atmospheres the oxygen vacancy absorbs hydroxide ions from water, while the remaining proton becomes associated with another oxide ion:

$$H_2O_{(g)} + O_O^x + v_O^{\cdot\cdot} = 2OH_O^{\cdot} \tag{2.102}$$

In addition to its ionic contribution, an oxide such as BZY will exhibit electronic defects such as holes and electrons. These electronic defect concentrations are most prominent at, respectively high and low partial pressures of oxygen.

At high partial pressure of oxygen, annihilation of vacancies by introduction of oxygen is charge compensated by holes:

$$v_O^{\cdot\cdot} + \frac{1}{2}O_{2(g)} = O_O^x + 2h^{\cdot} \tag{2.103}$$

While at low partial pressure of oxygen, the introduction of more vacancies is charge compensated by electrons:

$$O_O^x = \frac{1}{2}O_{2(g)} + v_O^{\cdot\cdot} + 2e' \tag{2.104}$$

These are respectively oxidation and reduction reactions.

The equilibrium coefficient of all reactions is then given as any other chemical equilibrium. Firstly, the hydration reaction from (2.101):

$$K_{hydr} = \frac{[OH_O^{\cdot}]^2}{[O_O^X][v_O^{\cdot\cdot}]p_{H_2O}} = \frac{X_{OH}^2}{X_O X_v p_{H_2O}} \tag{2.105}$$

Here the concentration of water vapour is given by the partial pressure of water, p_{H_2O}, while the rest is given by molar concentrations [] or site fractions X_i.

While the oxidation (2.103) and reduction (2.104) reaction contain partial pressure of oxygen, p_{O_2}, and p and n as holes and electrons, which is equivalent to $h^{\cdot}$ and e'.

$$K_{ox} = \frac{[O_O^x]p^2}{[v_O^{\cdot\cdot}]p_{O_2}^{\frac{1}{2}}} \tag{2.106}$$

$$K_{red} = \frac{[v_O^{\cdot\cdot}]p_{O_2}^{\frac{1}{2}}n^2}{[O_O^x]} \tag{2.107}$$

To retrieve atmospheric dependencies for water vapour and oxygen partial pressure, the above-mentioned reactions can be solved by assuming that one of the defects is dominating. The derivation for oxidising conditions in dry atmosphere will be included here, the rest are presented in Brouwer diagrams at the end of this chapter.

Under oxidising and dry condition's reaction (2.103) is applicable and either oxygen vacancies or holes will be the dominating compensating defect:

$$[Y'_{Zr}] = 2[v_O^{\cdot\cdot}] + p \tag{2.108}$$

Assuming vacancies are dominating and have a much higher concentration than holes the electroneutrality can be simplified:

$$[Y'_{Zr}] \approx 2[v_O^{\cdot\cdot}] \gg p \tag{2.109}$$

The limiting electroneutrality condition applies for the equilibrium expression (2.106), which can be solved for the majority and minority defect. The majority defect is given by:

$$2[v_O^{\cdot\cdot}] = [Y'_{Zr}] = constant \tag{2.110}$$

Oxygen vacancies are only limited by the constant yttrium content, according to the electroneutrality. While the minority defect is given by the solution of the equilibrium expression:

$$p = K'_{ox}[v_O^{\cdot\cdot}]^{\frac{1}{2}}[O_O^x]^{-\frac{1}{2}}p_{O_2}^{\frac{1}{4}} \tag{2.111}$$

Where the marked equilibrium coefficient is a simplification of $K'_{ox} = K_{ox}^{\frac{1}{2}}$. In this instance the equilibrium expression is unchanged, and the hole concentration is proportional to the power of ¼ of partial pressure of oxygen, or ¼ to logarithmic partial pressure of oxygen:

$$p \propto \frac{1}{4}\log\left(p_{O_2}\right)$$

Now assuming holes are dominating:

$$[Y'_{Zr}] \approx p \gg 2[v_O^{\cdot\cdot}] \tag{2.112}$$

The equilibrium equation then yields the dependencies:

$$[Y'_{Zr}] = p = constant \tag{2.113}$$

$$[v_O^{\cdot\cdot}] \propto -\frac{1}{2}\log\left(p_{O_2}\right) \tag{2.114}$$

The dependencies for partial pressure of oxygen in humid and dry conditions are presented in Figure 2, with arbitrary units of log(pO_2) and log(defects). Similarly, water vapour

dependencies are presented in Figure 3 with log(pH_2O). All logarithmic dependencies are solved by assuming limiting conditions for the electroneutrality on each equilibrium expression for the different reactions (hydration, oxidation, and reduction). The assumed dominating defect are indicated in each column of the figures below.

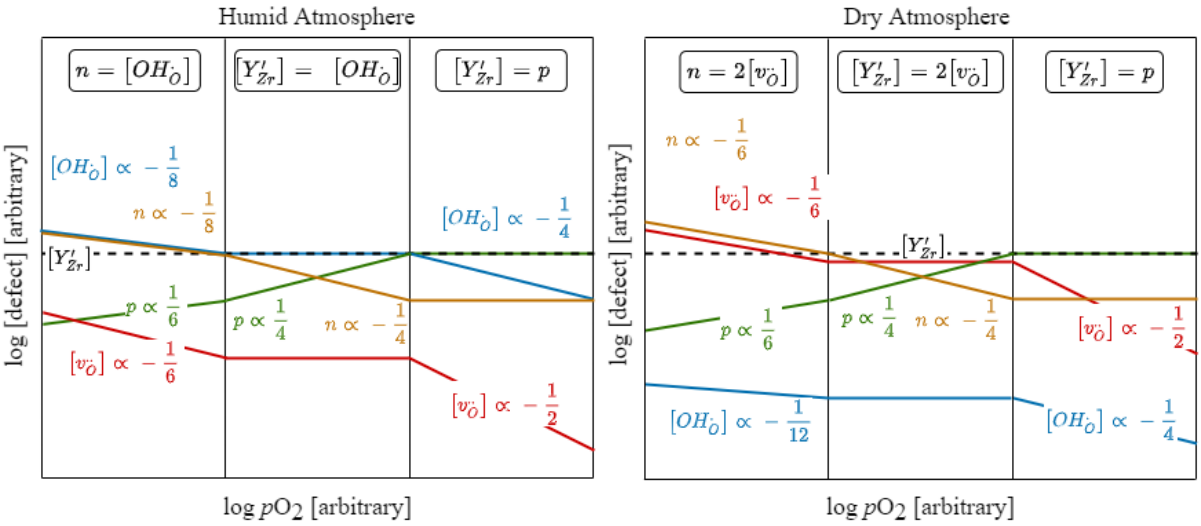

Figure 2: Brouwer diagram with log(pO_2) vs log(defect) with arbitrary units for humid and dry conditions.

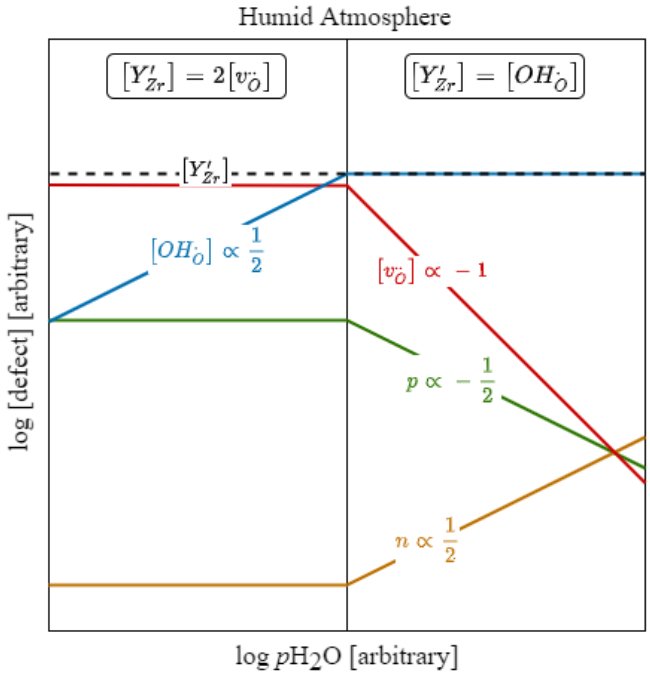

Figure 3: Brouwer diagram with log(pH_2O) vs log(defect) with arbitrary units for humid atmosphere.

2.1.3 Unwanted point defects

There are several unwanted defects that could affect the charge carrier defect concentrations. Most known is the issue of barium loss due to high volatility at higher temperatures in BZY. The other focus will be the introduction of point defects because of sintering additives. Further elaboration will be done in the literature part and are briefly presented here.

Barium is known to be volatile at high temperatures. It also suffers from poor stability under high pressures of carbon dioxide and water, forming respectively, carbonates and hydroxides. The problem of barium loss is therefore inherent to the high sintering temperatures. Where it either does not fully incorporate into the structure or is annihilated from it. The annihilation can be presented as:

$$Ba_{Ba}^{x} = v_{Ba}'' + 2h^{\cdot} + Ba \tag{2.115}$$

Or:

$$Ba_{Ba}^{x} + O_{O}^{x} = v_{Ba}'' + v_{O}^{\cdot\cdot} + BaO \tag{2.116}$$

The case is then barium deficiency and in what degree barium vacancies attribute decreased oxygen vacancy concentration and as a result decrease of proton concentration.

Sintering additives are in this thesis incorporated as additives and not doping. This means that there is a surplus of cations which may dissolve into the grain interior of the perovskite or segregate as a secondary phase. Another option is the segregation of cations into the grain boundaries, which have a more disordered defect chemistry than the grain interior.

A representation could be the incorporation of nickel at the interstitial sites of octahedral holes:

$$v_{i}^{x} + NiO = Ni_{i}^{\cdot\cdot} + 2e' + O_{O}^{x} \tag{2.117}$$

The same mechanism could apply with copper as sintering additive:

$$v_{i}^{x} + CuO = Cu_{i}^{\cdot\cdot} + 2e' + O_{O}^{x} \tag{2.118}$$

These interstitials could associate with yttrium cations and form neutral defect pairs that prohibit the formation of the compensating defects.

Another possibility is that the cations go to the A- or B- site in the structure. From the ionic radius in Table 1 it seems more likely that the Ni and Cu cations would occupy the B-site.

Table 1: Ionic radius for selected atoms with specified charge and coordination number gathered from [11], *closes CN for the applicable situation.

Cation (site)	Charge	CN	Ionic Radius (Å)
Ba (A)	2	12	1.61
Sr (A)	2	12	1.44
Zr (B)	4	8	0.84
Ce (B)	4	8	0.97
Y (B)	3	8	1.019
Ni	2	6*	0.83
Cu	2	6*	0.73

If we assume that Ni and Cu have the 2+ oxidation state. The ionic radius suggest that Ni and Cu would probably dissolve into the B-site. The following reactions are therefore proposed:

$$NiO = Ni''_{Zr} + O_O^x + \frac{1}{2}v_O^{\cdot\cdot} + h^{\cdot} \quad (2.119)$$

$$NiO + Y_2O_3 = Ni''_Y + 2Y_{Ba}^{\cdot} + 4O_O^x \quad (2.120)$$

$$CuO = Cu''_{Zr} + O_O^x + \frac{1}{2}v_o^{\cdot\cdot} + h^{\cdot} \quad (2.121)$$

$$CuO + Y_2O_3 = Cu''_Y + 2Y_{Ba}^{\cdot} + 4O_O^x \quad (2.122)$$

Here nickel and copper cations substitute yttrium or zirconium in the lattice which might cause segregation or displacement of functional atoms.

2.2 Electro chemistry

2.2.1 Electrical conductivity

Any charged species $z_i e$ (charge x elementary charge) within an electrical field E have the potential U to move according to the force F the field applies on the species. The ability for a charged species to move accordingly and create a current I is defined as its conductivity. The species can be electrons in the conduction band of a metal, or an ion diffusing through the structure of an oxide. The conductivity of any species i is:

$$\sigma_i = z_i e c_i u_i \tag{2.200}$$

Where c_i is concentration and u_i mobility of species i.

The concentration can also be defined as a unitless fractions in function of the oxygen density (molar density) of the material. Which will be the approach in this thesis. The oxygen density ρ_O is the theoretical density (ρ) per molar mass (Mm) of the material in question. Then conductivity is defined as:

$$\sigma_i = F\frac{\rho_{theoretical}}{Mm}c_i u_i = F\rho_O c_i u_i \tag{2.201}$$

where Faradays constant gives the charge carried per mole.

The total conductivity is the sum of all the partial conductivities:

$$\sigma_{tot} = \sum_i z_i e c_i u_i \tag{2.202}$$

More specific for a mixed electronic ionic conductor:

$$\sigma_{tot} = \sigma_{ion} + \sigma_{el} = \sigma_c + \sigma_a + \sigma_n + \sigma_p \tag{2.203}$$

Here c, a, n and p index the partial conductivities of respectively cations, anions, electrons and holes. The ratio of the species contribution to the total conductivity gives the transport number for said species, *i*:

$$t_i = \frac{\sigma_i}{\sigma_{tot}} \tag{2.204}$$

The correlations between diffusion (D_i), mobility (u_i) and conductivity (σ_i) are given by the Nernst-Einstein relation:

$$D_i = \frac{u_i k_b T}{z_i e} = \sigma_i \frac{k_b T}{c_i (z_i e)^2} \tag{2.205}$$

The Arrhenius expression expresses the temperature dependence for diffusion:

$$D_i = D_i^0 e^{-\frac{E_a}{k_B T}} \tag{2.206}$$

The activation barrier for an ionic charge carrier, such as protons or vacancies (oxide ions) [1], constitute both the enthalpy of formation and mobility. I.e., for a proton to move in the lattice it must first be there (formation) and then be able to move (mobility). The pre-exponential (D_0) therefore constitutes the entropy of formation and mobility, and the activation energy is given by the summation of enthalpies within the exponent. Accordingly, (2.206) can be expressed as:

$$D_0 = \alpha a_0^2 v \, e^{\frac{\Delta S_f + \Delta S_m}{R}} e^{\frac{\Delta H_f + \Delta H_m}{RT}} \tag{2.207}$$

Where α is a geometrical factor, a_0 is the lattice parameter, and v the vibration frequency. Using the Nernst-Einstein relation (2.205) Arrhenius expressions for mobility (u_i) and conductivity (σ_i) can be derived:

$$\sigma_i = \sigma_0 \frac{1}{T} e^{-\frac{\Delta H_a}{RT}} \tag{2.208}$$

$$u_i = u_0 \frac{1}{T} e^{-\frac{\Delta H_a}{RT}} \tag{2.209}$$

These expressions contain an extra temperature factor relative to that of diffusion, which is factored into the conductivity and mobility data to obtain linear equations that can be fitted. Here conductivity is used as an example:

$$\ln(\sigma_i T) = \ln(\sigma_0) - \left(\frac{\Delta H_a}{R}\frac{1}{T}\right) \tag{2.210}$$

Or by the 10th logarithm, with the relation $\ln(x) = \log(x)\frac{1}{\log(e)}$:

$$\log(\sigma_i T) = \log(\sigma_0) - \log(e)\left(\frac{\Delta H_a}{R}\frac{1}{T}\right) \tag{2.211}$$

These equations follow the linear trend:

$$y = -ax + b, where\ x = \frac{1}{T} \tag{2.212}$$

[1] Vacancies and oxide ions are proportional charge carriers as they follow the same mechanism of diffusion or jumps to portray a conductivity or current. I.e., oxide ions jump to a vacancy will the vacancy goes the opposite direction.

The pre-exponentials then also follow the Nernst-Einstein relation and gives temperature dependent sets for both conductivity and mobility:

$$u_0 = D_0 \frac{z_i e}{k_B} \tag{2.213}$$

$$\sigma_0 = D_0 \frac{c_i z_i^2 e^2}{k_B} \tag{2.214}$$

$$\sigma_0 = u_0 c_i z_i e \tag{2.215}$$

Their units are presented in Table 2.

Table 2: Pre exponential units for diffusion, mobility, and conductivity.

Pre-exponential	**Units**
D_0	$cm^2\ s^{-1}$
u_0	$cm^2 K\ V^{-1} s^{-1}$
σ_0	$S\ K\ cm^{-1}$

Considering equation (2.207) and (2.208) when the species i has a frozen concentration allows for some simplifications. When concentration is constant the formation enthalpy for species, i, does not contribute to the activation barrier or the pre-exponential. Then the exponent in expression (2.208) is simply:

$$\Delta H_a = \Delta H_m \tag{2.216}$$

And the activation enthalpy of mobility is the sole activation energy that the charge carrier must overcome. For the Arrhenius equations the linear extraction than yields the enthalpy of mobility.

$$\sigma_i = \sigma_i^0 \frac{1}{T} e^{-\frac{\Delta H_{i,m}}{RT}} \tag{2.217}$$

The defect theory and the above listed formulas make up the basis of the theoretical aspect for investigating electrochemical transport properties. Going forward in the thesis

electrochemical aspects revolve around this basis and are narrowed down to be precise and applicable for the measurement techniques used for the material in question.

2.2.2 Brick layer model

The Brick Layer model aims to standardise the observed conductivity for grain boundaries according to the applicable microstructural situation. Conductivity will always be standardised, as it is specific according to the area and length of the conductor. However, to get comparable results the conductivity of especially grain boundaries must be extracted in comparison to the microstructural case. For example, measuring two equal compositions of BZY20 with different grain size distribution and grain boundary width will affect the data collected, making the dataset incomparable. The Brick Layer Model (BLM) is based upon the works of Bauerle [12], Beekmans and Heyne [13], and was named by Burggraaf et al. [14]. Here the applicable theory is presented with inspiration from a paper by Haile et al. [15].

The model assumes that a sample with length L and with symmetrical electrodes with area A (or current collectors) constitutes of perfect cubic grains, and vertical and horizontal grain boundaries, respectively oriented in series and parallel. The model is reconstructed into a two dimensional illustration in Figure 4, reconstructed from Haile et al. [15].

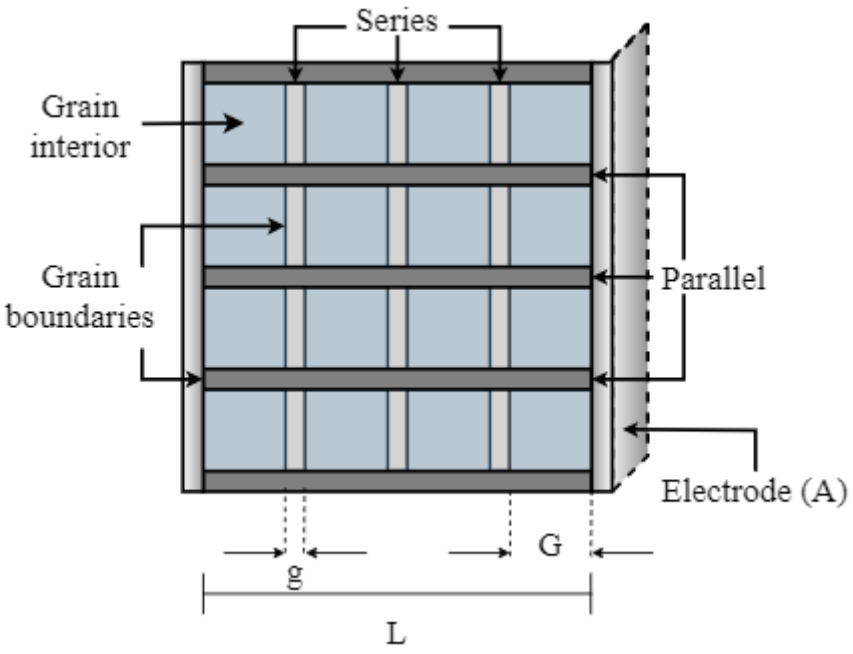

Figure 4: Two-dimensional illustration of the Brick layer Model (BLM).

The small g is the mean diameter of the GB, the big G is the mean diameter of the grains, A is the area of the electrode, and L is the length of the sample. The resistances of bulk and grain boundary are in series and can be summed together by the inverse resistances:

$$\frac{1}{R_{tot}} = \frac{1}{R_{bulk}} + \frac{1}{R_{gb}} \tag{2.218}$$

Assuming that the transport of protons is similar in the grain interior and parallel grain boundaries the contribution of high frequency resistor is comprised of the two:

$$\frac{1}{R_{Hf}} = \frac{1}{R_{gb\parallel}} + \frac{1}{R_{bulk}} = \frac{A}{L}\left\{\frac{2g}{G}\sigma_{gb} + \sigma_{bulk}\right\} \tag{2.219}$$

For the low frequency resistor, the contribution is from the GB in series:

$$\frac{1}{R_{Lf}} = \frac{1}{R_{gb\perp}} = \frac{A}{L}\left\{\frac{G}{g}\sigma_{gb}\right\} \tag{2.220}$$

The rather tangled situation for the high frequency resistor can be simplified. In a normal case, *case 1* [15], the bulk conductivity will be much higher than that of the grain boundaries which means the sample under investigation must have relatively large grains in relations to the grain boundaries. In simple terms, the sample is well sintered, dense with large grains. Mathematically:

$$\sigma_{bulk} > \sigma_{gb} \rightarrow\ g \ll G \tag{2.221}$$

If bulk conductivity is much higher than that of GB, in other words the resistance is much lower, the expression in (2.219) can be simplified to:

$$\frac{1}{R_{Hf}} = \frac{1}{R_{bulk}} = \frac{A}{L}\sigma_{bulk} \tag{2.222}$$

Now introducing the same simplification for the capacitances related to the high and low frequency resistors.

$$C_1 \approx C_{bulk} = \frac{A}{L}\varepsilon_{bulk}\varepsilon_0 \tag{2.223}$$

$$C_2 \approx C_{gb\perp} = \frac{A}{L}\frac{G}{g}\varepsilon_{gb}\varepsilon_0 \tag{2.224}$$

Here ε is the relative dielectric constant and ε_0 is the permittivity of vacuum. Depending on the electrolyte material, bulk and GB resistances can vary by several orders of magnitude, the dielectrics vary less significantly. Another simplification can thus be made by assuming that $\varepsilon_{bulk} \sim \varepsilon_{gb}$. Then expression (2.223) and (2.224) can be put together and solved to the expression:

$$\frac{C_1}{C_2} \approx \frac{C_{bulk}}{C_{gb}} = \frac{g}{G} \tag{2.225}$$

Which expresses that the ratio of capacitances should equal the ratio of mean GB diameter over mean grain interior diameter. This makes (2.220) solvable by using the capacitance ratio as a means to determine σ_{gb}.

$$\sigma_{gb.s} = \frac{g}{G}\sigma_{gb} \approx \frac{C_1}{C_2}\sigma_{gb} \tag{2.226}$$

An important thing to notice is the inconsistency in literature to report σ_{gb} as proposed over. Often σ_{gb} is represented only as the extracted value, not corrected with the capacitance ratio. In this thesis both values are shown for better comparison, where the values corrected by BLM is called $\sigma_{gb.s}$ (specific) and the not corrected values are presented as σ_{gb}.

2.2.3 Space charge potential

The grain boundary is a metastable 2-dimensional[2] extended defect. It is a result of insufficient configurational entropy (negative) in relation to positive formation enthalpy, which forces ions into a metastable disordered phase [16]. The extended defect of GB is therefore not chemically neutral with the bulk region and will in general exhibit the constraints of being electrostatically charged. The charge difference between bulk and the grain boundary is the origin of the space charge layer and the associated potential barrier between bulk and the GB core.

The knock-on effect of the potential difference is diffusion of vacancies and dopants from the space charge zone, which extends into the bulk region with distance λ^*. This solid-solid interface has the same characteristics of a solid-liquid interface typically explained by the Stern-Helmholtz model. A strong polarization of charge with a correlating diffusion layer caused by an electrostatic potential. The basis of the solid-solid interface in this thesis follows De Souza's

[2] In literature the grain boundary is sometimes considered as a 3-dimensional defect, this is a definition problem and not inherent to the theory itself.

approach based around the grain boundary for $SrTiO_3$ [17], and Christian Kjølseth et al. reiteration for $BaZr_{0.9}Y_{0.1}O_{3-\delta}$ [10].

Regarding the grain boundary core some simplifying assumptions can be made: It is homogenous with regards to charge and defects, and it has a physical width, w_c.The core is also considered to be positively charged [18].

The core is the reference point at $x = 0$, while bulk is $x = \infty$. The width of the space charge zone is λ^*. Figure 5 displays the space charge layers in relation to the grain boundary core.

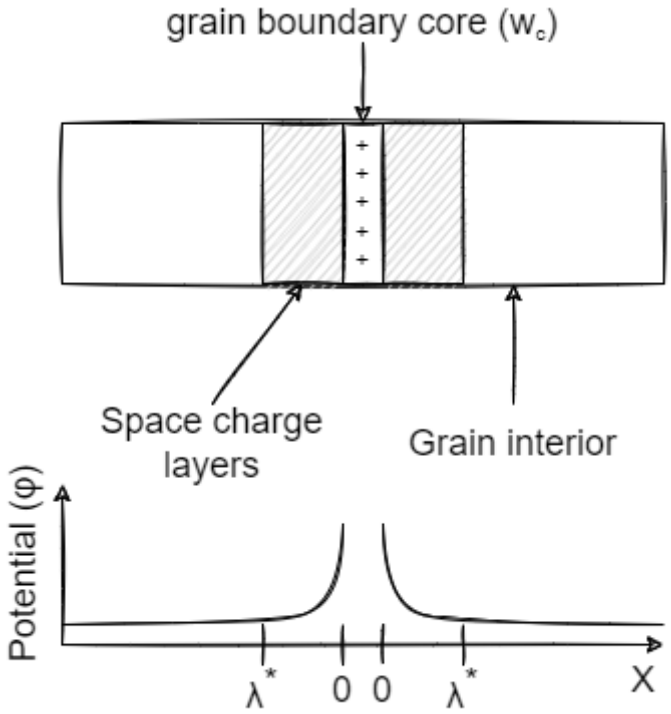

Figure 5: Space charge layers extending into bulk because of charge difference between positively charged GB core and neutral grain interior.

The derivation of the space charge layer in this thesis is considered in relation to protons. We therefore consider the mobile proton as a function of position (x) in the space charge region. The electrochemical potential of such a proton can be described by the chemical and electrical part. Here assuming an ideal solution for the chemical potential:

$$\mu_i^{ideal} = \mu_i^0 + k_B T ln(c_i) \tag{2.227}$$

The electrochemical potential is then given as:

$$\eta_{H^+}(x) = \mu_{H^+}^0 + k_b T ln\big(c_{H^+}(x)\big) + e\varphi(x) \tag{2.228}$$

Here μ^0 is the standard chemical potential of protons, c_{H^+} is the proton concentration and $\varphi(x)$ the electrostatic potential as a function of position (x) in the space charge region.

The limit of the space charge region is the grain interior where electrostatic potential is neutral and follows the bulk arrangement of atoms. This limit is defined as $x = \infty$, here the electrochemical potential of protons is given as:

$$\eta_{H^+}(\infty) = \mu^0_{H^+} + k_b T ln\big(c_{H^+}(\infty)\big) + e\varphi(\infty) \tag{2.229}$$

Where proton concentration is the same as nominal solution for the defect as a function of hydration thermodynamics, $c_{H^+}(\infty) = [OH_O^{\cdot}]$, and then electrostatic potential is $\varphi(\infty) = 0$.

Defining the difference in electrostatic potential as an expression of the equilibrium of electrochemical potential, $\eta_{H^+}(x) = \eta_{H^+}(\infty)$, gives:

$$\Delta\varphi(x) = \varphi(x) - \varphi(\infty) \tag{2.230}$$

Solving expression (2.228) and (2.229) according to equilibrium then gives the change in electrostatic potential:

$$\Delta\varphi(x) = \frac{k_b T}{e} \ln\left(\frac{c_{H^+}(\infty)}{c_{H^+}(x)}\right) \tag{2.231}$$

Assuming protons in bulk and GB have equal mobility, the term $\sigma_{H^+} = z_{H^+} e c_{H^+} u_{H^+}$ can be used to express (2.231) in conductivity:

$$\frac{c_{H^+}(\infty)}{c_{H^+}(x)} = \frac{\sigma_{bulk}}{\sigma_{gb.s}} = \exp\left(\frac{e\Delta\varphi(x)}{k_b T}\right) \tag{2.232}$$

To extract the apparent value over the whole region, which amounts to the potential at $x = 0$, the expression is integrated over the space charge layer length λ^*:

$$\frac{\sigma_{bulk}}{\sigma_{gb.s}} = \frac{1}{\lambda^*} \int_0^{\lambda^*} \exp\left(\frac{e\Delta\varphi(x)}{k_b T}\right) \tag{2.233}$$

Which is solved by Guo et al. [18] for an oxide ion conductor by assuming Mott Schottky approximation, i.e. the acceptor dopant is constant up to the grain boundary core. This requires solving (2.231) by the Poisson equation, which will not be presented here but can be found in the reference. The solution is:

$$\frac{\sigma_{bulk}}{\sigma_{gb.s}} \cong \exp \frac{\left(\frac{e\Delta\varphi(0)}{k_b T}\right)}{\left(\frac{2e\Delta\varphi(0)}{k_b T}\right)} \tag{2.234}$$

In this thesis a numerical solution is used with the conductivities obtained from EIS at each temperature to extract $\Delta\varphi(0)$. Additionally, the space charge length can be obtained for the corresponding potential barrier ($\Delta\varphi(0)$) from the Debye length (L_D):

$$\lambda^* = 2L_D \left(\frac{e\Delta\varphi(0)}{k_B T}\right)^{\frac{1}{2}} \tag{2.235}$$

Where the Debye length is given by:

$$L_D = \left(\frac{k_B T \varepsilon}{2e^2 c_y(\infty)}\right)^{\frac{1}{2}} \tag{2.236}$$

The dielectric constant is that of the space charge layer and it is essentially equal to that observed for relative dielectric of grain boundary multiplied with the permittivity of vacuum, $\varepsilon \cong \varepsilon_{gb}\varepsilon_0$. The concentration c_y at infinity or in the grain interior is the concentration of yttrium in bulk. When we apply the unitless acceptor concentration we need to account for the molar distribution of oxygen by the oxygen density. The Debye length is then given by:

$$L_D = \left(\frac{RT\varepsilon_{gb}\varepsilon_0}{2F^2\rho_O\left[Y'_{Zr,eff}\right]}\right)^{\frac{1}{2}} \tag{2.237}$$

where both the permittivity of vacuum (ε_0) and the oxygen density (ρ_O) need to have the same unit of length.

2.3 Thermodynamics

Thermodynamics is the relation between the energy of a system subject to change from temperature change or work. An example is the hydration of yttrium doped barium zirconate. The total energy of the system is the Gibbs free energy, which is the contribution of enthalpy (energy) and entropy (microscopic coordinates). The entropy constitutes the dispersion of possible sites/orientations in a structure where the electronic energy landscape (enthalpy) is the same for each position. In other words, it represents the different microscopic systems that are possible. In general terms this relationship is expressed by:

$$\Delta G = \Delta H - T\Delta S \tag{2.300}$$

The hydration reaction expressed in (2.102), hydration is spontaneous at low temperatures, illustrated at T_1 in Figure 6. At higher temperature T_2 there is no free sites for the hydroxide ion left, and the entropic states are filled up. At this temperature hydration is no longer spontaneous. Further temperature increase may result in dehydration as the vibration entropy increases and deem sites unavailable for protons.

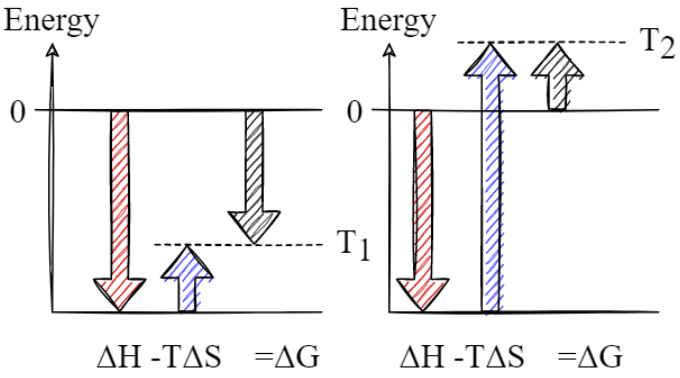

Figure 6: Gibbs free energy from spontaneous situation (hydration) to a forced situation (dehydration).

Entropy constitutes both the vibrational and configurational arrangements of microscopic states. The vibrational contribution will be the focus of this thesis as it determines the dependency on temperature and therefore the proton concentration. The configurational entropy can be disregarded when accounted for in the site fraction evaluation of oxygen, oxygen vacancies and hydroxides.

A short introduction and proof for why the configurational entropy can be disregarded. The configurational entropy is the distribution of vacancies among available sites.

$$S = k_B \ln(W) \tag{2.301}$$

$$W = \frac{(N + n_v)!}{N!\, n_v!} \tag{2.302}$$

By Stirling's approximation the expression in (2.301) becomes the site fraction, which in defect chemistry is an equivalent way of expressing activity or concentration in the equilibrium term. Effectively the configurational entropy does not contribute to the total entropy because we maintain the site ratio between oxygen, vacancies and protons when describing their concentration.

$$[O_O^x] = 3 - [v_O^{\cdot\cdot}] - [OH_O^{\cdot}] \tag{2.303}$$

2.3.1 Concentration of defects

The absorption of protons follows the reaction (2.102) and the equilibrium coefficient (2.105). Furthermore, the equilibrium coefficients are related to thermodynamics through van't Hoff's expression, which include the enthalpy and entropy of the reaction.

$$K_{hydr} = e^{\left(-\frac{\Delta G^{\circ}_{hydr}}{RT}\right)} = e^{\left(-\frac{\Delta H^{\circ}_{hydr}}{RT}\right)} e^{\left(\frac{\Delta S^{\circ}_{hydr}}{R}\right)} \tag{2.304}$$

Here with subscript *hydr* because the reaction is a hydration reaction. This can also be written in the linear form, which will be used for data to extract the slope and intercept.

$$\ln\left(K_{hydr}\right) = \frac{\Delta S^{\circ}_{hydr}}{R} - \frac{\Delta H^{\circ}_{hydr}}{RT} \tag{2.305}$$

For the hydration reaction there are two charge neutrality equations to consider. The amount of hydroxide ions, oxygen vacancies and oxygen atoms are related through the stoichiometry of the composition (2.303). Furthermore, the substitute of lower valence cation, yttrium, is related to the number of vacancies and thus the amount of hydroxide ions:

$$[Y_{Zr}'] = 2[v_O^{\cdot\cdot}] + [OH_O^{\cdot}] \tag{2.306}$$

Regarding synthesis and sintering, the yttrium content will deviate from that of the initial yttrium amount in the precursor mix. This may be due to a number of factors, some of them were proposed in the unwanted point defect chapter. Therefore the theory follows the simplified approach of Kreuer [19] where yttrium content is assumed to be proportional to the maximum proton concentration observed. It is proposed that yttrium may sit on the A-site, either substituting barium or replacing barium vacancies. Then the electroneutrality (2.306) can be written as:

$$[Y_B'] - [Y_A^{\cdot}] = 2[v_O^{\cdot\cdot}] + [OH_O^{\cdot}] \tag{2.307}$$

Yttrium may also reside elsewhere. The importance of the approach is to define the substitution degree of yttrium and include it in the derivations for modelling proton concentration and conductivity. We define the effective substitution concentration as:

$$[Y_{Zr,eff}'] = [Y_B'] - [Y_A^{\cdot}] = 2[v_O^{\cdot\cdot}] + [OH_O^{\cdot}] \tag{2.308}$$

where $[Y'_{Zr,eff}]$ is sometimes shortened to S, or S% if in percentage.

Applying these conditions on the equilibrium equation for hydration gives:

$$K_{hydr} = \frac{4[OH_O^{\cdot}]^2}{p_{H_2O}\left([Y'_{Zr,eff}] - [OH_O^{\cdot}]\right)\left(6 - [Y'_{Zr,eff}] - [OH_O^{\cdot}]\right)} \tag{2.309}$$

The following equation can be solved to express the proton concentration by the equilibrium constant (thermodynamics), the effective acceptor concentration (S) and partial pressure of water:

$$[OH_O^{\cdot}] = \frac{3Kp_{H_2O} + \sqrt{Kp_{H_2O}\left(9Kp_{H_2O} - 6Kp_{H_2O}S + Kp_{H_2O}S^2 + 24S - 4S^2\right)}}{Kp_{H_2O} - 4} \tag{2.310}$$

See 9.2 for derivation in Appendix A.

From the electroneutrality condition (2.308) the correlation between hydroxide ion concentration and oxygen vacancies are given in relation to the assumed effective acceptor dopant. Which can be rearranged to express vacancy concentration:

$$[v_O^{\cdot\cdot}] = \frac{[Y'_{Zr,eff}] - [OH_O^{\cdot}]}{2} \tag{2.311}$$

Expression (2.310) and (2.311) are correlated, knowing one concentration will give the other.

2.3.2 Concentration of minority charge carriers

The concentration of holes can be expressed as in (2.111), where the oxygen vacancy and oxygen concentration are given by (2.311) and (2.303), respectively:

$$[h^{\cdot}] = K'_{ox}\left(\frac{[Y'_{Zr,eff}] - [OH_O^{\cdot}]}{2}\right)^{\frac{1}{2}}(3 - [v_O^{\cdot\cdot}] - [OH_O^{\cdot}])^{-\frac{1}{2}}\, p_{O_2}^{\frac{1}{4}} \tag{2.312}$$

Since oxygen concentration is $2.9 \leq [O_O^x] \leq 3$ when doping with 20mol% yttrium the expression can be simplified with $[O_O^x] = 3$:

$$[h^{\cdot}] = K'_{ox}\left(\frac{[Y'_{Zr,eff}] - [OH_O^{\cdot}]}{2}\right)^{\frac{1}{2}}(3)^{-\frac{1}{2}}\, p_{O_2}^{\frac{1}{4}} \tag{2.313}$$

The enthalpy and entropy of formation determining K'_{ox} for holes is difficult to extract as mass change is minimal and not distinguishable from other possible defect reactions, such as hydration/dehydration. Thus, the entropy and enthalpy of formation and mobility can't be separated. Oxygen partial pressure dependencies are instrumental to examine the theoretical ¼ dependency as presented in section 2.1.2 and to determine the overall activation barrier. The conductivity expression for holes is then given by (2.201) with the concentration expression tangled with the mobility:

$$\sigma_p = \sigma_p^0 \left(\frac{\left[Y'_{Zr,eff}\right] - \left[OH_O^{\cdot}\right]}{2}\right)^{\frac{1}{2}} (3)^{-\frac{1}{2}} p_{O_2}^{\frac{1}{4}} \exp\left(-\frac{\Delta H_a}{RT}\right) F \rho_O \qquad (2.314)$$

where the pre-exponential consists of the entropy of formation and mobility, $\sigma_p^0 = \exp\left(\frac{\Delta S_f}{R}\right) \times u_p^0$). The activation enthalpy consists of the enthalpy of formation and mobility, $\Delta H_a = \Delta H_f + \Delta H_m$.

2.4 Impedance Spectroscopy

Impedance spectroscopy uses an alternating voltage to investigate the electrochemical properties of a system or sample. The alternating current (AC) response from the system is used to describe both resistive and dielectric properties when the frequency of the sinusoidal wave is changed. As faradic elements charge and discharge with a characteristic time constant the shift in frequency determines the degree of phase change between the AV and AC. In an ionic conductor there are different intrinsic capacitors which are listed with typical capacitances in Table 3.

Table 3: Mechanisms in ionic solids and their approximate capacitance.

Mechanism	**Capacitance [F cm^{-1}]**
Bulk	$\sim 10^{-12}$
Grain boundary	$\sim 10^{-11} - 10^{-8}$
Trippel phase boundary / interface	$\sim 10^{-8} - 10^{-6}$

Charge transfer	$\sim 10^{-6} - 10^{-3}$
Mass transfer	$\sim 10^{-3} - 1$

A capacitance is either given as the amount of charge (Q) per potential (U), or by its dielectric constant (ε_r) relative to the permittivity of vacuum (ε_0) according to its surface area (A) and thickness (d):

$$C = \frac{Q}{U} = \varepsilon_0 \epsilon_r \frac{A}{d} \tag{2.400}$$

A resistor acts according to Ohms' law and is the internal electrostatic friction felt by the charge carrier in a potential field. In an alternating situation the potential and the current can be described by sinusoidal function of the angular frequency ω and the time t, together they constitute what is called the phase angel. The angular frequency is related to the frequency by $\omega = 2\pi f$.

$$R = \frac{U}{I} = \frac{U_0 \sin(\omega t)}{I_0 \sin(\omega t + \theta)} \tag{2.401}$$

The phase angle describes the relation of the two sinusoidal waves. The response from the current will differ from the alternating applied voltage when a capacitor is charged/discharged, which is the phase offset θ. A perfect capacitor portrays a phase angel shift from 0 to -90° and has an infinite resistance as charge can't transpose over the element. From EIS measurements impedance is extracted, which is the complex set of expression (2.401) when separating in phase and out of phase response:

$$Z^* = Z_{re} + iZ_{im} = R + iX \tag{2.402}$$

Here Z_{re} is the real part, which is the resistance in phase, while the Z_{im} is the imaginary part which is the resistance out of phase, or better called reactance. Impedance (Z^*) is thus the composite of the real resistance and imaginary reactance. The impedance can also be given as:

$$Z^* = \frac{1}{i\omega C_0 \varepsilon^*} = \frac{1}{i\omega C} \tag{2.403}$$

where the complex permittivity is ε^*, C_0 is the geometrical capacitance of the cell.

The inverse of impedance gives the conductance and the imaginary part called susceptance.

$$Y^* = \frac{1}{Z^*} = G + iB \tag{2.403}$$

The resistance and conductance of a material is inversely related to its resistivity and conductivity specific to the conductor area and length. R is resistance, ρ is resistivity, G is conductance and σ is conductivity.

$$R = \rho \frac{l}{A} \tag{2.404}$$

$$G = \sigma \frac{A}{l} \tag{2.405}$$

$$\sigma = \frac{1}{\rho} \tag{2.406}$$

2.4.1 Nyquist Plot

A Nyquist plot consist of the data points from an impedance sweep over a set frequency range. The X axis is the real part, and the Y axis is the imaginary part. High frequency will be associated with a small capacitance, while low frequency is associated with a larger capacitance, i.e., from high to low frequency we will typically expect bulk, grain boundary and electrode related capacitors as seen in Figure 7.

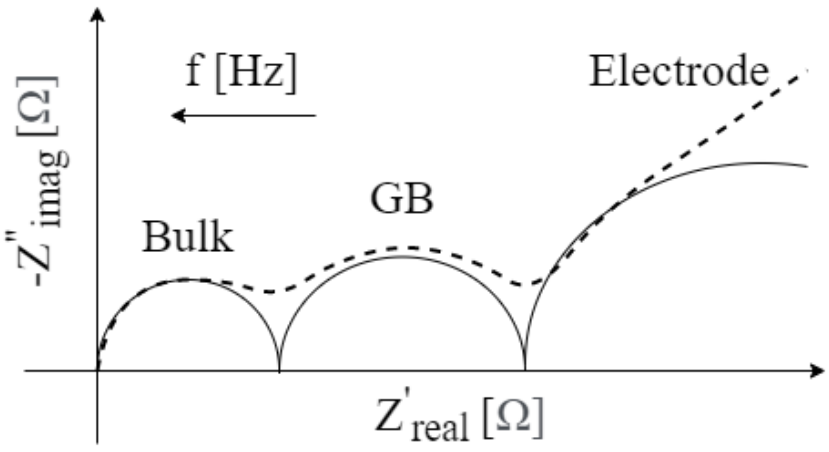

Figure 7: Typical Nyquist plot of polycrystalline ionic conductor.

2.4.2 Equivalent Circuits

The Nyquist plots must be deconvoluted to specific property parameters such as resistance and capacitance to give more precise information about the electrochemical properties of the sample. This process involves the construction of electrical circuits that behave or have the same characteristics as the sample in question, i.e., equivalent circuits. Furthermore, these circuits are fitted, simulated, and manipulated to resemble the real measurements as accurate as possible. The program Zview® from Scribner is used for this procedure in this work.

The equivalent circuit used for a polycrystalline ionic conductor usually consists of a resistor and capacitor connected in parallel for each semicircle illustrated in Figure 8. Here constant phase elements (CPE) are used to describe non ideal response from a capacitor, usually seen in a Nyquist plot as a supressed semicircle. Its relation to capacitance is given by:

$$C = \frac{R^{(1-P_{CPE})}}{P_{CPE}} T_{CPE}^{\left(\frac{1}{P_{CPE}}\right)} \tag{2.407}$$

Where P_{CPE} is a number between zero and one describing the deviation from an ideal capacitor, and T_{CPE} is the apparent ideal capacitance. R is the resistance of the RCPE circuit.

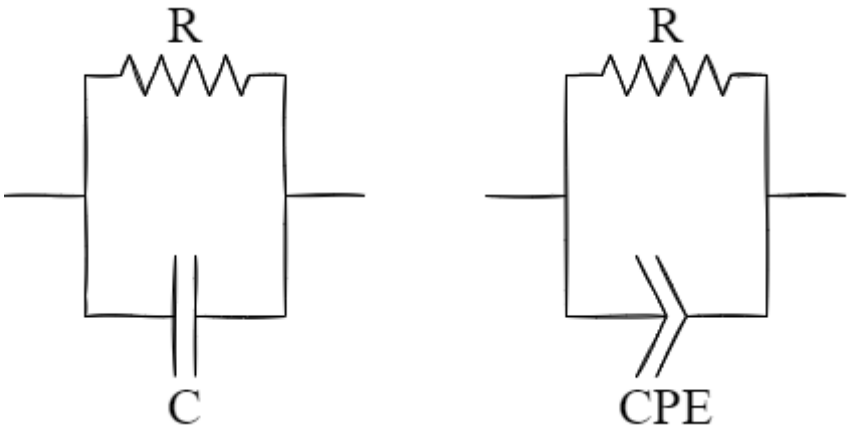

Figure 8: Parallel circuits usually associated with bulk and grain boundary semicircles.

2.5 Trapping of protons

Proton migration is considered to happen by the free migration mechanism which is the Grotthuss mechanism. Protons associate with oxygen ions in the lattice and form hydroxide ions where the proton is free to reorient itself and jump to neighbouring oxygen atoms.

Trapping happens as positively charged protons or hydroxide ions are in the vicinity of a negatively charged yttrium ion, which effectively increases the binding energy of the local proton. This results in an increased activation barrier for proton migration which will affect the overall diffusion, mobility, and conductivity of protons. The defect pair that is formed in such a case can be described by the reaction:

$$OH_{O,f}^{\cdot} + Y_{Zr,f}' = (OH_O^{\cdot} Y_{Zr}') \tag{3.400}$$

Where *f* denotes that the proton and yttrium ion is free and then becomes associated as a defect pair, effectively immobilising the proton. If the trap acts as a permanent dipole the trapping mechanism could be formulated through a dielectric relaxation process. Figure 9 illustrates the possible reorientation of a trapped dipole within an alternating electric field.

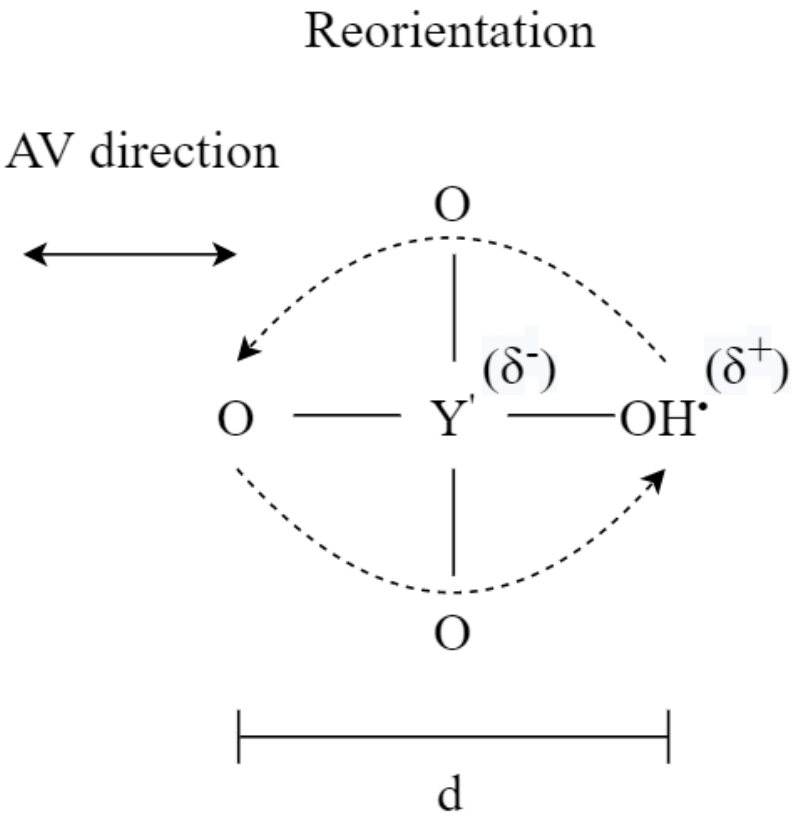

Figure 9: Dipole reorientation of a trapped hydroxide ion associated with a negatively charged yttrium cation (or yttrium octahedra).

At low temperatures in humid conditions the proton conductor is expected to be fully hydrated, thus the mobility[3] of protons is governing the temperature dependency ($E_{appernt}$ =

[3] Mobility is the total transport of the charge carrier, while migration is the transport due to the applied field (long range hopping, for example by Grotthuss mechanism).

$E_{H^+,mobility}$). When incorporating the possibility of trapped and free protons the apparent activation barrier consists of:

$$E_{a,apperant} = E_{a,trap\ free} - E_{a,trap} \tag{3.401}$$

Here the trapping energy is a negative value because the bond between the proton and the trapping centre, yttrium, is formed by columbic interactions that are attractive. The expression can be reiterated for the mobility of protons, the migration energy of protons and the association[4] energy of the trap.

$$E_{a,mobility} = E_{a,migration} - E_{a,association} \tag{3.402}$$

In other words, the observed mobility of protons comprises the protons that move and are trapped, the protons that are trapped need to overcome an extra energy barrier to contribute to long range transport.

2.5.1 Dielectric relaxation

Dielectric relaxation is related to the resonance of a permanent dipole in an alternating electric field, where the resonance is the peak reorientation frequency at a particular AV.

The capacitance related to the relaxation of a molecular dipole can be estimated if we assume that the dipole is reorientating within the constraints of the alternating field direction. Now we can define a vector less dipole at a point of reference in the middle of the reorientation distance (d) with the assumption that the dipole consists of two opposite charges ($\pm e$), this gives the dipole as:

$$\mu_{dip} = e\ d \tag{2.403}$$

The oxygen density (ρ_O) of the composition multiplied with Avogadro's number can be reiterated as the unspecific dipole density, which can be multiplied with mole fractions (or relative concentrations) to obtain specific dipole densities. For hydroxide ions and oxygen vacancies this is the same as the fraction of yttrium or effective acceptor concentration:

$$N_{dip} = X_{Y'} N_a \rho_O \tag{2.404}$$

[4] Association (trap) energy can also be regarded as dissociation (overcoming the trap) energy, for a diatomic columbic interaction the dissociation has equal but positive value.

The relaxation strength commonly extracted through complex permittivity and fittings with relaxation models can be estimated by considering the dipole and concentration of a particular species:

$$\Delta\varepsilon \approx \frac{1}{\varepsilon_0}\frac{\mu_{dip}^2}{k_B T}N_{dip} \tag{2.405}$$

The relaxation strength is the dielectric constant of the dipole, which then gives the approximate capacitance corresponding to the relaxation process:

$$C_{dip} = \varepsilon_0 \Delta\varepsilon \frac{A}{l} \tag{2.406}$$

where A and l are area and length, respectively, specific to the conductor.

The resonating polarisation related to the relaxation mechanism results in energy lost to the system as heat. General polarisation mechanism and associated resonance frequencies are presented in Table 4. Both space charge and permanent dipole polarisations are of interest. Permanent dipole reorientation could be associated with trapped ionic charge carriers, while space charge polarisations could be associated with the dielectric of the grain boundary or the electrode – electrolyte interface. Space charge polarisations consist of both polarisation of free charged and permanent dipoles.

Table 4: Polarisations and associated resonance frequencies.

Polarisation	**Frequency** $[\boldsymbol{Hz}]$
Electrons	$\sim 10^{15}$
Atoms	$\sim 10^{12}$
Permanent Dipoles	$\sim 10^{6} - 1$
Space charge polarisations	$\sim 10^{4} - 0.01$

3 Literature

3.1 Background

The perovskite structure shows a diverse set of properties useful in a range of application, such as electrolytes, electrodes, piezoelectric, optics, lasers, catalytic, etc. First discovered by Gustav Rose in the Ural Mountains in 1939 as the naturally occurring calcium titanate and named after the Russian mineralogist Lev Aleksevich von Perovski [20].

3.1.1 Perovskite

The perovskite structure is an oxide of the general composition ABO_3, where A and B are typically a di- and tetravalent element, respectively. There can be a distribution of other valences across the sites if the structure is neutral and intact. Some examples are A=Ba, Sr, Ca, and B=Ti, Zr, and Ce. The A site cation is coordinated in a dodecahedron (CN=12) and the B site cation in an octahedron (CN=6) with respect to oxygen. This constitutes a primitive cubic unit cell with space group Pm-3m. For the functional material some B-site cations are doped with lower valent elements such as Y, Yb, Gd, Nd or Sm. The nonstoichiometric material is compensated by defects that ensures charge neutrality in bulk.

Depending on the ions that constitute the perovskite it can exhibit a lowered symmetry until a point where the phase is no longer stable. The symmetry of the structure is expressed by the Goldschmidt tolerance factor (t) [21]:

$$t = \frac{r_A + r_O}{\sqrt{2}(r_B + r_O)} \tag{3.100}$$

Which for $BaZrO_3$, $SrZrO_3$ is approx. 1 and 0.95 [22], while the yttrium doped variants show a decreased tolerance factor with increasing yttrium content [23]. Inversely proportional to an increased lattice parameter as yttrium is a larger cation.

3.1.2 Functional perovskites

From an electronegativity point of view there are correlations between the hydration enthalpy and entropy, and chemical stability versus the type of B-site cation in relation to Ba and Sr on A-site. With increasing electronegativity, the hydration coefficient decreases in the order; Ce, Zr, Sn, Nb, Ti, vis versa the chemical stability increases. Chemical stability in this case refers to stability under CO_2 and H_2/H_2O atmospheres, thus the evolution of carbonates and hydroxides, which happens in relation to the A-site cation. To elaborate further, the enthalpy of hydration for $BaCeO_3$ is more exothermic (more negative) than for $BaZrO_3$, the same applies

for $SrCeO_3$ and $SrZrO_3$. The trend is explained to be a result of the slight shift in basicity of the oxide [19].

The poor chemical stability of $BaCeO_3$ results in degrading proton conducting abilities over time, which is fixed by partial or full substitution of zirconium, typically 40mol% is enough to increase the chemical stability significantly. But it's also enough to decrease the degree of hydration significantly [24].

3.1.3 BSZCY

The BSZCY perovskite variant that will be investigated in this work was first presented by Dayaghi et al. [4] with the aim to increase thermal expansion coefficient for the highly proton conducting BZY. A high TEC means higher volume change as a function of temperature, which means less strain on the structure and contact areas with electrodes with similar TEC. Since the TEC increases, $BaZrO_3 < SrZrO_3 < SrCeO_3 < BaCeO_3$ [25, 26], strontium and cerium substitution on A- and B-site were performed, respectively. This resulted in an increased TEC as proposed. The results are presented in Table 5 with comparisons to BZY10 and BZY15.

Table 5: TEC comparison for BZY variants.

Material	$\boldsymbol{TEC}$: $\boldsymbol{30-450°C}$ $[\boldsymbol{10^{-6}K^{-1}}]$	$\boldsymbol{TEC}$: $\boldsymbol{600-1150°C}$ $[\boldsymbol{10^{-6}K^{-1}}]$	**Remark / reference**
BSZCY151020	10.07	10.11	Synthetic Air / [4]
BSZCY151020 + 1 wt.% NiO	9.71	9.73	
BZY10	7.27	8.45	Dry air / [27]
BZY10	7.29	7.13	Air + 3% H_2O / [27]
BZY15	8.0	8.0	Dry / [19]

3.2 SSRS

Solid state reactive sintering is a straightforward synthesis method commonly employed in the manufacturing of metal alloys. The one step temperature treatment has seen increased popularity over the last two decades also for synthesis of functional ceramics. It has proven a cost effective and reliable method to produce dense solid electrolytes. Especially when employing sintering additives which increases densification at lowered temperatures and for shorter sintering times.

3.2.1 Barium Evaporation

It is shown by Yamazaki et al. [28] that undoped barium zirconate and barium cerate do not exhibit barium loss to a degree that is comparable with the yttrium doped variants. Which indicates that the problem is inherent to the yttrium substitution on B-site. The underlying reason is expected to be the difference in ionic radius between Zr and Ce, and Y. Respectively the ionic radius is 0.84Å, 0.97Å and 1.019Å (Imperial College London Atomistic Simulation Group & [11]). This is also expected to be partly the reason for increased hydration and mobility of protons in the cerate compounds as the ionic radius is more comparable between the host and dopant.

Yttrium is occupying A-site in addition to B-site. This nudges barium to segregate or evaporate. The initial incorporation reaction of yttrium presented in the defect theory chapter might therefore have a different characteristic, as proposed by Yamazaki:

$$2Ba_{Ba}^{x} + v_{O}^{\cdot\cdot} + Y_2O_3 = 2Y_{Ba}^{\cdot} + O_{O}^{x} + 2BaO \qquad (3.200)$$

This is also, why Kreuer et al. [19] proposes effective acceptor dopant as a function of yttrium content on the A-site. To combat this issue the powders are sintered in sacrificial powder, which is calcined powders with the same composition as the sample and with a surplus of barium carbonate, typically 10wt.% [29].

At high temperatures barium may react with alumina in the crucible, this is seen for BZY20 samples with NiO as sintering aid. [30], forming both $BaAl_2O_4$ and $Ba_3Y_2AlO_{7.5}$. From the studies of Burtsev et al. [31] barium has seemingly higher diffusivity in alumina than magnesia. These studies are done with plasma-melted barium slags, but it may suggest that magnesia is better than alumina as crucible material also for SSRS. An in-house study by Dayaghi has shown that BZYb samples sintered in magnesia crucible show higher hydration than those sintered in alumina crucibles. This is probably related to the volatility of barium [30].

3.2.2 Sintering additives

Sintering additives have been introduced as a means to increase densification and allow sintering at lower temperatures for shorter times. Nikodemski et al. [32] did an extensive study on transition metal oxides from period 5 and 4, and their effects on densification of a BCZY63 ($BaCe_{0.6}Zr_{0.3}Y_{0.1}O_{3-\delta}$). They found that the divalent cation from period 4 showed the best densification. Of these CuO, CoO, ZnO and NiO showed promise. Ni has also been extensively used as anode material in a complete fuel cell and has shown an improved effect on densification when co-sintering is applied. The additives behave as diffusion inducing bridges or as complexes, either as solids or liquids. This decreases the dihedral angle between grains which speeds up diffusion and thus sintering.

On the addition of sintering additives, there is some proposed defect mechanisms and relations to barium deficiency, decrease of hydration and possibly the introduction of electrical conductivity. Polfus et al. [33] carried out a mixed computational-experimental approach to study the solubility of transition metal as interstitials in BZY. Among the cations of interest were Ni and Cu. The nickel interstitials were in fact associated with barium vacancies. This defect pair is formed by introduction of nickel oxide to an A-site vacancy:

$$NiO + v''_{Ba} + v^{\cdot\cdot}_{O} = (Ni_i v_{Ba})^{x} + O^{x}_{O} \tag{3.201}$$

Both (3.200) and (3.201) include the annihilation of oxygen vacancies, which effectively lowers the nominal hydration levels. An alternative to the incorporation of nickel into the structure is the formation of a barium and yttrium rich secondary phase:

$$NiO + Ba^{x}_{Ba} + v''_{Ba} + 2Y'_{Zr} + 4O^{x}_{O} + 2v^{\cdot\cdot}_{O} \xrightarrow{-2BaZrO_3} BaY_2NiO_5 \tag{3.302}$$

It was also shown that the copper cation probably could act in the same manner as nickel, but with the discrepancy of having an isolated state within the band gap with approximate band energy of 1.3eV. This may indicate a state unrelated to that of host cations and oxygen.

The parasitic contributions from the sintering aids have been investigated and observed for both hydration and conductivity of sintered samples. Han et al. [6] found that hydration decreased by the addition of ZnO, CuO and NiO investigating hydration by Karl-Fischer titration. They also deduced the average distribution of the sintering aid. cations overall, between the grain interior and the grain boundary by means of ICP-AES measurements and STEM-EDS analysis. It was observed that nickel was incorporated into the sample to a higher degree than CuO and

ZnO, also that the post annealing to reduce the binary oxides to metal had little effect on Ni situated in the grain interior and grain boundary. Furthermore, an abrupt decrease in ionic transport number was observed when the amount of sintering aid was around 2wt.%, indicating that the divalent cations may increase electronic defects. Figure 10 show hydration results with respect to sintering aid. content in at.%, where 1wt.% CuO and NiO correspond to approximately 0.5at.% and 1.25at.%, respectively [6]. They show that nickel decreases the proton concentration more than copper, which is due to the difference in atomic concentration of cations dissolved in the BZY lattice.

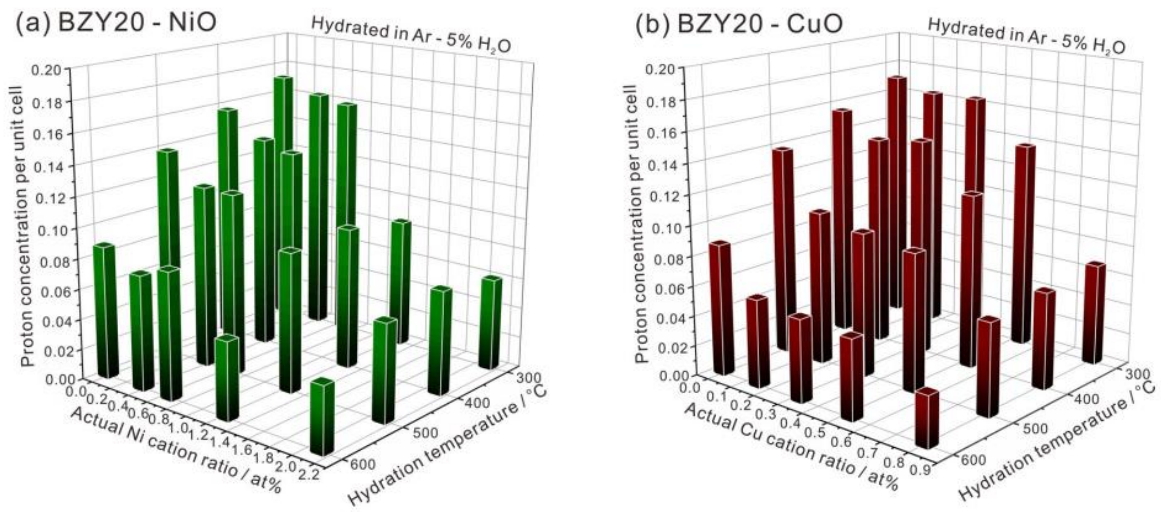

Figure 10: Proton concentrations as a function of sintering additive content versus temperature in 5% H_2O – Argon mix from Han et al. [6].

Nickel oxide is the most investigated sintering aid, probably because of its application as support in composite BZY-NiO anode materials. From XRD studies by J. Tong et al. [34] at set of BZY20 samples with 2wt.% NiO were sintered between 800°C and 1500°C for 10 hours. The initial phases of NiO and $BaNiO_x$ were documented until 850°C, and at 900°C the BaY_2NiO_5 phase was identified, and disappeared at 1500°C. It was also shown that the latter phase melted at around 1450°C. As a result of the $BaNiO_x$ phase, the perovskite formation temperature was 100°C lower than that of the control sample.

3.3 Hydration

Hydration thermodynamics for different proton conductors extracted by TG measurements in either isobaric or isothermal conditions are presented in Table 6. Here some of the electronegativity trends are visible, BCY exhibit more negative hydration enthalpy than BZY.

When increasing the Zr content in a BZCY sample we expect a decrease in negativity for the hydration enthalpy.

Table 6: Hydration thermodynamics for selected yttrium doped perovskites obtained from isobaric and isothermal thermogravimetric measurements.

Composition	p_{H_2O} atm	ΔH_{hydr}° $[kJ\ mol^{-1}]$	ΔS_{hydr}° $[J\ K^{-1} mol^{-1}]$	S%	**Remark / reference**
BZY20	0.023	-93.3	-103.2	18	Isobar, [35]
BZY10	0.023	-79.4	-88.8	10	Isobar, [35]
BCY20	0.035	-172	-158	16	Isobar, [36]
BCY10	0.023	-162.2	-166.7	10	Isobar, [37]
$BaCe_{0.2}Zr_{0.7}Y_{0.1}O_3$ + 1mol% NiO	0 – 1 (600°C)	-127 ± 2	--	--	Isothermal, [38]
$BaCe_{0.2}Zr_{0.7}Y_{0.1}O_3$ + 2mol% NiO	0 – 1 (600°C)	-125 ± 2	--	--	Isothermal, [38]

3.4 Proton conductivity in oxides

Norby and Larring [39] compared the proton conductivity in different oxides by gathering data for proton mobility and hydration thermodynamics. Figure 11 shows conductivities for 10mol% acceptor doped perovskites versus temperature. Acceptor doped $BaZrO_3$ stands out because of its high conductivity, surpassing $10^{-2}\ S\ cm^{-1}$ above 400°C. Even higher conductivity was seen in Y-doped $BaCeO_3$, but as mentioned the oxide suffers from poor chemical stability, which has led to a significant number of studies on the mixed cerate – zirconate structure to optimize properties.

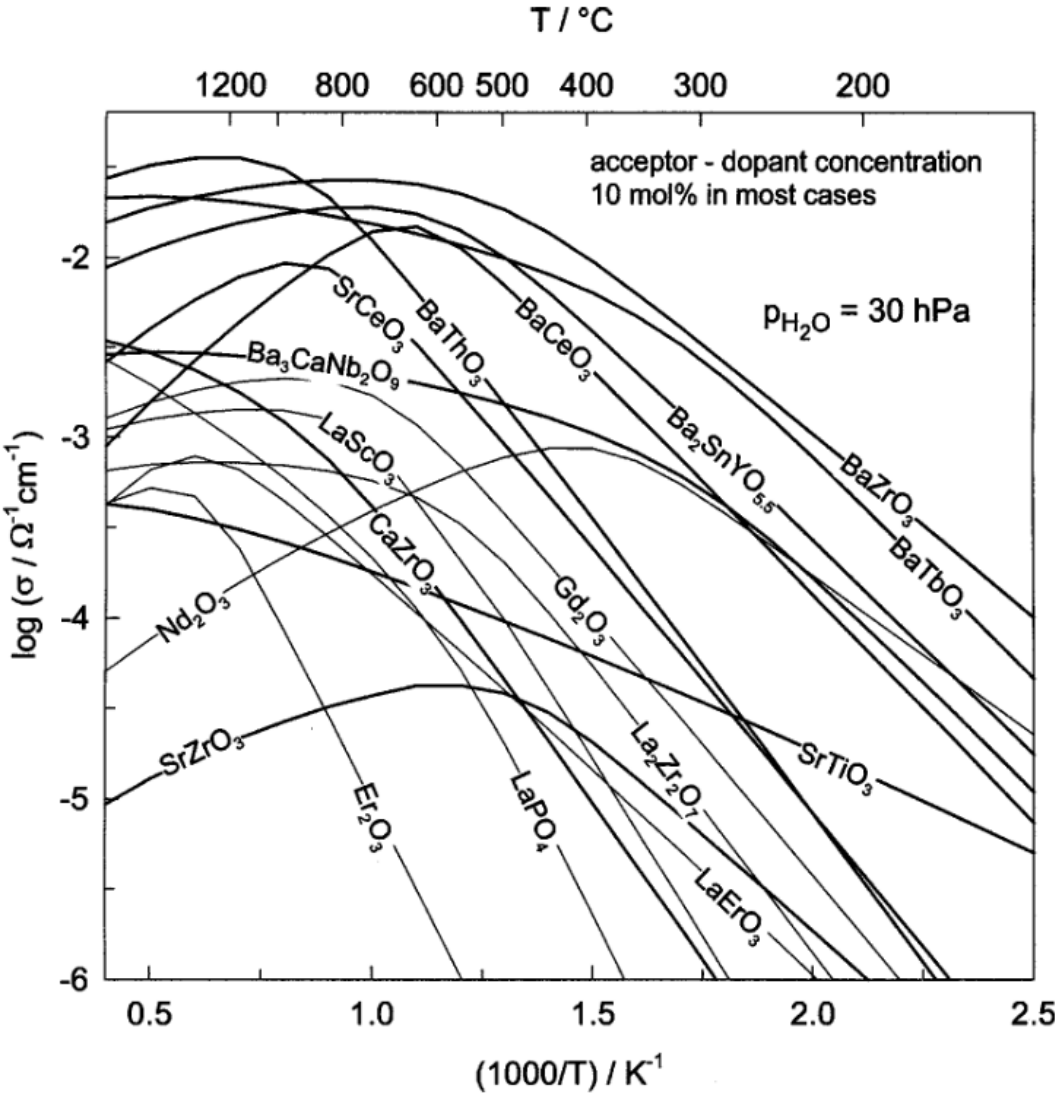

Figure 11: Proton conductivities for a selection of 10mol% acceptor doped perovskite variants as a function of temperature from [19]. The conductivities are calculated from parameters for mobility and thermodynamics, and the proton concentrations, according to Norby and Larring [39].

3.5 Charge carrier transport parameters

The activation energies in different temperatures range are often presented in combination with conductivity data for different perovskite variants. However, these activation energies are less commonly extracted, defined, and presented as isolated charge carrier parameters such as pre-exponential and enthalpy of mobility of protons, oxygen, or holes. And when presented, there is no consensus as to which unit the pre-exponential is best presented.

Tsvetkov et al. [40] presents charge carrier parameters for protons, oxygen vacancies and holes according to Arrhenius linearisation of conductivity data for BZY10. They also present the resulting model as a function of pO_2 and pH_2O for both conductivity and transport numbers at

constant temperatures. The result for transference number at 1038°C can be seen in Figure 12, where holes are shown to dominate even in inert atmospheres, around $pO_2 \sim 10^{-6}$atm, when temperature is high enough. Similar transport numbers have also been presented for $BaCe_{0.2}Zr_{0.7}Y_{0.1}O_3$ by Ricote et al. [38] in oxidising and reducing atmospheres by electromotive force (EMF) measurements.

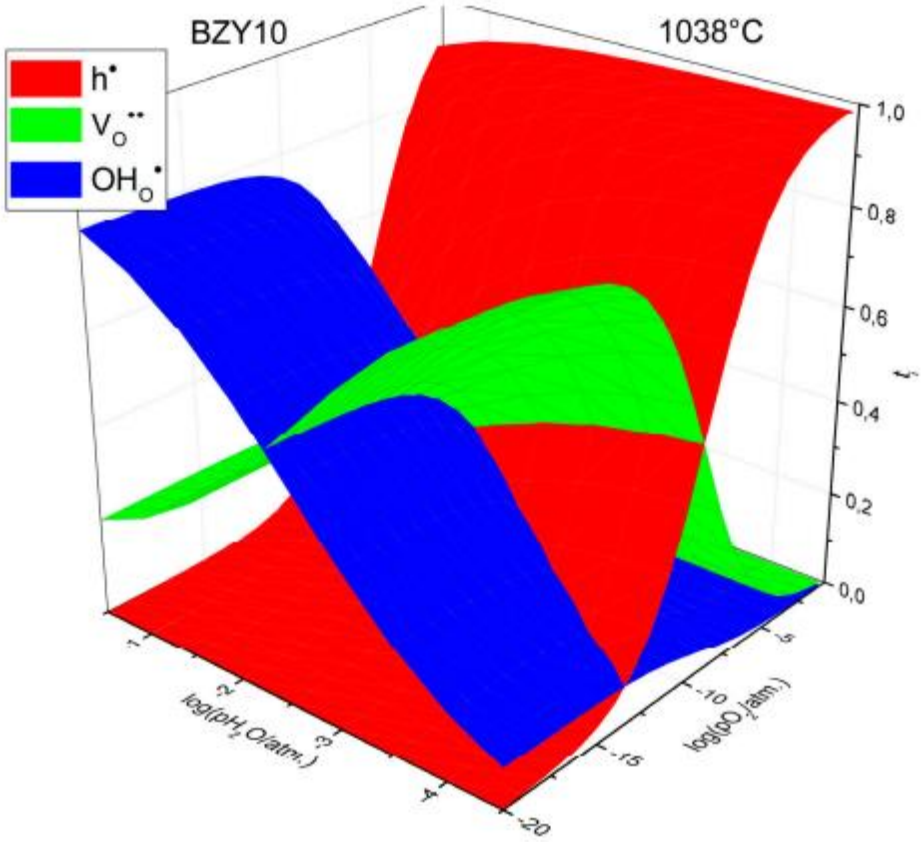

Figure 12: Transference numbers for different charge carriers at 1038°C as a function of pO_2 and pH_2O [40].

The same parameters have also been reported for the 20mol% yttrium doped variant. Zhu et al. [41] investigated the effects of polaron trapping, which is the mechanism where ionised oxygen (oxygen with hole) associates with a yttrium cation and form a defect couple. It was shown that neither proton nor oxygen mobilities were not affected by the inclusion of polaron trapping in the modelling.

Selected parameters for the three charge carriers are presented in Table 7 from studies on comparable compositions of the yttrium doped perovskite.

Table 7: Apparent mobility enthalpies for protons, oxide ions and holes for some BZY compositions.

Charge Carrier	**Enthalpy of activation energy**	**Zhu et al. [41] BZY20**	**Tsvetkov et al. [40] BZY10**	**Coors et al. [42] NiBCZY27**	**Wang et al. [43] BZY07**	**Bohn and Schober [44] BZY10**
$OH_O^{\cdot}$	E_{mob} $[kJ\ mol^{-1}]$	61	--	43	--	42
$v_O^{\cdot\cdot}$	E_{mob} $[kJ\ mol^{-1}]$	85	137	90	55	106
$O_O^{\cdot}\ (h^{\cdot})$	E_a $[kJ\ mol^{-1}]$	79	70	--	97	87

In the studies by Kim et al. [45], a set of mobility values for temperatures 750, 700, 650, and 600°C for each charge carrier were found by a modelled fitting of conductivity vs pO_2 and pH_2O for BZCYYb1711. Using Arrhenius expression for mobility, comparative values were extracted in the temperature range (750-600°C) and are presented in Table 8.

Table 8: Calculated pre-exponential and enthalpy of mobility from mobility values for each charge carrier from [45]. *Hole parameters are also comprised of the formation parameters for the oxidation reaction.

Charge Carrier	**Pre-exponential** $u_i^0\ [cm^2\ K\ V^{-1}\ s^{-1}]$	**Enthalpy of mobility / activation** $\Delta H_{i,mob}\ [kJ\ mol^{-1}]$	**R^2**
$OH_O^{\cdot}$	33.42	48.49	0.9906
$v_O^{\cdot\cdot}$	263.04	76.34	0.9738
$h^{\cdot}\ /\ (O_O^{\cdot})$*	1666.27	76.40	0.8573

3.6 Trapping

The mechanism of trapping has been described in several papers, often from a theoretical perspective. Yamazaki et al. [9] approached the problem of proton trapping by comparing low and high temperature diffusivity of protons, the latter was approximated by means of exchange measurements to find the ambipolar diffusivity between protons and deuterium. The difference between the Arrhenius slopes were attributed the association energy of the trap. The following hopping sequence of a trapped and free proton is depicted in the illustration from Yamazaki in Figure 13. The association energy was found to be -29 kJ mol^{-1}.

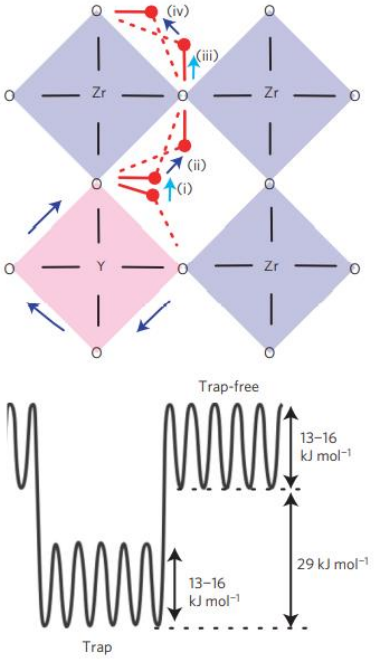

Figure 13: Schematic of proton migration of a trapped and free proton from Yamazaki et al. [9].

To expand upon the relationship between relaxation of a permanent dipole and trapping some shortcuts in theory has been taken. Mainly because the intermediate steps are complex and not explained in detail in literature. The foundation is therefore explained in short in this section to emphasise that the theory is on the periphery of the authors understanding and that literature is relayed upon.

From electrochemical impedance spectroscopy a set of frequency dependent complex properties are obtainable. These are impedance (Z*), admittance (Y*), electric modulus (M*), permittivity (ε*) and dielectric loss tangent (tan (δ)), which are all related through a set of expressions for permittivity [46] and can be generalised through:

$$\tan(\delta) = \frac{\varepsilon''}{\varepsilon'} = \frac{Z'}{Z''} = \frac{M''}{M'} = \frac{Y'}{Y''} \tag{3.600}$$

The dielectric loss tangent or dissipation factor (tan (δ)) is best presented in an argand diagram as in Figure 14, where δ is the phase angle shift from an ideal capacitor (-90° + δ) and the relation to permittivity is solved by trigonometry:

$$\frac{\varepsilon''}{\varepsilon'} = \frac{\varepsilon^* \sin(\delta)}{\varepsilon^* \cos(\delta)} = \tan(\delta) \tag{3.601}$$

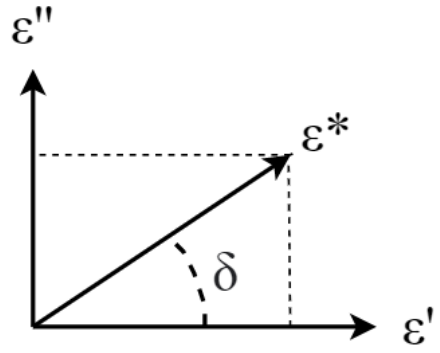

Figure 14: a) Argand diagram for complex.

The real part of permittivity measures the polarisation of the material, while the imaginary part measures the dielectric loss. To be more precise, the real part constitutes the absorbed energy in the system, while the imaginary part constitutes the energy lost to the system, both to polarisations. In mixed ion-proton conductors' polarisation and dielectric loss due to ionic charge carrier transport (hopping) is dominating [47, 48][5], consequently dielectric loss (ε'') characteristics for relaxation mechanisms are concealed. Where (ε'') for relaxation takes the form of a peak at the frequency of resonance is concealed by a nearly constant increase in dielectric loss due to conduction. In literature, this is circumvented by estimating that $\tan(\delta) \propto \varepsilon''$ [46, 49-51], where the dielectric loss tangent gives the ratio of dielectric loss to polarisation. In other words, $tan(\delta)_{max} \propto \varepsilon''_{max}$, which in turn by Arrhenius expression gives the activation energy of the relaxation process:

$$\tan(\delta)_{max} = \tan(\delta)^0_{max} \frac{1}{T} \exp\left(-\frac{E_{as}}{k_B T}\right) \tag{3.602}$$

[5] The reasons for the so called nearly constant (dielectric) loss for ionic conductors is still under discussion.

Typically called association energy (E_{as}) to convey that it's the permanent dipole that is of interest, thus trapping mechanisms. The correlating resonance frequency of $\tan(\delta)_{max}$ is related to the speed of which reorientation happens, which would equal the energy barrier of migration:

$$f_{max}(\tan(\delta)_{max}) = f_{max}^{0}\frac{1}{T}\exp\left(-\frac{E_{mig}}{k_B T}\right) \qquad (3.603)^{6}$$

A permanent dipole will exhibit increased resonance frequency with increase in temperature and thermal motion, and at sufficiently high temperature thermal motion might disrupt the dipole reorientation. In other words, reorientation is faster as thermal motion increases, until a point where thermal motion dominates, and the free charge of the dipole contributes to transport. In the case of protons, they are freed from the yttrium trap. Pending on the type of dipole the frequency range will vary and will have a characteristic temperature range, in which change in dielectric loss can be distinguished.

The dielectric loss tangent has mainly been used to extract association energies for oxide ion conductors [50, 51]. For proton conductors, there are few papers on extraction of association energies by using (3.602). Singh et al. [52] used dielectric loss tangent for BSCZGY and found two relaxation peaks in the $\tan(\delta)$ – frequency plot, which were attributed the relaxation of protons in isolated and clusters of YO_6 octahedra. The association energies for the two relaxation mechanisms are presented in Table 9 with values from computational studies.

Table 9: Association energies from calculations and tan(δ) extraction associated with isolated and clusters of YO_6 octahedra.

Composition	**E_{ass} [kJ mol^{-1}] (Y-OH)**	**Reference / method**
BZY20	29	[9] / Diffusivity calculations
BZY	25	[53] / calculations
BZY3.7	15	[54] / calculations
BSCZGY	14 (isolated YO_6) 20 (clusters)	[52] / tan(δ)

[6] In literature the expression is used with and without the temperature variable outside the exponent (inconsistent).

4 Experimental

4.1 Sample preparation

The solid-state-reactive-sintering method is used to fabricate all samples in this thesis. However due to increased experience and discussions with co-workers the method was altered through the 2-year period aiming to increase the low proton concentration that were seen from the previous attempts. To keep some comparability between the samples of different batches only the sintering parameters were altered.

4.1.1 General approach

The precursors $BaCO_3$, $SrCO_3$, ZrO_2, CeO_2 and Y_2O_3 were weighed out with a precession weight according to the stoichiometric ratios of the composition. Usually 20-25grams of powder were made for each batch. Next, the powders were mixed in a 250cm^2 plastic container using 140 grams of 10mm and 5mm diameter zirconia balls in isopropanol in a roll mill for 72hours. The isopropanol was evaporated on a hot plate with a magnetic stirring rod after mixing. The stirring keeps the powders mixed while precipitating out of suspension. The zirconia balls were removed using a sieve and rinsed of any residual powders with isopropanol. Batches with TZ-8Y ($Zr_{0.852}Y_{0.148}O_{1.926}$) as a precursor were also made. The ternary oxide replaces all ZrO_2 and partly the Y_2O_3 content of the starting mixture. The precursors and their respective supplier were otherwise always the same and are listed in Table 10.

Table 10: All precursors with supplier, purity, structure, and corresponding CAS-number.

Precursors	**Supplier**	**Purity**	**Structure**	**CAS**
$BaCO_3$	Sigma Aldrich	99%	Orthorhombic	513-77-9
$SrCO_3$	Alfa Aesar	99% (1% Ba)	Orthorhombic	1633-05-2
ZrO_2 (<5µm)	Sigma Aldrich	99.9%	Monoclinic	1314-23-4
CeO_2 (<50nm)	Sigma Aldrich	99.95%	Cubic	1306-38-3
Y_2O_3 (<20µm)	Alfa Aesar	99.9%	Cubic	1314-36-9
TZ-8Y (<40nm)	Tosoh	«high purity»	Tetragonal	--

The precursor mixtures were divided in three, one with no sintering additive hereby referred to as pristine samples, and the other two were added either 0.5 or 1 weight percent (wt.%) NiO and CuO as sintering additives. The powders with sintering aid were then re-mixed for 1h in a planetary ball-mill with 300rpm in a zirconia jar. Zirconia balls of 5mm diameter with approximate ratio of 10x the powder mass was added in addition to isopropanol to mix the powders. The sintering additives are presented in Table 11 and the relation between wt.% and mol% are presented in Table 12.

Table 11: Sintering additives.

Sintering additives	**Supplier**	**Purity**	**Structure**	**CAS**
NiO (<50nm)	Sigma Aldrich	99.8%	Cubic	13-13-99-1
CuO (micron)	Sigma Aldrich	99.9%	Monoclinc	1317-38-0

Table 12: Relation between weight percentage and mol percentage for sintering additive.

Sintering additives	**wt.%**	**mol%**
NiO	1	3.6
	0.5	1.8
CuO	1	3.4
	0.5	1.7

The powders were cold pressed uniaxially in steel dies with different diameters in a hydraulic press, Specac GS15011. Generally, a 20mm die was used, except for when sintering in pure oxygen (10mm) and for dilatometry studies (6mm). The applied pressure for each diameter is listed in in Table 13.

Table 13: Pressures and die diameters.

Pressure [MPa]	**Diameter [mm]**
90-100	20
50-60	10
10-20	6

To promote adhesion between the grains in the pressed pellet, 15-20 drops binder (paraloid acetate) per gram of powder was mixed into the powders in a mortar. The pressure was applied slowly and after 5-10 seconds it was released almost fully, before the same pressure was applied again. When delamination or other cracking occurred or was visible, the sample was crushed and pressed again.

4.1.2 Sintering

Four batches of green powders were mixed and processed as stated above. The pressed pellets were sintered with different sintering parameters, all included a 1-hour dwell at 450°C to combust the binder. For samples sintered in air a magnesia crucible was used, while those sintered in oxygen were enclosed in a ProboStat™ and required an alumina crucible.

Batch 1 is presented in Table 14 and the crucible setup is presented in Figure 15. The initial batch did not contain YSZ as a precursor, only binary oxides, and carbonates.

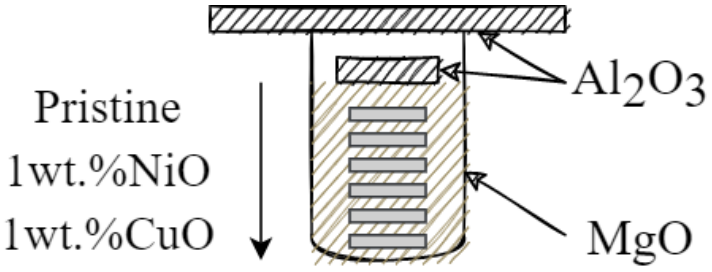

Figure 15: Crucible setup for the initial batch.

Table 14: Abbreviations, sintering temperature and time and sintering additives for the initial batch.

Abbreviation	**Sintering temp. & time**	**Sintering additive**	**Sacrificial powders**
BSZCYNi1	1400°C – 12h	1wt.%NiO	$BaZr_{0.7}Ce_{0.2}Y_{0.1}O_{3-\delta}$
BSZCYCu1		1wt.%CuO	
BSZCY1400		--	
BSZCY1600Ni1	1600°C – 12h	1wt.%NiO	
BSZCY1600Cu1		1wt.%CuO	
BSZCY1600		--	
BSZCYNi1(O2)	In oxygen atm. 1250°C – 1h 1400°C – 12h	1wt.%NiO	$BaZr_{0.8}Y_{0.2}O_{3-\delta}$ $+10wt.\%\ BaCO_3$
BSZCYCu1(O2)		1wt.%CuO	

Batch 2 included YSZ as a precursor, however a calculation error occurred between the initial amount of yttrium and TZ-8Y, which meant that the samples only contained 14mol% yttrium. These samples are therefore abbreviated with a star in Table 15. The setup for sintering in oxygen is depicted in Figure 16.

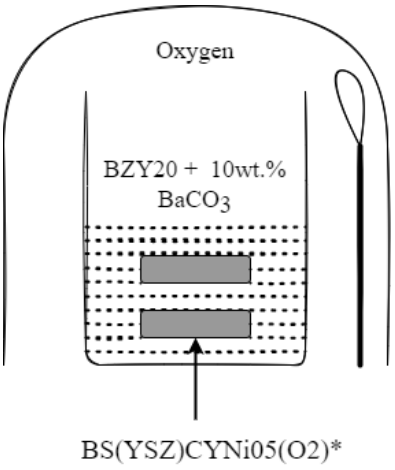

Figure 16: Crucible of alumina when sintering in oxygen

Table 15: Abbreviations, sintering temperature and time, and sintering additives for the second batch.

Abbreviation	**Sintering temp. & time**	**Sintering additive**	**Sacrificial powders**
BS(YSZ)CY1400*	1400°C – 12h	--	$BaZr_{0.7}Ce_{0.2}Y_{0.1}O_{3-\delta}$
BS(YSZ)CY1600*	1600°C – 12h	--	
BS(YSZ)CYNi05*	1600°C – 12h	0.5wt.%NiO	$BaZr_{0.8}Y_{0.2}O_{3-\delta}$ $+10wt.\%\ BaCO_3$
BS(YSZ)CYNi05(O2)*	In oxygen atm. 1450°C – 12h	0.5wt.%NiO	

The last two batches were made with similar sintering parameters for samples with and without YSZ as a precursor. In addition, sacrificial powders of the same composition were made by the stated mixing procedure, a calcination at 1200°C for 12 hours, and with the addition of 10wt.% $BaCO_3$ after calcination. These are presented together in Table 16 and the crucible setup is illustrated in Figure 17.

Table 16: Abbreviations, sintering temperature and time, sintering additives, and precursor for batch 2 and 3.

Abbreviation	**Sintering temp. & time**	**Sintering additive**	**Sacrificial powders**	**w/ or w/o YSZ**
BSZCYNi05	1250°C – 1h	0.5wt.%NiO	$Ba_{0.85}Sr_{0.15}Zr_{0.7}Ce_{0.1}Y_{0.2}O_{3-\delta}$	w/o
BSZCYCu05	1600°C – 12h	0.5wt.%CuO	$w/o\ YSZ$	w/o
BSZCY	1250°C – 1h	--	$+10wt.\%\ BaCO_3$	w/o
BS(YSZ)CY	1600°C – 24h	--	$Ba_{0.85}Sr_{0.15}Zr_{0.7}Ce_{0.1}Y_{0.2}O_{3-\delta}$	w/
BS(YSZ)CYNi05	1250°C – 1h	0.5wt.%NiO	$w/\ YSZ$	w/
BS(YSZ)CYCu05	1600°C – 12h	0.5wt.%CuO	$+10wt.\%\ BaCO_3$	w/

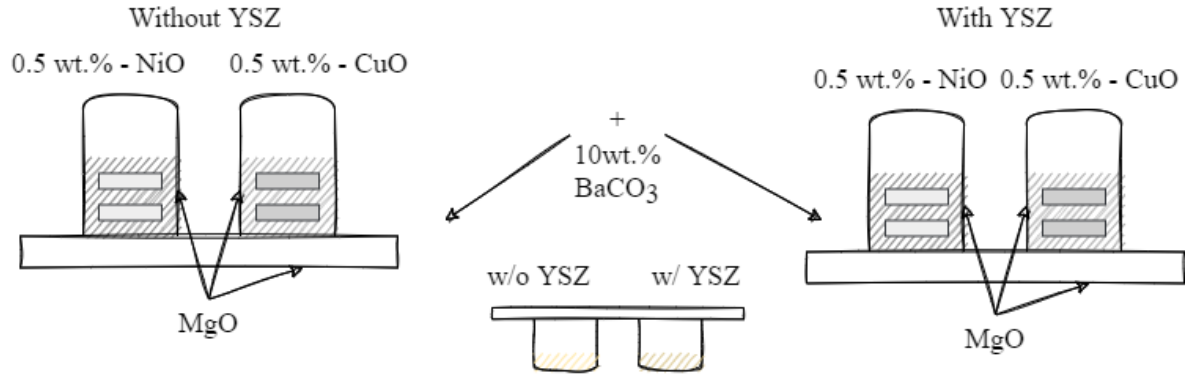

Figure 17: Samples sintered with and without YSZ with sintering aid and calcined sacrificial powders of same stoichiometry + 10wt.% $BaCO_3$.

4.1.3 Painting electrodes

Selected samples were painted with a platinum ink which was mixed to a slurry in ethanol. The paint was added in three layers with drying at 200°C for a couple of minutes in between. Afterwards, the samples were heat treated at 900°C for 1 hour to increase adhesion between the electrode layer and sample. The platinum electrodes were painted symmetrical to both sides of the sample. The samples that were painted are listed in Table 17 with electrode area and sample height, these are later used as dimensions when defining the specific area for resistance, conductivity, capacitance, etc.

Table 17: Pt-painted samples, electrode areas and sample heights.

Sample BSZCY151020	**Area [cm^2]**	**Height [cm]**
BSZCYNi1	0.17	0.107
BSZCYCu1	0.17	0.136
BS(YSZ)CYCu05	0.95	0.122

4.2 Characterization

Investigations in SEM, TG and XRD were used to characterize microstructure, hydration, and crystal structure, respectively. Mainly to get insight into the effect of fabrication, but also for additional information that can be associated to findings from EIS.

4.2.1 Dilatometry

Dilatometry is used to describe and detect macroscopic sintering mechanisms, as well as the degree of shrinkage. It measures length change in one dimension with temperature change over time. From the initial length the relative length change is given as:

$$\frac{dl}{l_0} = \frac{a_1 - a_2}{a_1} \tag{4.200}$$

where a_1 is the initial length, a_2 is the measured length. In this thesis the relative length change is presented in percentages.

The sintering profiles were investigated using a Dilatometer 402C from Netzsch (Germany) by measuring linear length change of a cylindrical pellet versus temperature and time. The 6mm pellets were put in the dilatometer furnace with 10mm diameter alumina spacers at each side before the pushrod was put in place with a constant pressure of 30cN (Figure 18). In this setup no sacrificial powders are used, and the sample is in direct contact with alumina, these samples are therefore discarded after measurement. Usually 1550-1600°C was used for the dilatometer furnace. Dilatometry studies were used to determine sintering conditions.

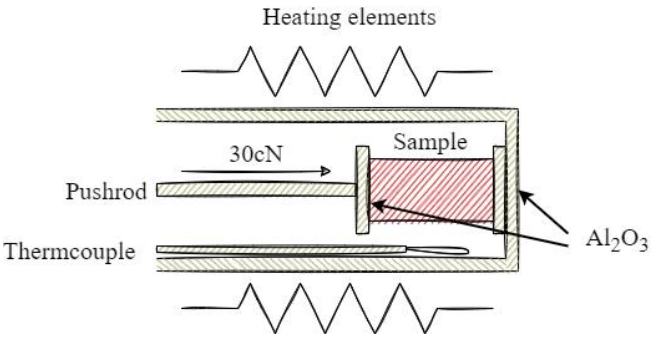

Figure 18: Dilatometer setup.

4.2.2 X-Ray diffraction

X-ray diffraction was performed using a D8 Advance diffractometer with DaVinci design with Lynxeye detector with CuKα-1 (λ = 1.54060 Å) and CuKα -2 (λ = 1.54439 Å) radiation. The analysis was performed on every single composition of sintered BSZCY151020 in the range of $20° \leq 2\theta \leq 90°$ with time steps between 0.1-0.5s per degree. The analysis was done to identify the phases of each sample. Typically, phases above 1wt.% of the composition should be visible in the pattern.

In preparation, the pellets were crushed to fine powders using a mortar. Isopropanol was used to suspend the powders before dripping them on the XRD sample container with a pipette. The obtained patterns were processed in DIFFRAC.EVA V4.3 by comparison to the Crystallography Open Database (COD) and to Powder Diffraction Files (PDF) from the International Centre for Diffraction Data. The lattice parameter was extracted by means of manually applying Bragg's Law, and by Rietveld refinement in the program TOPAS with Lorentz function.

4.2.3 High-Temperature X-Ray diffraction

To investigate the phase transitions during sintering, green powders of BSZCY151020 without YSZ and sintering additive were analysed using an in-situ X-ray diffraction technique. The HT-XRD data were collected by a D8 A25 diffractometer equipped with a Lynxeye XE detector for high energies, with Mo*K*α-1 (λ = 0.70930 Å) and Mo*K*α-2 (λ = 0.71359 Å) radiation. The temperature was controlled by an Anton Paar HTK1200 furnace with an alumina plate sample holder under ambient air. The measurement was conducted from room temperature to 1200°C with 50°C intervals up until 900°C, followed by 5°C intervals until 1200°C. All measurements were done between $10° \leq 2\theta \leq 30°$ and the heating rate was 2°C/min. The following peaks

were evaluated by comparison to PDF from a crystallographic database in DIFFRAC.EVA V4.3.

4.2.4 Thermogravimetry

Water uptake (hydration) studies for selected samples were performed in a Netzsch Tarsus 401 thermobalance with 10ml/min flow of protective argon gas. The samples were initially subject to 900°C in air flowed through a drying stage (P_2O_5 powders) to dehydrate the samples. After equilibrium was reached, the gas was switched to air humidified in a bubbler with deionised water saturated with KBr salt $\left(p_{H_2O} \approx 0.026atm\right)$. Then the sample was cooled down to room temperature with 50°C or 100°C steps. Each isotherm was maintained for 0.5-3 hours, increasing in time with decrease in temperature to promote that equilibrium was reached. The flow of gas was 40ml/min, and the cooling rate between the isotherms was 3°C/min.

Proton concentrations were extracted from relative mass changes acquired from the TG measurements. The mass gain was attributed the hydration reaction (2.102) and was converted to mol percent OH per mol BSZCY151020 by equation (4.201), where Δm_{sample} is the mass change, M the molar mass of the composition, and m_{inital} is the initial mass of the measured samples.

$$mol\frac{OH_O^{\cdot}}{BSZCY151020}\% = 2\frac{dm_{sample}\,M_{BSZCY151020}}{M_{H_2O}\,m_{initial}}\% \qquad (4.201)$$

Equilibrium at 900°C in dry air was used as the initial reference point for hydration. A data point for each isothermal from 800-400°C was extracted and used for fitting in a van't Hoff plot to obtain values for enthalpy and entropy, according to (2.305). In addition, the maximum hydration (obtained below 300°C) were used to determine the effective acceptor doping, $\left[Y'_{Zr,eff}\right] = \max\left[OH_O^{\cdot}\right]$.

The thermodynamic parameters were also extracted using the expression for proton concentration (2.310) and applying the equilibrium expression (2.305) as a secondary equation in the mathematical fitting program, Table Curve 2D (StarCom Information Technology Limited). Now utilizing the whole data range obtained from TG (900-200°C) and not constraining the effective acceptor doping as a fixed value in the equilibrium expression (2.309). Accordingly relative proton concentration from TG was fitted as a function of inverse temperature. The following results were also used to determine the relative concentrations of oxygen (2.303) and oxygen vacancies (2.311).

4.2.5 Scanning electron microscopy

Cross sectional fractures of samples sintered in high temperature furnace were investigated with a field-emission scanning electron microscopy (Fei Quanta 200 FEG-ESEM) to determine grain size, morphology, and phase purity. The main analysis was done with mixed backscatter and secondary electron configurations with 15-25k acceleration voltage at suitable magnifications. The mean grain size was analysed by image analysing software (ImageJ) by extracting diameters in four directions for each grain and by drawing the grain areas.

For one representative sample the grain size distribution of a crushed pellet was also investigated prior to thermogravimetric analysis.

4.3 AC characterization

4.3.1 Measuring cell

The measuring cell is supplied by NORECS and is referred to as a ProboStat^{TM}. It's a cylindrical cell consisting of an inner and outer chamber of alumina with separate gas inlet and outlet, one in and out for each chamber. The outer chamber can field three electrodes and two thermocouples, while the inner cell can field one electrode and one thermocouple.

A 4-wire 2-electrode setup with symmetrical electrodes was used for all EIS measurements, where the four wires are high and low current (HC and LC), and high and low voltage (HV and LV). The wires were connected to platinum mesh current collectors, which were placed on the Pt-painted electrodes and hold in place by an alumina top piece suspended by 3 springs. The cell is illustrated in Figure 19 where the sample sits between the inner and outer chambers.

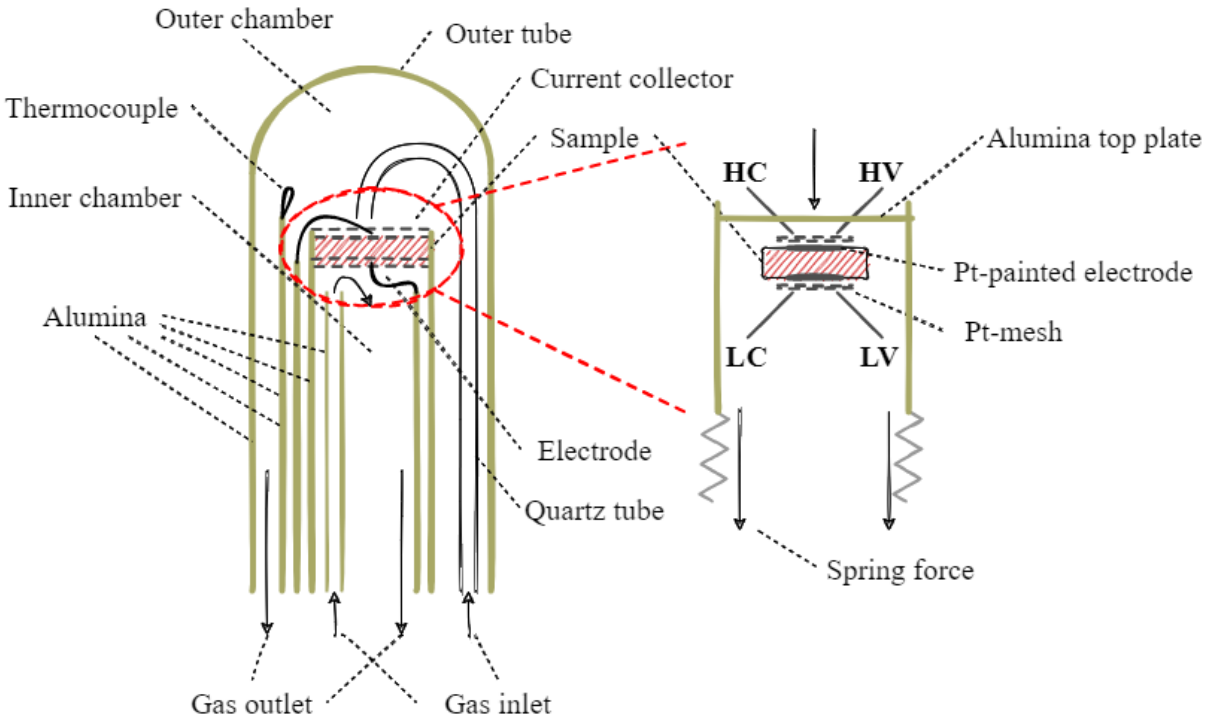

Figure 19: Alumina measuring cell setup with symmetrical platinum electrodes, platinum current collectors, thermocouple, quartz tube for directed gas flow and alumina chambers.

4.3.2 Gas mixer

The atmosphere in the ProboStat^{TM} was controlled by gas flow from a gas mixer. The gas mixer consists of 4 pairs of Brooks flowmeters, making up Mix 1, 2, 3, and 4, as illustrated in Figure 20. The three first are for mixing and dilution of gasses, while the last has the option to either humidify or dry the gas, this can also be bypassed. The wetting stage consists of two bubblers, the first with deionised water and the second with deionised water saturated with potassium bromide salt. The salt insures a lower partial pressure of water such that condensation in the copper tubing is avoided. The partial pressure is approximately 0.026atm after wetting at room temperature.

The drying stage is a glass flask filled with P_2O_5, which acts as desiccants. The system pressure is closed by mineral oil bubblers that ensure overpressure, these are situated after each mixing stage (Mix # out) and lets out excess gas.

The gas was under all measurements evenly distributed to the inner and outer chamber of the ProboStat^{TM}.

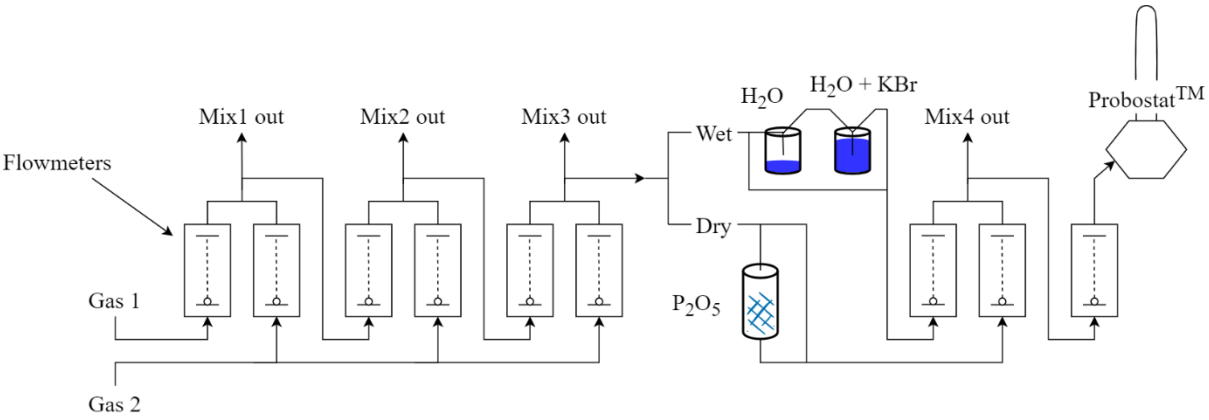

Figure 20: Gas mixer with mixing and dilution stage (mix 1, 2, 3), and wetting and drying stage (mix 4).

The software ProGasMix v.0.7.1 was used to calculate flow values needed to obtain certain partial pressures of oxygen. Oxygen (Gas 1) was diluted with argon (Gas 2) with different ratios of flow to obtain p_{O_2} between $1 - 10^{-5} atm$. The same procedure was used to obtain p_{O_2} between $10^{-5} - 10^{-25} atm$ by diluting harmix with argon. The latter values varied by temperature as the gas was also humidified.

4.3.3 Deconvolution

The EIS spectra were deconvoluted using Zview® v3.5 (Scribner) by fitting the data to equivalent circuits. At low temperatures ($< 350°C$) a high-, mid-, and low-frequency response were observed in the form of semicircles attributed to bulk, grain boundary and electrode. The bulk and grain boundary semicircles were deconvoluted with RC or RCPE elements, while the electrode was deconvoluted with the element best fitting the data, varying between open and closed Warburg, and RCPE elements. At high temperatures ($> 350°C$) the bulk contribution consisted solely of an ohmic response. Impedance at 10kHz was used as a means to predict the total resistance of the sample, as it normally sits around the high intercept of the GB semicircle.

4.3.4 Conditions and measurements

Selected samples were measured from high to low temperatures in humid and dry conditions. Measurements were conducted from 1000°C to 100°C, and at one instance to room temperature. The ProboStat™ was heated with a tube furnace, and for low temperatures ($< 250 - 100$°C) a heating mantel.

EIS measurements were also carried out under different partial pressures of oxygen ranging from approx. $1 - 10^{-25} atm$. This was done at 400, 600, 800 and 1000°C.

The sample resistance was monitored between different temperatures and atmospheres by time measurements at constant frequency (10kHz). This was done to check if the sample had reached chemical equilibrium.

4.4 Processing of data

The data obtained from EIS was organised and analysed in Excel as bulk, grain boundary, specific grain boundary (Brick layer model) and total conductivity. Linear regressions of $log(\sigma T)$ versus $\frac{1}{T}$ according to Arrhenius expression (2.211) were used to extract activation energies (slope) and pre-exponentials (intercept).

This chapter explains the approach of extracting initial values for pre-exponential and enthalpy of mobility for protons, oxygen vacancies and holes. To gain insight into the charge carrier contributions of the conductivity data, initial assumptions and extractions are done to obtain isolated mobility parameters before fitting conductivity (2.201) with expressions for each charge carrier with Table Curve 2D (StarCom Information Thecnology Limited). Since the conductivity alone typically don't expose the transport contribution of a particular charge carrier the initial mobility parameters are fitted to the experimental data according to the expression for conductivity (2.201) with Table Curve 2D (StarCom Information Technology Limited). This is done to obtain a correlating set of pre-exponentials and mobility values, effectively modelling the experimental data in all conditions to obtain one set of parameters for one specific sample. These parameters being pre-exponentials and mobility enthalpies, for holes it would be the activation enthalpy. The procedure of fitting the total model of all partial conductivity contributions is explained at the end of this section.

4.4.1 Ionic charge carrier parameters

The apparent activation energy of the conductivity in humid argon was extracted by Arrhenius expression as the proton mobility enthalpy (2.209) in the temperature interval 400-100°C. At this temperature proton concentration is approximately constant and at its maximum, as observed from TG measurements, which means $\Delta H_{a,OH_O^{\cdot}} \approx \Delta H_{mob,OH_O^{\cdot}}$ (2.216) and oxygen vacancies can be assumed a minority charge carrier. The obtained pre-exponential ($\sigma^0_{OH_O^{\cdot}}$ $[S\ K\ cm^{-1}]$) was converted to the pre-exponential of mobility (u_0 $[cm^2 K\ V^{-1}s^{-1}]$) via the Nernst-Einstein relation (2.215).

The same procedure was used to extract enthalpy ($\Delta H_{mob,v_O^{\cdot\cdot}}$) and pre-exponential ($u^0_{v_O^{\cdot\cdot}}$) of mobility for oxygen vacancies in dry air from 500-1000°C, assuming that protons are a minority charge carrier.

4.4.2 Electronic charge carrier parameters

The hole formation and mobility enthalpy are tangled together (2.314) which means that the apparent activation energy consists of the two. From pO_2 – dependency measurements in humid atmospheres at 600, 800 and 1000°C a dependency close to ¼ of log (p_{O_2}) for conductivity was observed, as illustrated in Figure 21. At low pO_2 the conductivity is independent of oxygen pressure and was assumed to be dominated by ionic conductivity. To retrieve the conductivity of holes, the ionic contribution (flat region) was subtracted from the total conductivity at approx. 1atm of pO_2.

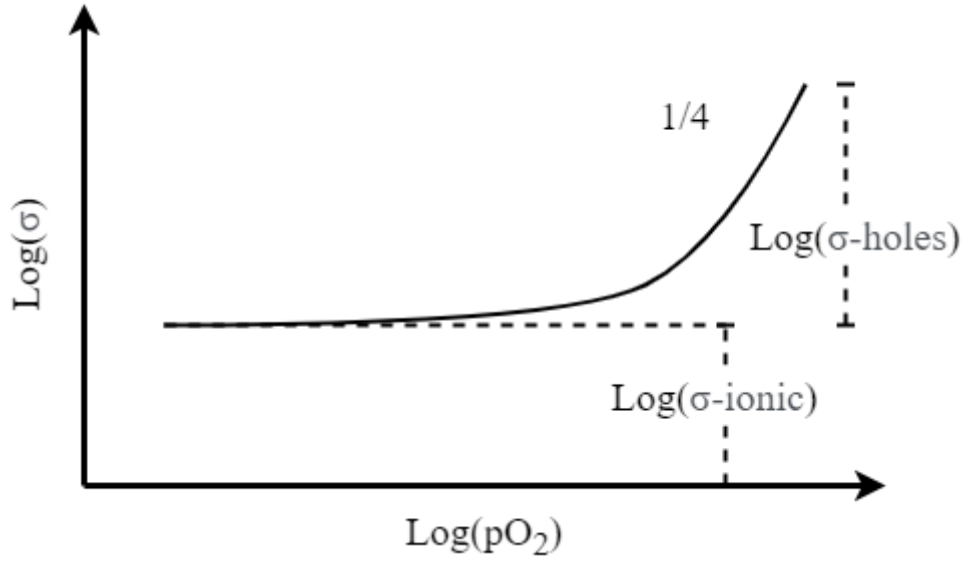

Figure 21: Observed total conductivity in varying atmospheres at temperatures above 600°C and the different contributions (dashed lines).

The hole conductivity was then plotted versus temperature and the hole contribution was extracted by Arrhenius expression, yielding the pre-exponential and enthalpy of activation. These values were used as initial values for the total model of conductivity in the next section.

4.4.3 Modelling partial conductivities

Using Table Curve 2D the expression in Figure 22 were fitted to the conductivity data obtained in humid argon, dry air and in different pO_2 as $log(\sigma)$ (Y) versus $\frac{1}{T}$ (X). The unknown parameters $u^0_{OH_O^{\cdot}}, \Delta H_{OH_O^{\cdot},mob}, u^0_{v_O^{\cdot\cdot}}, \Delta H_{v_O^{\cdot\cdot},mob}, \sigma_p^0$ *and* $\Delta H_{p,a}$ were given the initial values as

obtained above and were given suitable upper and lower boundary limits depending on the uncertainty of the initial value. For example, proton mobility, which has a relatively low uncertainty, was given $\pm 4kJ\ mol^{-1}$ to adjust.

As conductivity ($\sigma_i = u_i c_i F \rho_O$) is a function of concentration, the enthalpy and entropy of hydration (obtained from TG) were added as fixed parameters to give the proton concertation and oxygen vacancy concentration as a function of temperature.

To obtain a good fit with all conductivity data in the different atmospheres the data sets were fitted to each one, cycling back and forth until the parameters converged at appropriate values representing the complete set of data as closely as possible. The final fitting was done with the humid argon conductivity, and it is from this the R-square error value is presented.

a) $K_{hydr} = e^{\left(-\frac{\Delta H_{hydr}}{RT}\right)} e^{\left(\frac{\Delta S_{hydr}}{R}\right)}$

b) $[OH_O^{\cdot}] = \frac{3Kp_{H_2O} + \sqrt{Kp_{H_2O}\left(9Kp_{H_2O} - 6Kp_{H_2O}[Y_{Zr,eff}] + Kp_{H_2O}[Y_{Zr,eff}]^2 + 24[Y_{Zr,eff}] - 4[Y_{Zr,eff}]^2\right)}}{Kp_{H_2O} - 4}$

c) $[v_O^{\cdot\cdot}] = \frac{[Y_{Zr,eff}] - [OH_O^{\cdot}]}{2}$

d) $u_{OH_O^{\cdot}} = u^0_{OH_O^{\cdot}} \frac{1}{T} \exp\left(-\frac{\Delta H_{OH_O^{\cdot},mob}}{RT}\right)$

e) $\sigma_{OH_O^{\cdot}} = [OH_O^{\cdot}] F \rho_O u_{OH_O^{\cdot}}$

f) $u_{v_O^{\cdot\cdot}} = u^0_{v_O^{\cdot\cdot}} \frac{1}{T} \exp\left(-\frac{\Delta H_{v_O^{\cdot\cdot},mob}}{RT}\right)$

g) $\sigma_{v_O^{\cdot\cdot}} = [v_O^{\cdot\cdot}] F \rho_O u_{v_O^{\cdot\cdot}}$

h) $u_p = \left(\sigma_p^0\right) \frac{1}{T} [v_O^{\cdot\cdot}]^{\frac{1}{2}} [O_O^x]^{-\frac{1}{2}} p_{O_2}^{\frac{1}{4}} \exp\left(-\frac{\Delta H_{p,a}}{RT}\right)$

i) $\sigma_p = u_p F \rho_O$

$Data$:

$X = \frac{1}{T}$

$Y = Log\left(\sigma_{OH_O^{\cdot}} + \sigma_{v_O^{\cdot\cdot}} + \sigma_p\right)$

$Parameters$: $A0 = u^0_{OH_O^{\cdot}}, A1 = \Delta H_{OH_O^{\cdot},mob}, A2 = u^0_{v_O^{\cdot\cdot}}, A3 = \Delta H_{v_O^{\cdot\cdot},mob}, A4 = (\sigma_p^0)$ and $A5 = \Delta H_{p,a}$

Fixed parameters: ΔH_{hydr} and ΔS_{hydr}

$Constants$: $R, F, \left[Y'_{Zr,eff}\right], \rho_O, [O_O^x]$

Figure 22: Full conductivity model.

4.5 Error and uncertainties

In the presented fabrication and characterisations methods there are several possible errors, some easier accounted for then others. While some errors will be inherent to the procedure others can be identified and minimized. The latter is the aim and focus of this chapter.

There is an uncertainty of $\pm 0.1mg$ for the pression weight, which is small relative to the possible execution errors. Contaminates from surroundings and equipment are expected to a small degree, to minimize the introduction of foreign impurities zirconia mixing balls and zirconia planetary mill container was used. Although clean, mortars, crucibles, tweezers, dies etc. were wiped with isopropanol before use.

Thermogravimetric measurements might suffer mass change because of buoyance effect, this could be accounted for by measuring a substance that does not exhibit mass change in the applied conditions, such as alumina powders in an alumina crucible. However, since the effect is so small compared to the mass change in the samples this was regarded as an insignificant error.

The gas mixer used to set the atmospheric conditions in the ProboStat™ is associated with several errors and uncertainties. The flowmeters have an uncertainty of $\pm$ 5%. The gas that is flowed through the drying stage is expected to have $p_{H_2O} < 10^{-6}$, but was found to be approx. $p_{H_2O} \approx 3 \times 10^{-5}$ by Kofstad and Norby [55]. As an approximate value $p_{H_2O} = 10^{-5}$ was used when fitting conductivity in dry conditions. Furthermore, the high purity argon gas used is expected to have $p_{O_2} \approx 2 \times 10^{-6}$. When calculating partial pressures of oxygen with ProGasMixer a leakage of $p_{O_2} \approx 10^{-5}$ was included.

Since the samples are prone to change from the surrounding conditions isothermal equilibriums were used to determine mass change in TG and impedance in EIS. To check the equilibrium in the ProboStat™, constant 10kHz time measurement was run between each EIS sweep to determine if resistance was stable. At high temperatures (>900°C) drift in resistance was observed for the time measurements which indicates that the sample undergoes small changes and thus the characteristic impedance and conductivity will drift between measurements. Which affects results and subsequent fittings, especially when considering the total model of partial conductivities.

The mathematical modelling of partial conductivities is subject to a large variation in saddle points because of the nature of parallel conductivities. By performing a cycle of fittings with different experimental data the parameters are narrowed down to reasonable values, which are compared with literature. Thus, obtaining the most realistic set of parameters for the model. Another physical error is the drift of electrolyte resistance over time, especially at high

temperatures where defect mechanisms and microstructure are prone to change. Degrading electrode – electrolyte interface may also affect the conductivity that is obtained.

A certain amount of error must be expected from equipment not recently calibrated. This applies for thermocouples in furnaces, impedance analysers, etc. Since two different impedance analysers were utilized for EIS measurements, namely Novo Control and Solartron 1260, a deviation between results is expected. However, the deviation was shown to be insignificant when comparing the two with a familiar circuit, only slight change in characteristics at high frequency was observed.

5 Results

In this section, the most relevant findings are presented. Because of the large quantity of results a portion of the findings have been placed in Appendix B: Supplementary results. These will be referred to as Figure S # or Table S # in the text that follows.

The first section is mainly orientated towards synthesis and sintering outcome, with the sintering techniques, dilatometry and HT-XRD, coupled with material characterisation. This is followed by the findings from AC characterisation.

5.1 Samples

Samples that were sintered with the use of sintering aid showed high density. With a few exceptions, the density when using both 0.5 and 1.0 weight percent CuO and NiO was above 90%. These samples were always dark in colour and maintained their cylindrical shape post sintering. While the pristine samples sintered for 24 hours showed densification and dark colour, the ones sintered for 12 hours were either cracked or disformed and had a lighter yellowish colour when retrieved from the furnace with next to no densification. Either way, pristine samples that left the furnace intact were subject to cracking over time in ambient air and when stored in a desiccator. Consequently, their densities were not obtained.

Images of different samples are presented in Figure 23, showing the visible difference between pristine samples and samples with sintering additive. All relative densities can be found in Table S 1.

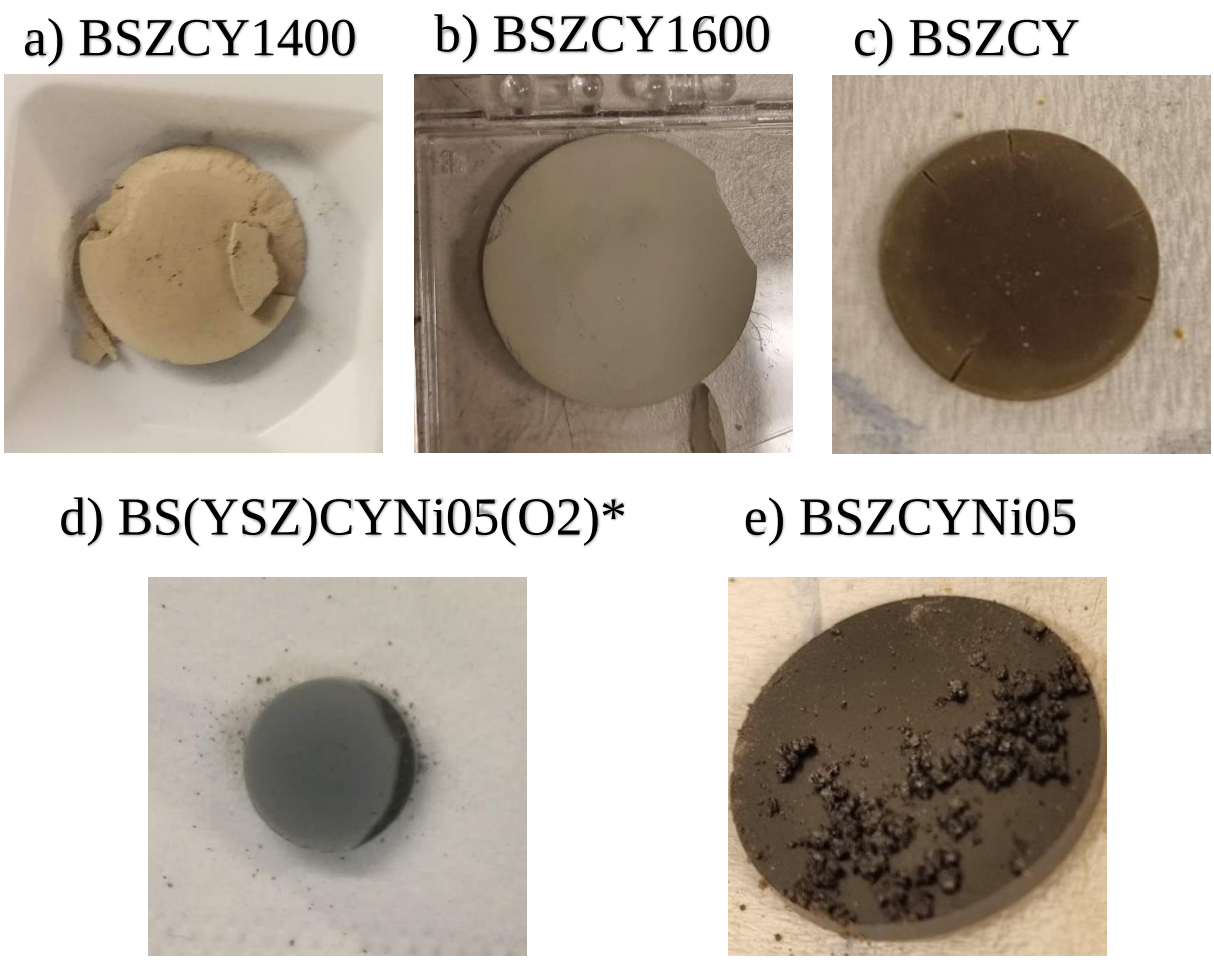

Figure 23: Pristine samples sintered at a) 1400°C – 12h, b) 1600°C – 12h, and c) 1600°C – 24h. While d) BS(YSZ)CYNi05(O2)* and e) BSZCYNi05 are representations of samples with sintering additive, respectively sintered in oxygen and air.

5.2 Dilatometry

The one-dimensional length change for the initial batch (BSZCY, BSZCYNi1 and BSZCYCu1) are presented in Figure 24. Note that BSZCYCu1 was investigated at a lower maximum temperature (1550°C) due to furnace limitations.

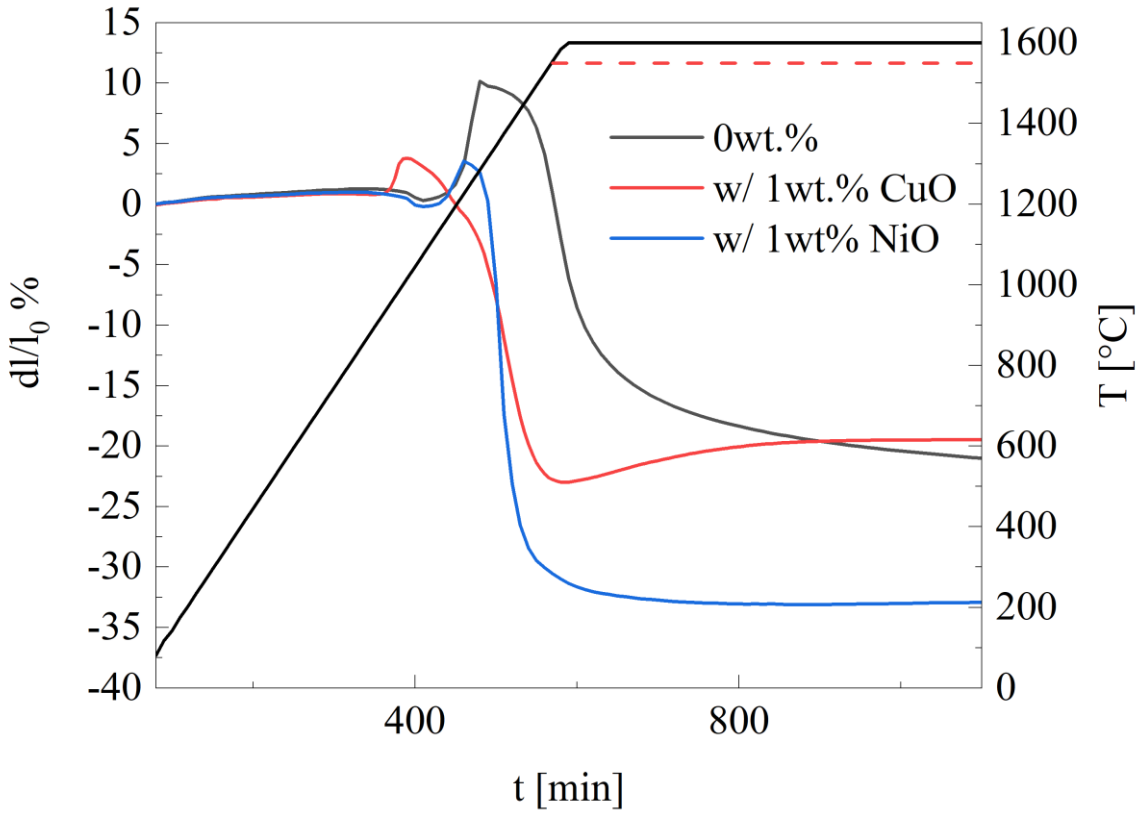

Figure 24: Dilatometry results for BSZCY, BSZCYNi1, and BSZCYCu1. The red dashed line is the maximum temperature (1550°C) of the measurement with CuO.

The initial expansion is due to decomposition of carbonates, where the carbon dioxide to a degree is trapped in the sample. This is evident when looking at the elongated peaks in Figure 25 at the 1250°C isothermal. With sintering aids, the peak is depressed as sintering initiates at a lower temperature. These effects are also seen for the comparison study of using YSZ as a precursor in Figure 25. In the following plots, the black line is without, and the green line is with YSZ as a precursor. For both BSZCY and BSZCYNi05, an initial shrinkage can be observed with an onset at 1030°C, indicating a phase transition that portrays volume shrinkage. The Zirconia transformation from monoclinic to tetragonal was believed to be the reason, as it is a martensitic transition with volume decrease [56]. To investigate the transition temperature a pure pre sintered zirconia pellet was cycled between 900°C and 1200°C. The results show an initial length change of around -1% with onset at 1175°C and the reverse transition at approx. 940°C, which repeated at subsequent cycles with slight deviation to length change, see Figure S 1.

A significant decrease for the onset temperature of expansion is observed for the BSZCYCu05 and BS(YSZ)CYCu05 (Figure 25c)) samples, which is attributed the reduction reaction of copper:

$$CuO \rightarrow Cu_2O + \frac{1}{2}O_2 \tag{5.200}$$

Which likely conceals the initial shrinkage observed for BSZCY without YSZ (Figure 25a, b). The onset around 955°C fits well with copper oxidation diagrams [57].

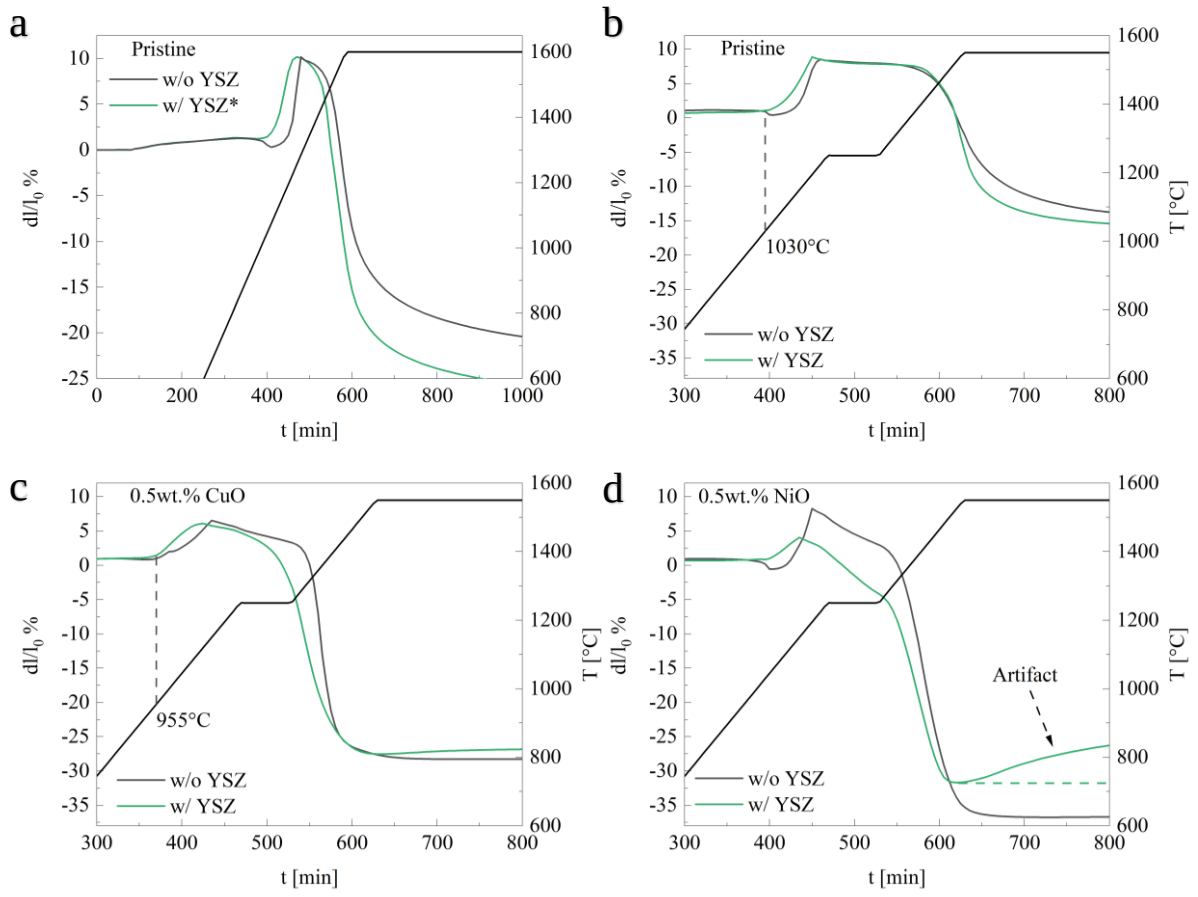

Figure 25: Dilatometry results for samples with and without YSZ as a precursor from batch 2 (14mol% yttrium) (a), and from batch 3 and 4, pristine (b), 0.5wt.% CuO (c), and 0.5wt.% NiO (d). Green lines are with YSZ and black are without.

The shrinkage of the CuO and NiO samples are considerable higher than the pristine pair in Figure 25, and it is reached faster. While the pristine samples densify over a longer period. The maximum shrinkage and corresponding relative densities for pellets sintered in a high temperature furnace with sacrificial powder are presented in Table 18.

Table 18: The mean relative densities of two sintered pellets for each composition measured geometrically compared to shrinkage from dilatometer with maximum furnace temperature in brackets.

Samples	**Sintering Temp. & Time**	**Sintered R.D.%**	**Shrinkage from dilatometer %** $[T_{max} = 1550°C]$
BSZCYCu05	1600°C – 12h	97	-28
BS(YSZ)CYCu05		89	-26
BSZCYNi05		96	-36
BS(YSZ)CYNi05		92	-25
BSZCY	1600°C – 24h	--	-14
BS(YSZ)CY		--	-16
			$[T_{max} = 1600°C]$
BSZCY*	1600°C – 12h	--	-21
BS(YSZ)CY*		--	-26

The results, show that using YSZ as a precursor increases densification to a small degree for pristine samples, while with sintering additive the trend is opposite. For the NiO containing sample the decrease in shrinkage is significant when adding YSZ, while for CuO the decrease is most significant in the R.D. of the sintered samples. Because of discrepancies in the dilatometry measurement and geometrical calculations of R.D. the trends are mainly what can be deduced from these results.

5.3 Microstructure

5.3.1 XRD

Selected X-ray diffraction results are presented here as all samples showed the perovskite structure with space group Pm-3m. Three samples had a visible secondary phase, BSZCY1400, BSZCY and BS(YSZ)CY which showed the $SrZrO_3$ perovskite phase of same space group. The $SrZrO_3$ phases were not visible in SEM.

The X-ray diffraction patterns of pellets sintered at 1400 and 1600°C for 12 hours are presented in Figure 26, the star indicates the secondary phase of $SrZrO_3$. Additionally, batch 3 and 4 samples are presented in Figure 27, with similar indications of the secondary phase.

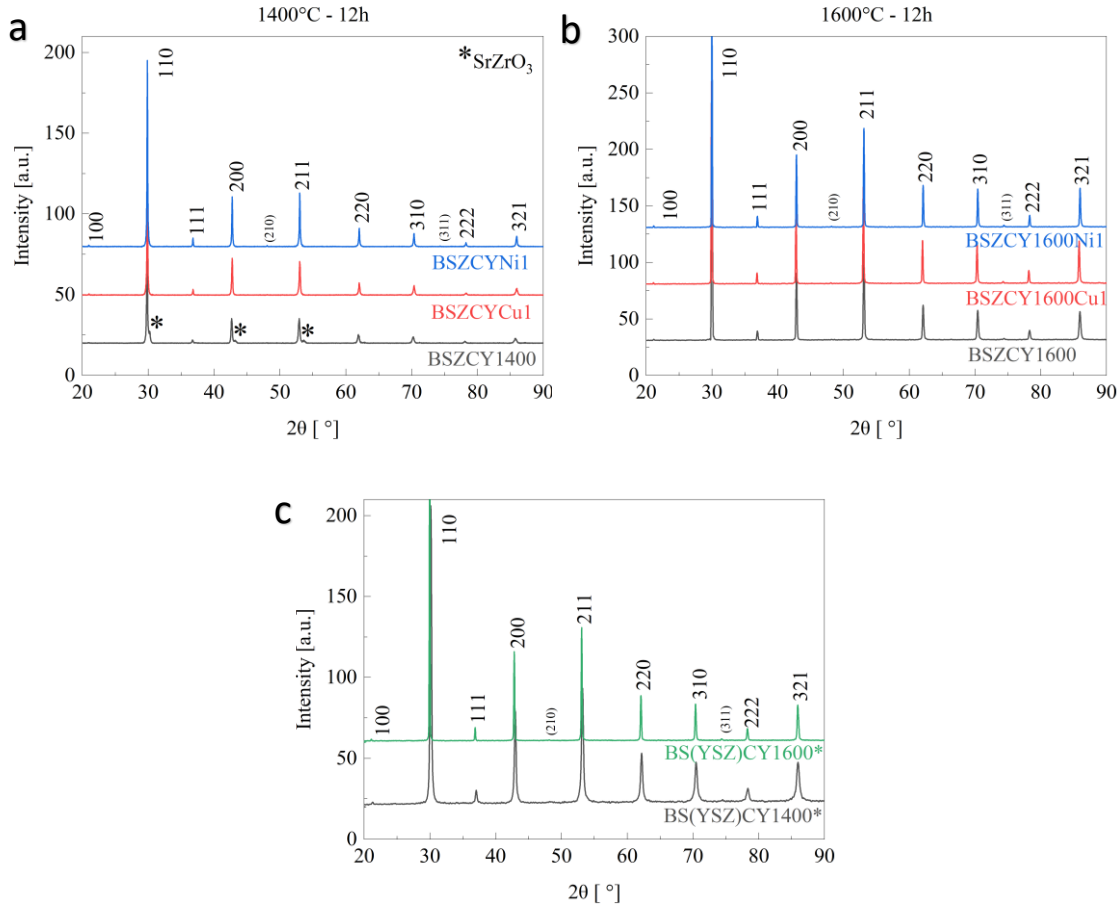

Figure 26: XRD patterns for samples sintered for 12 hours at a) 1400°C, b) 1600°C and c) with and without YSZ at both temperatures.

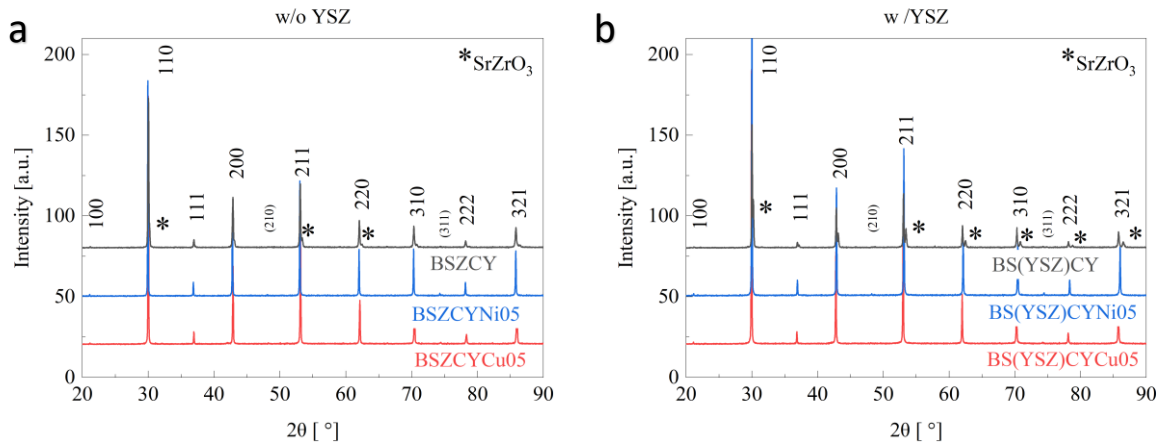

Figure 27: XRD patterns for samples without (a) and with YSZ (b) as a precursor, respectively batch 3 and 4.

The lattice parameter for each sample was extracted by refinement in TOPAS v.5.0 with the Rietveld method. The mean value was found to be 4.233Å, and was used to calculate theoretical density:

$$\rho = \frac{Mm}{N_a\, a_0^3} \tag{5.300}$$

The theoretical density was approx. $5.97 g\ cm^{-3}$, which was used to find oxygen density (ρ_O) and to calculate relative densities. The lattice parameter was used as a mean value because of unknown hydration of the sample at the time of measurement.

5.3.2 SEM

BSZCY1400 and BSZCY1600 exhibited no significant densification, which is confirmed by SEM analysis, presented in Figure 28. The grains size increases slightly with temperature, but both samples remain porous.

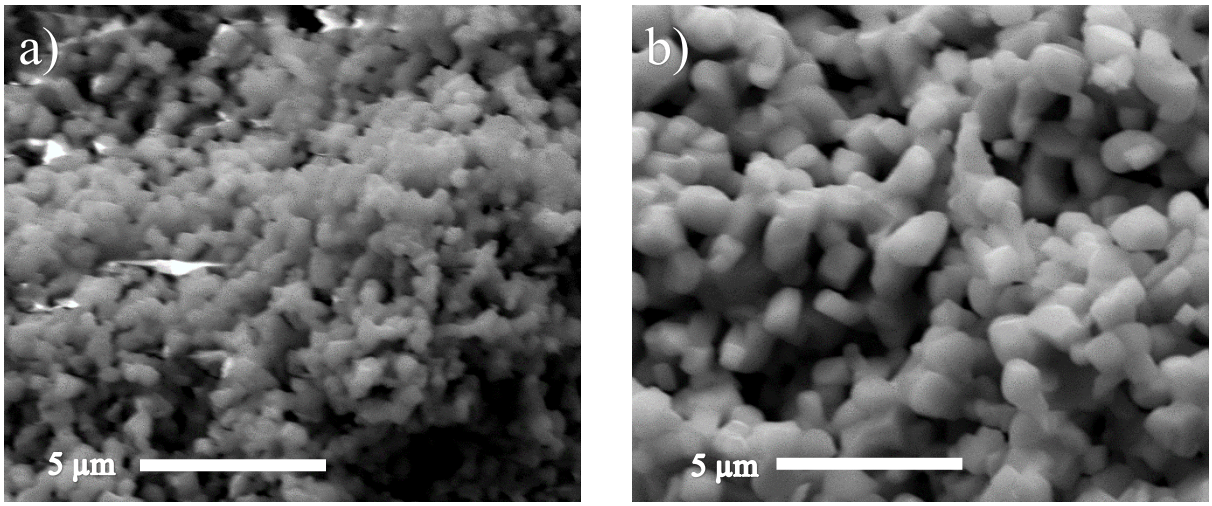

Figure 28: SEM images of a) BSZCY1400 and b) BSZCY1600.

BSZCYCu1 shows segregation of a secondary phase, mainly situated in the grain boundaries, while BSZCYNi1 shows no secondary phase (Figure 29). The segregates are probably CuO as they are not visible in any other sample.

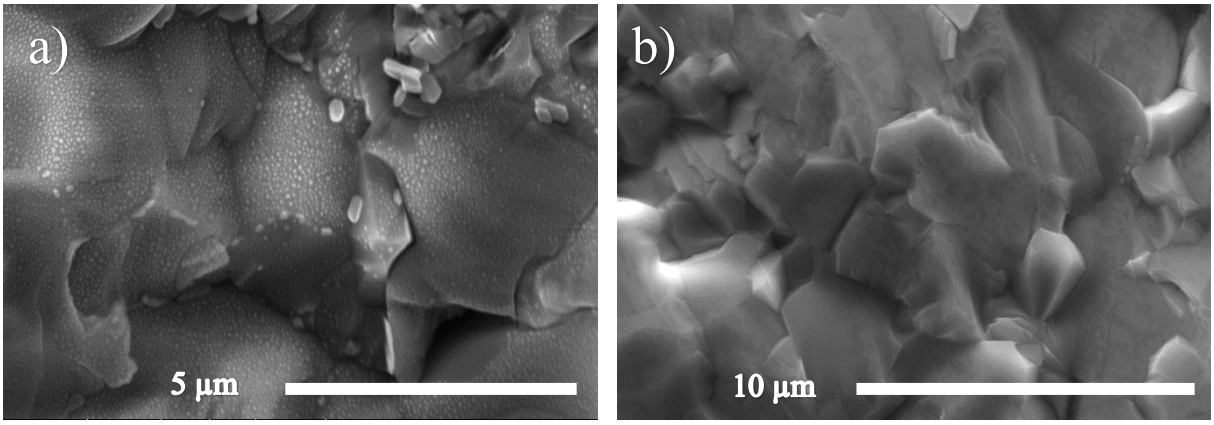

Figure 29: Secondary electron images of cross section fracture of a) BSZCYCu1 with segregation around grain boundary and b) BSZCYNi1 with no segregation.

BSZCYNi1 and BSZCYCu1 samples were also investigated by SEM after EIS measurements (Figure 30). The secondary phase in BSZCYCu1 is no longer visible and have dissolved into the structure. This is related to the cycling between reducing and oxidising atmospheres at high temperatures during EIS, especially under pO_2 dependency measurements, which allows copper to stabilise into the structure or grain boundaries. Or copper oxide leaves the sample as it is volatile at elevated temperatures.

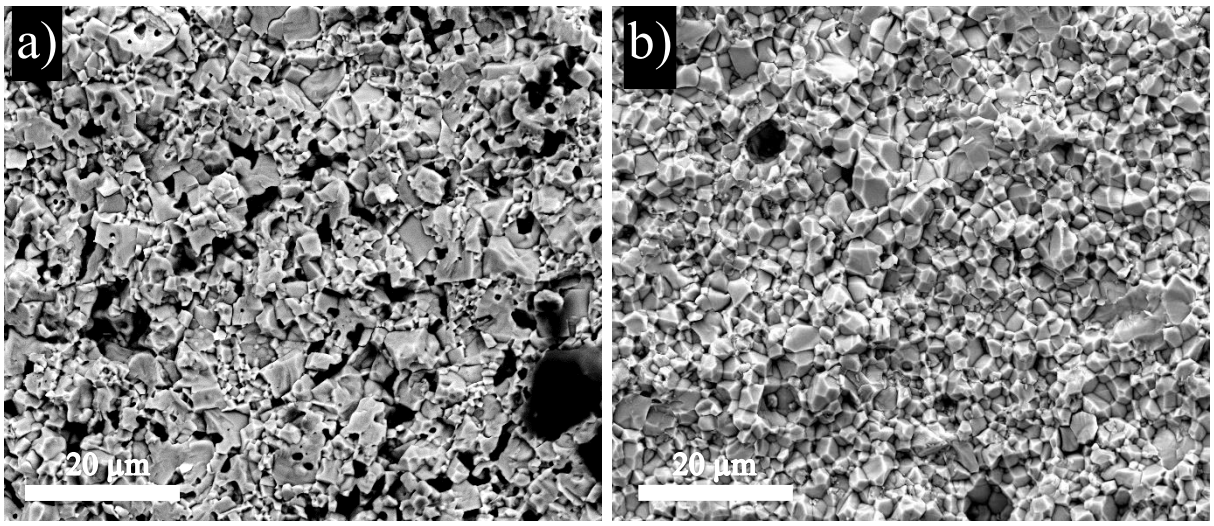

Figure 30: a) BSZCYCu1 and b) BSZCYNi1 post EIS measurements at maximum temperature 1000°C in Argon, Harmix and Oxygen.

The samples sintered with an extra isothermal at 1250°C for 1hour are pictured in Figure 31. Comparing the samples with image processing software (ImageJ) yields an estimate of grain sizes, which are presented in Table 19. All samples containing YSZ as a precursor have bigger grains compared to the samples to the same composition without YSZ. Qualitatively this is also visible in Figure 31.

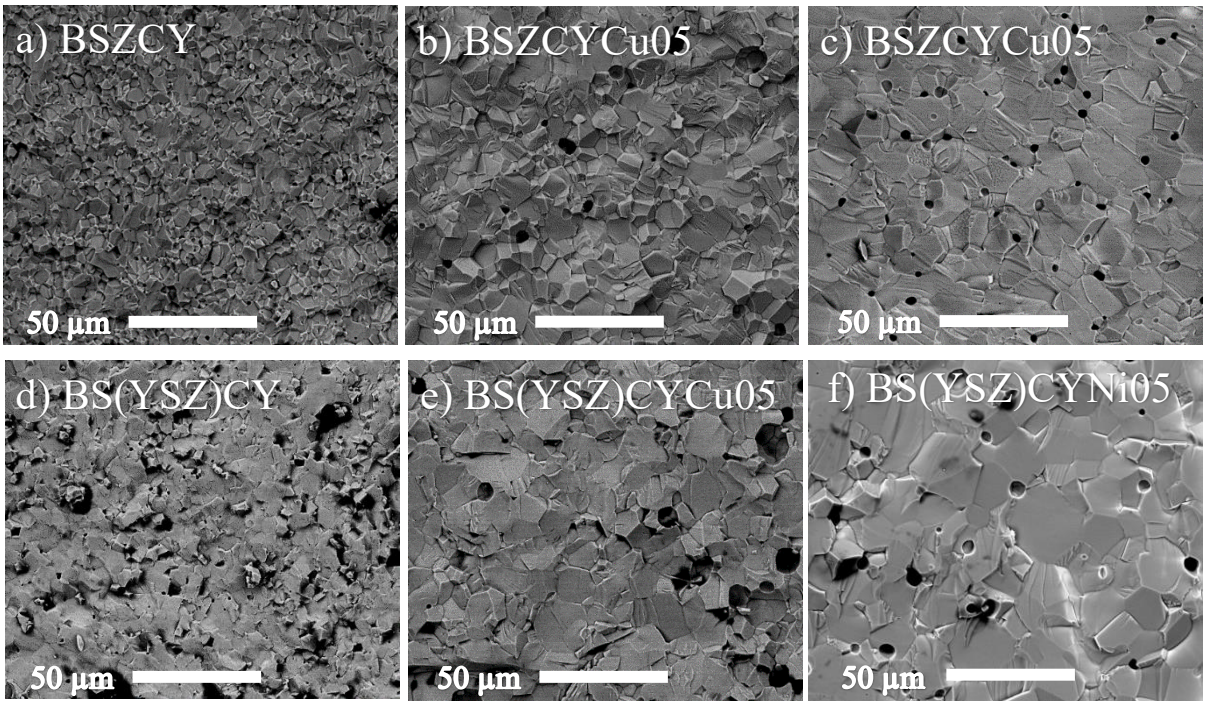

Figure 31: Mixed (SE & BSE) SEM pictures with 1000x lens magnification and 15kV electron beam. Samples a), b) and c) are respectively pristine, CuO and NiO without YSZ. While samples d), e) and f) are respectively pristine, CuO and NiO with YSZ as a precursor.

Table 19: Estimate of grain sizes by image processing.

Sample	**Mean grain size [µm]**	**Min - max [µm]**
BSZCY	4	2 - 7
BS(YSZ)CY	7	3 - 11
BSZCYNi05	12	8 - 18
BS(YSZ)CYNi05	16	7 - 32
BSZCYCu05	9	3 - 16
BS(YSZ)CYCu05	12	6 -17

Samples were also polished at the cross section and thermally etched for 10 minutes at 1300°C, but because of varying success the results will not be discussed and are placed in appendix B. The takeaway is that BS(YSZ)CYNi05(O2)* have two times larger grain size than BSZCYNi1. The mean grain diameters were found to be approx. 4.6µm and 2.4µm by gaussian fitting grain size diameters extracted with image processing software (ImageJ) for BS(YSZ)CYNi05(O2)* and BSZCYNi1, respectively.

5.3.3 Grain distribution of crushed pellet

The sintered pellet BS(YSZ)CYCu05 was examined by SEM to determine the grain size distribution of the crushed pellet prior to TG measurement. It is evident from Figure 32 that the distribution of grains is not uniform. The grains are ranging from a couple micrometres to around 100µm in some instances. This is of interest as bigger particles use longer time to reach chemical equilibrium. This could be the reason for not equilibrated isotherms, especially at lower temperatures in the TG analysis

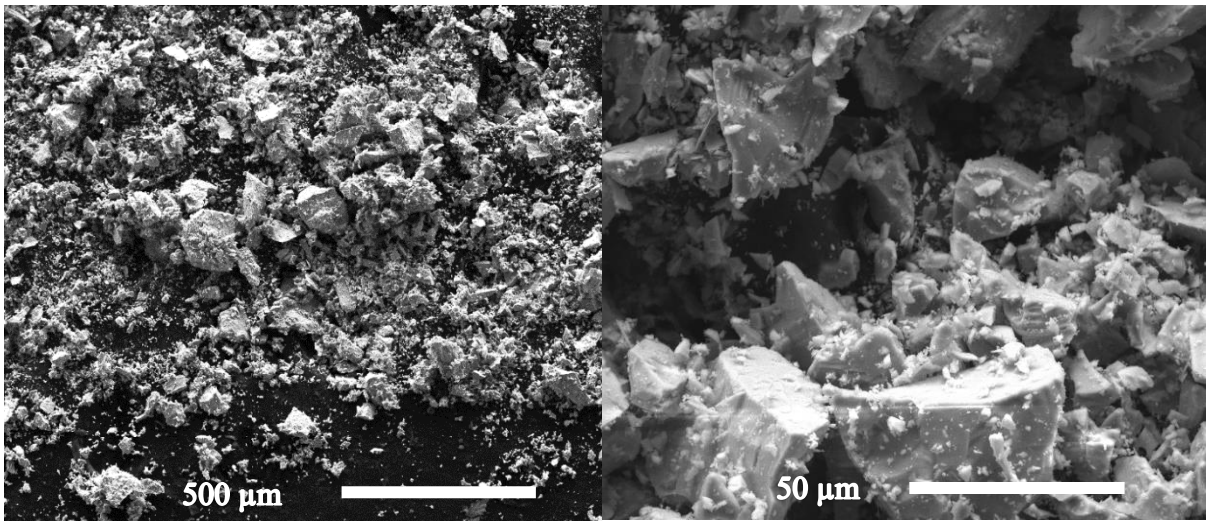

Figure 32: Grain size distribution of crushed BS(YSZ)CYCu05 pellet.

5.4 HT-XRD

The XRD patterns were obtained from low to high temperature for a BSZCY151020 composition without sintering aid and YSZ. The initial pattern at room temperature show peaks from all precursors, where barium carbonate and zirconia are associated with high intensity peaks as they have highest mole fraction in the composition. Ceria, yttria and strontium carbonate, show lower counts per reflection and are therefore less isolated and detectable. For the latter, peak positions were checked by performing a simple XRD scan with Cu*K*α radiation source for pure $SrCO_3$ and then fitted to the Mo*K*α spectrum, which showed the orthorhombic structure as expected.

The major changes in the precursor mix are mainly due to allotropic change of barium carbonate and the decomposition of carbonates. The transition from orthorhombic to trigonal (rhombohedral) and onward to cubic is observed respectively at approx. 800°C and 1020°C for barium carbonate. This fits well with the observations from Tong et al. [34] and Nie et al. [58]. The first allotropic change is also observed for strontium carbonate, however presumably due to overlapping peaks the expected trigonal phase is not observed. At 1130°C the cubic phase of barium carbonate disappears from the XRD pattern indicating that decomposition is well underway. Below 900°C there are no other significant changes. In Figure 33 the intensities from XRD patterns between 900-1200°C reveal the changes in the XRD pattern vs. temperature, here the background is removed meaning less intense peaks are not visible. The most significant peaks corresponding to the precursors and the cubic perovskite are marked in with coloured dashed lines.

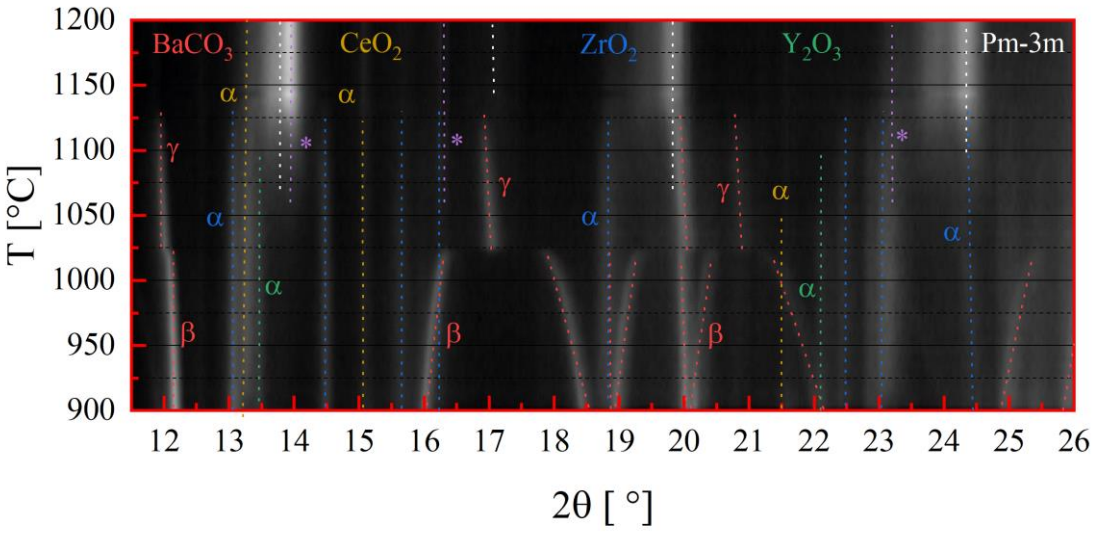

Figure 33: Layered (2D) intensity graph versus temperature with dashed lines to expose peaks and their relative phase. Barium carbonate in red, Ceria in gold, Zirconia in blue and Yttria in green. The purple lines and stars expose the tetragonal peaks that are barely visble.

The dashed lines in Figure 33 are drawn to expose the general transitions and reflection behaviour, the figure is in that regard a qualitative representation of what is observed from each pattern in the temperature range, supplementary figures can be found in appendix B (10.4). Zirconia and yttria peaks start to lose intensity around 1080°C, while yttria disappears around 1100°C, this indicates that yttria is stabilising zirconia into the tetragonal phase, which is briefly visible before the perovskite peaks out saturate them, especially at 14°. The PDF file (01-082-1244) was used to determine stabilized tetragonal zirconia, in the file the composition was $Zr_{0.84}Y_{0.16}O_{1.92}$. Zirconia disappears along with cubic barium carbonate phase at 1130°C, while ceria seems to remain in its precursor form to 1200°C (some peaks disappear, some remain).

The broad peaks emerging from 1100°C are related to the formation of the perovskite structure. However due to their nature, several cubic phases can be expected. $SrZrO_3$ (Pm-3m) is probably one of them as it was observed as a secondary phase in BSZCY1400, BSZCY and BS(YSZ)CY. Other peaks can be as mentioned tetragonal variants, such as $Zr_{0.84}Y_{0.16}O_{1.92}$ or possibly $Sr_3Zr_2O_7$.

5.5 Hydration thermodynamics and concentrations

Hydration thermodynamics, proton and oxygen vacancy concentration obtained from TG measurements for selected samples are presented here. The samples that also are characterised by EIS will be in focus, those are BSZCYNi1, BSZCYCu1 and BS(YSZ)CYCu05. As the

approach for each sample is similar all thermodynamic results are summarized in appendix B (10.5).

The mol hydroxide ions per mol of BSZCY is directly proportional to the mass change obtained from TG measurement. The relative proton concentration for BSZCYNi1, BSZCYCu1, and BS(YSZ)Cu05 are presented in Figure 34, Figure 35, and Figure 36, respectively.

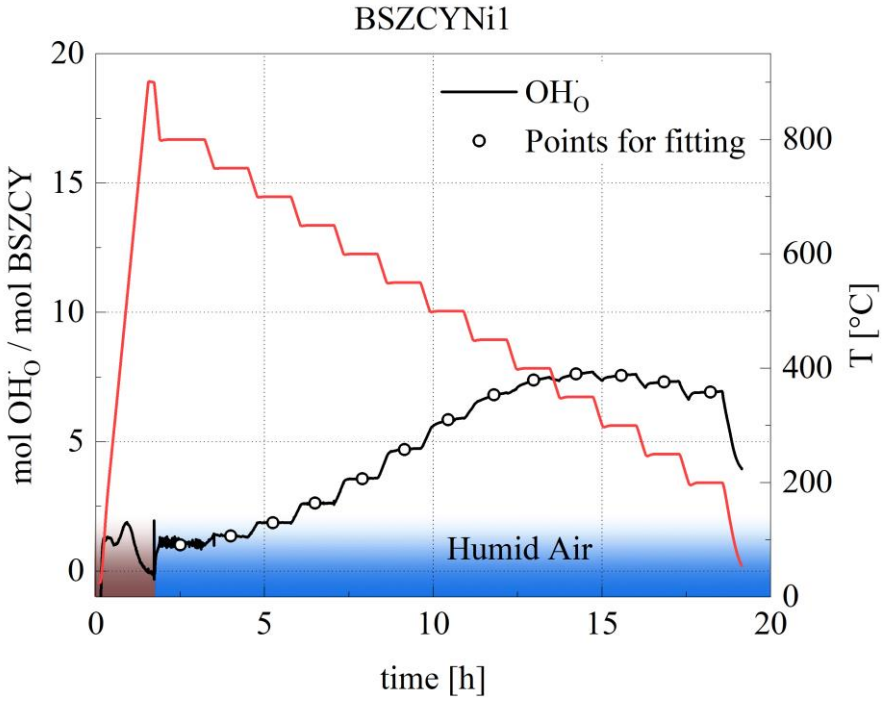

Figure 34: Mass gain results from thermogravimetric measurement of BSZCYNi1 converted to relative water uptake from dry (brown) conditions to humid (blue) conditions.

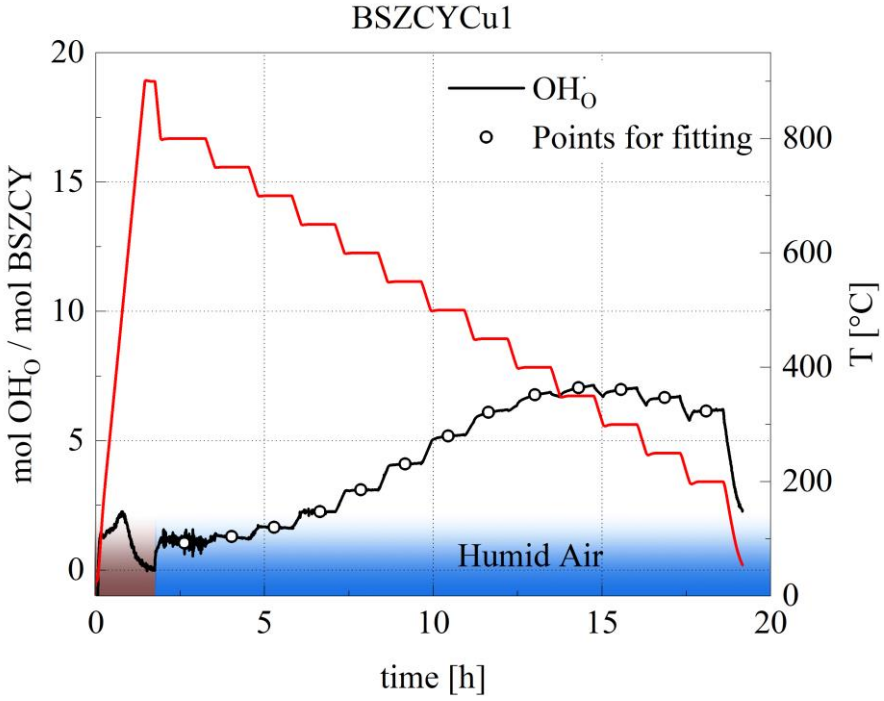

Figure 35: Mass gain results from thermogravimetric measurement of BSZCYCu1 converted to relative water uptake from dry (brown) conditions to humid (blue) conditions.

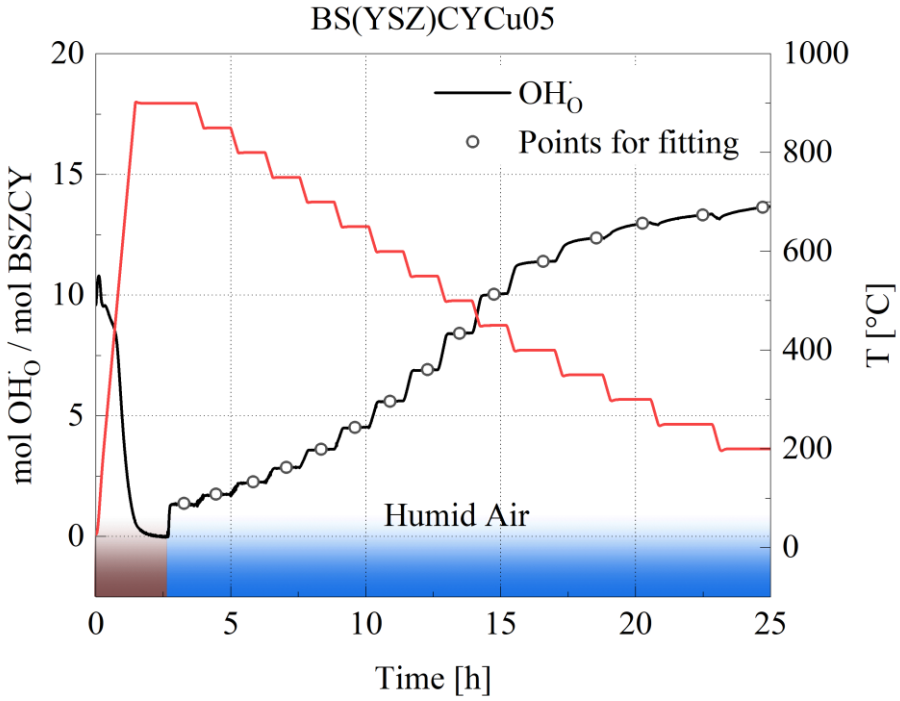

Figure 36: Mass gain results from thermogravimetric measurement of BS(YSZ)CYCu05 converted to relative water uptake from dry (brown) conditions to humid (blue) conditions.

In the results two distinct features are visible at temperatures below 400°C. That is the slight decrease in proton concentration closer to 200°C for BSZCYNi1 and BSZCYCu1, this might be due to buoyancy effects. For BS(YSZ)CYCu05 a steady increase in proton concentration is visible at the same temperature, this is probably due to the bigger particles taking longer to equilibrate . However, the curves are seen converging at lower temperature, which is due to the absorption limit of protons in the stated partial pressure of water.

Linear regression according to van't Hoff expression (2.305) is presented in Figure 37 for the three samples, where the natural logarithm of K_{hydr} yields the enthalpy (slope) and entropy (intercept) for the equilibrium coefficient.

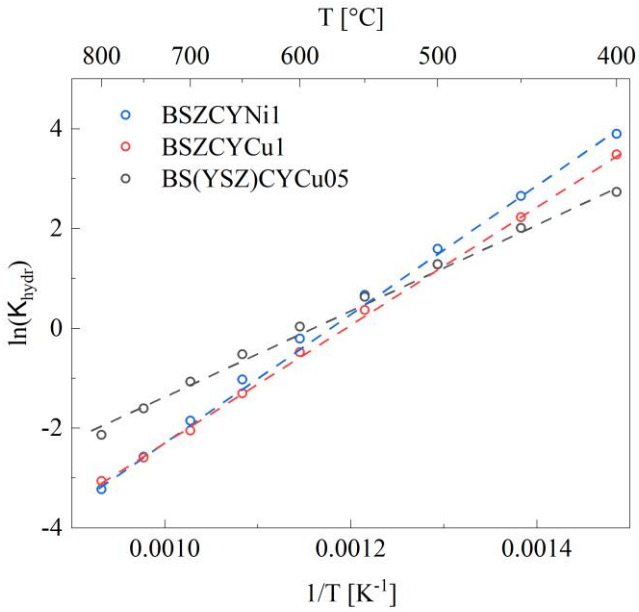

Figure 37: Van't Hoff plot with linear regression to extract enthalpy and entropy of hydration.

The obtained values for enthalpy and entropy of hydration, and effective acceptor doping (max hydration) are presented in Table 20.

Table 20: Enthalpy, entropy and effective acceptor doping from van't Hoff linear regression.

Sample	$\Delta H°_{hydr}$ $[kJ\ mol^{-1}]$	$\Delta S°_{hydr}$ $[J\ K^{-1}mol^{-1}]$	S%	r^2
BSZCYNi1	-107	-125	8	0.9980

BSZCYCu1	-100	-119	7	0.9988
BS(YSZ)CYCu05	-73	-84	14	0.9952

The same values were also obtained by fitting the proton concentration expression (2.310) directly, with the equilibrium equation as a secondary function in *Table Curve 2D*. The correlating oxygen vacancy concentration (red) and site fraction of oxygen (green) are plotted alongside the fitted proton concentrations (blue) with standard deviations indicated by dashed lines. These are presented for BSZCYNi1, BSZCYCu1, and BS(YSZ)CYCu05 in Figure 38, Figure 39, and Figure 40, respectively.

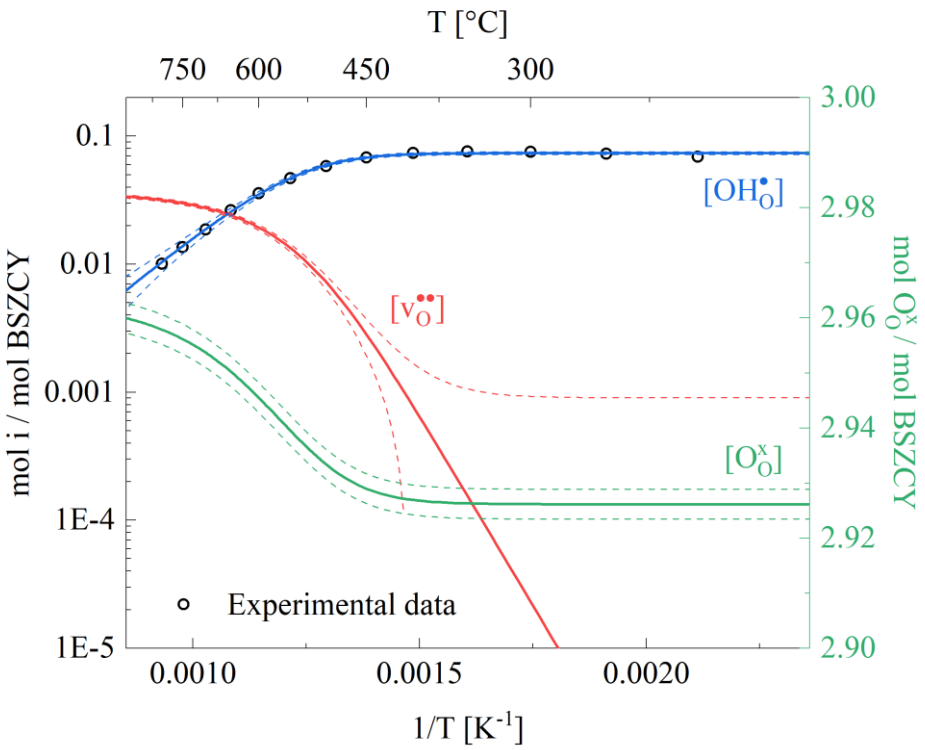

Figure 38: Fitted relative concentrations of protons, vacancies, and oxygen (w/ S.D.) for BSZCYNi1 based on the isothermal points obtained in TG.

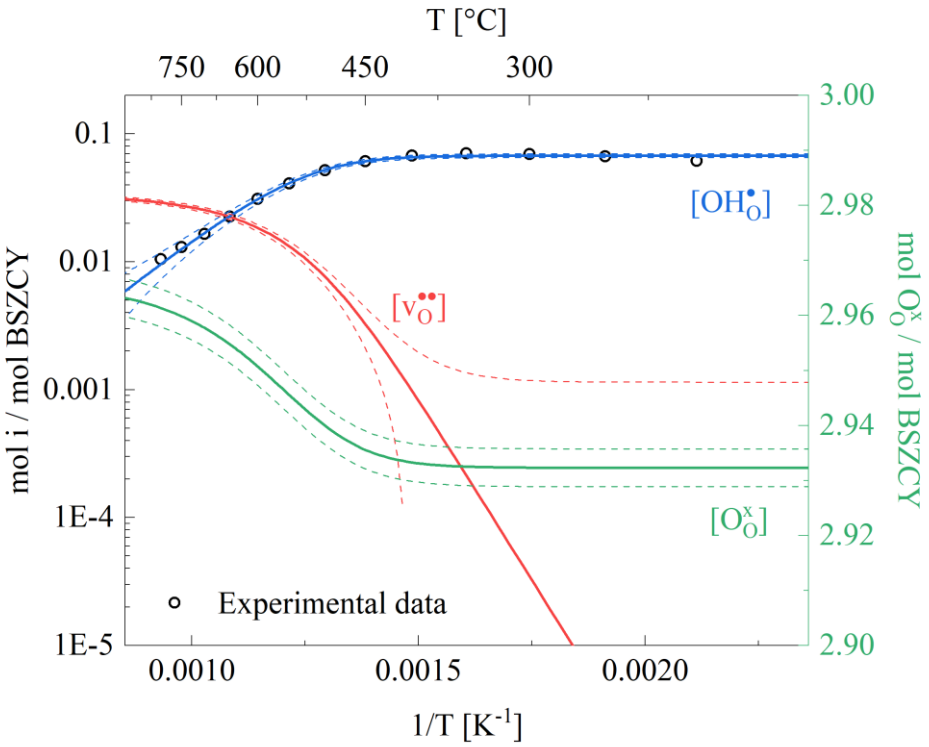

Figure 39: Fitted relative concentrations of protons, vacancies, and oxygen (w/ S.D.) for BSZCYCu1 based on the isothermal points obtained in TG.

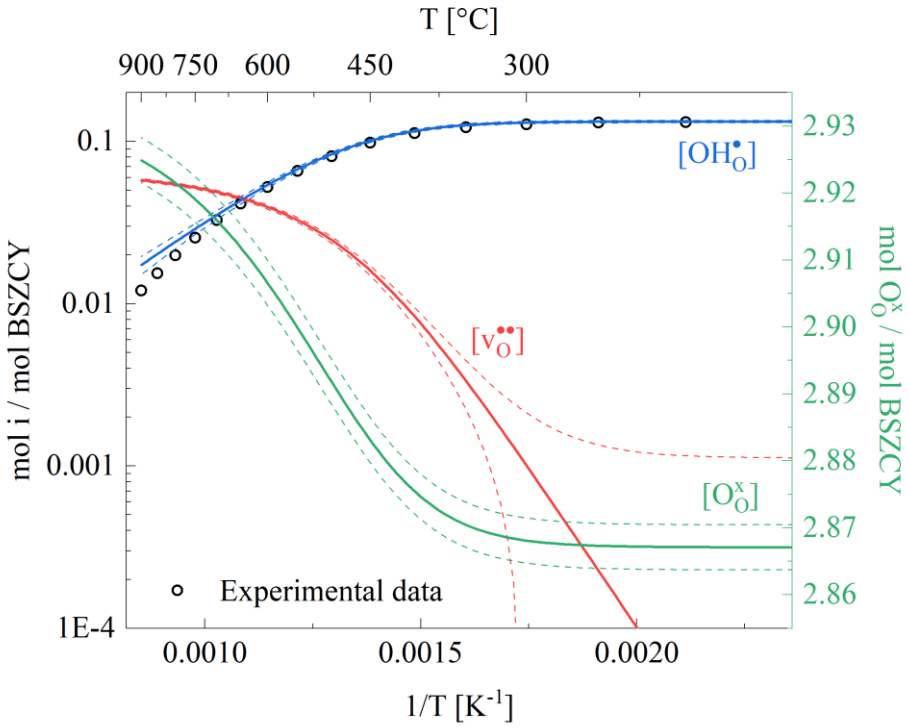

Figure 40: Fitted relative concentrations of protons, vacancies, and oxygen (w/ S.D.) for BS(YSZ)CYCu05 based on the isothermal points obtained in TG.

The obtained values for hydration enthalpy and entropy, and effective acceptor doping are presented Table 21.

Table 21: Enthalpy and entropy of hydration, and effective acceptor doping obtained through fitting of proton concentrations.

Sample	$\Delta H°_{hydr}$ $[kJ\ mol^{-1}]$	$\Delta S°_{hydr}$ $[J\ K^{-1}mol^{-1}]$	S%	r^2
BSZCYNi1	-114	-132	7	0.9964
BSZCYCu1	-109	-128	7	0.9931
BS(YSZ)CYCu05	-76	-87	13	0.9979

5.5.1 Effective acceptor doping

When the thermogravimetric results showed a converging behaviour at low temperatures, the effective acceptor dopant was extracted as the maximum proton concentration:

$$\max[OH_O^{\cdot}] = \left[Y'_{Zr,eff}\right] \quad (5.500)$$

These values were again evaluated when the thermodynamic parameters were extracted by van't Hoff linear regression. The following results are presented with respect to the van't Hoff extraction, but results from multifunction fitting for selected samples are also presented in appendix B (Table S 4), where the effective acceptor doping is a free parameter. The mean deviation for the effective acceptor concentration between the two methods was found to be approx. ± 0.5 % (when comparing the two in percentage).

The effective acceptor concentration for all samples in Figure 41 are around half of that expected with 20mol% yttrium. Additionally, some trends are distinguishable. The nickel containing samples show a decreased effective acceptor doping relative to the pristine samples, which could be due to the association of nickel with barium vacancies [33], nickel at B-site or as a interstitial associated with yttrium, all with the potential of annihilating oxygen vacancies.

The copper containing samples show an increase in effective acceptor concentration from 1400°C to 1600°C (Figure 41), and exceed that of the pristine sample at 1600°C. According to the SEM analysis, copper might form segregation along the grain boundaries which could indicate that copper dissolves into the structure to a lesser degree then nickel, which is also observed from Han et al. [6]. The increase in effective acceptor concentrations can be indicative of lower dissolution of copper coupled with the increased densification and reaction rates during sintering.

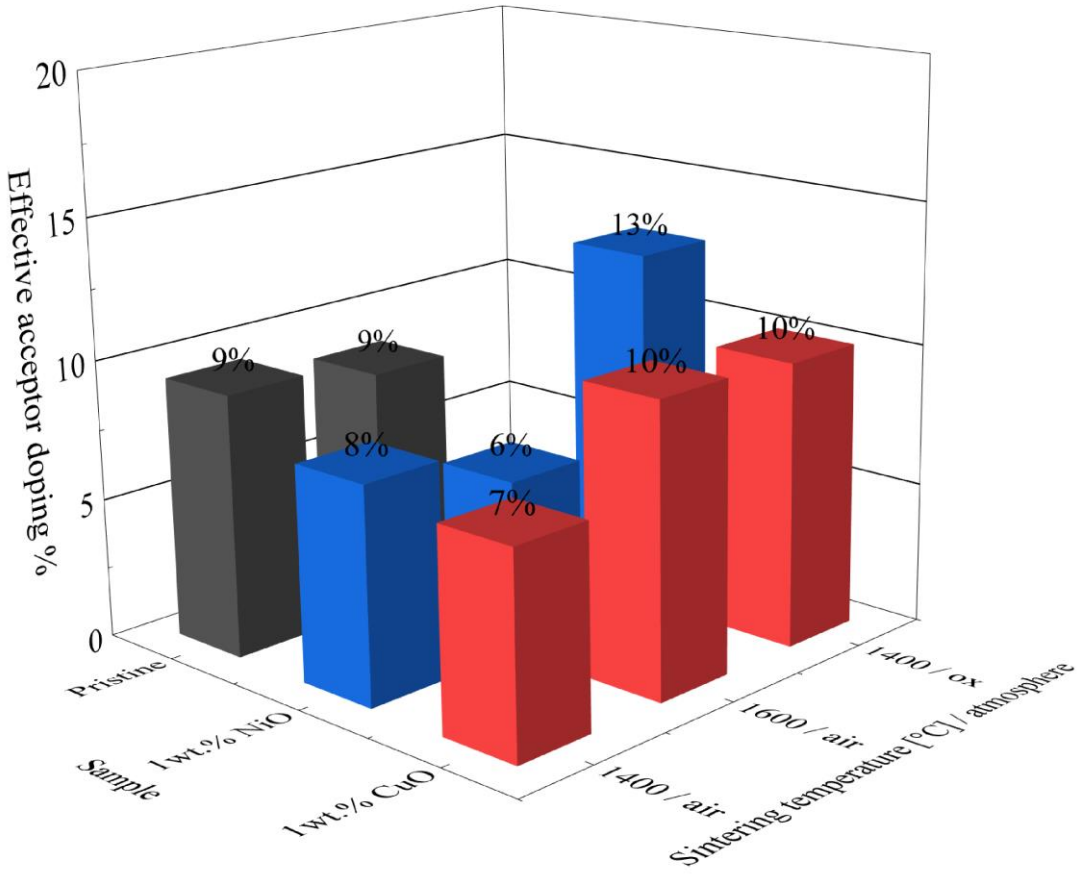

Figure 41: Effective acceptor dopant matrix of samples with and without sintering additives sintered for 12 hours in air at 1400°C and 1600°C, and samples sintered for 12 hours in oxygen at 1400°C.

A matrix of effective acceptor concentration is constructed for the samples with 0.5wt.% sintering aid sintered at similar temperatures in air with and without YSZ as a precursor in Figure 42. The pristine samples with and without YSZ show an increase of around 4% compared to the pristine samples in Figure 41. This increase might be due to correct stoichiometry of sacrificial powders, which would decrease the yttrium concentration gradient across the interface between pellet and powder, decreasing diffusion.

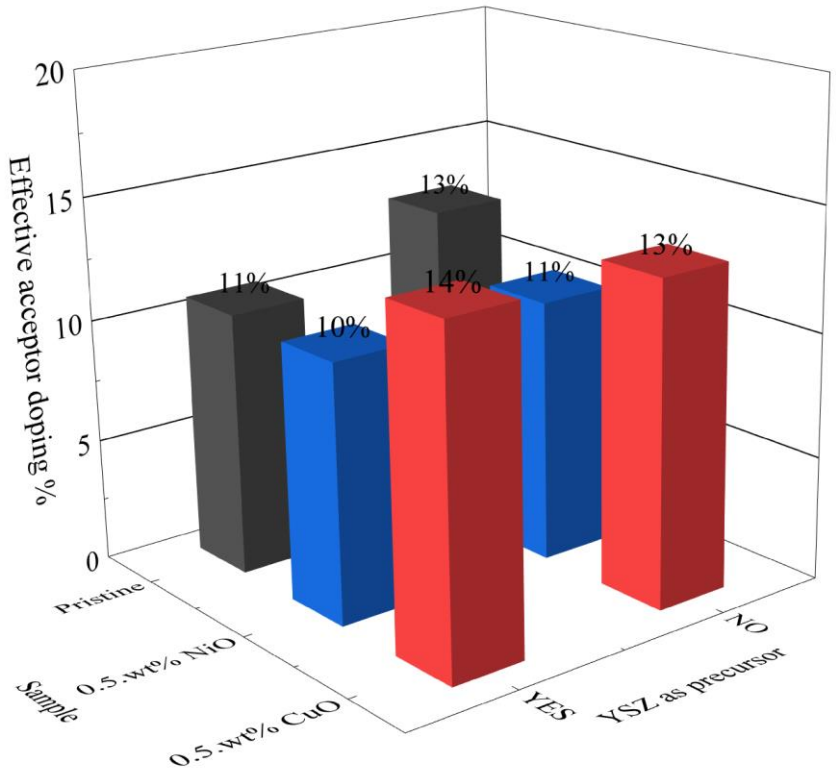

Figure 42: Effective acceptor dopant matrix of samples with and without YSZ, where pristine samples are sintered at 24 hours and the rest for 12 hours, all at 1600°C.

The degree of hydration compared to the nominal stoichiometry (20mol% yttrium) in percentage for all samples is between 30-70%, which is relatively low compared BZY20 and BZY10 which show respectively 90% and 100% hydration after sintering at 1700°C [35].

5.6 Electrochemical impedance measurements

EIS measurements were carried out under equilibrium conditions in humid argon and dry air in the temperature range 700-100°C and 1000-500°C, respectively, for the BSZCYNi1 and BSZCYCu1 samples. They were also investigated under different partial pressures of oxygen, from reducing (wet harmix) to oxidizing (pure oxygen) atmospheres at 400, 600, 800 and 1000°C. The BS(YSZ)CYCu05 sample was measured in humid argon from 800 to 30°C by using a mantel heater at temperatures below 250°C.

In this chapter results for electrochemical transport properties, space charge layers and dielectric relaxations are presented with basis in the data obtained by EIS measurements.

5.6.1 Impedance

Selected Nyquist plots for the three samples, BSZCYNi1, BSZCYCu1 and BS(YSZ)CYCu05 in humid argon are presented in Figure 43, Figure 44, and Figure 45, respectively.

BSZCYNi1, BSZCYCu1 and BS(YSZ)CYCu05 showed similar characteristics in humid argon. At high temperatures, an ohmic contribution followed by a semicircle tangled with the electrode response yielded, respectively, the bulk resistance and GB resistance. At intermediate temperatures the same applied but with no entanglement between GB and electrode, allowing for the extraction of GB capacitance. At low temperatures ($< 350°C$) the bulk semicircle appeared, and the bulk capacitance was also extracted.

The only visible deviation is seen for BSZCYNi1 which seems to exhibit another faradic element at temperatures below 300°C, which is seen in Figure 43b at 10^4 Hz at 200°C. The additional element at high frequency was deconvoluted as a bulk contribution.

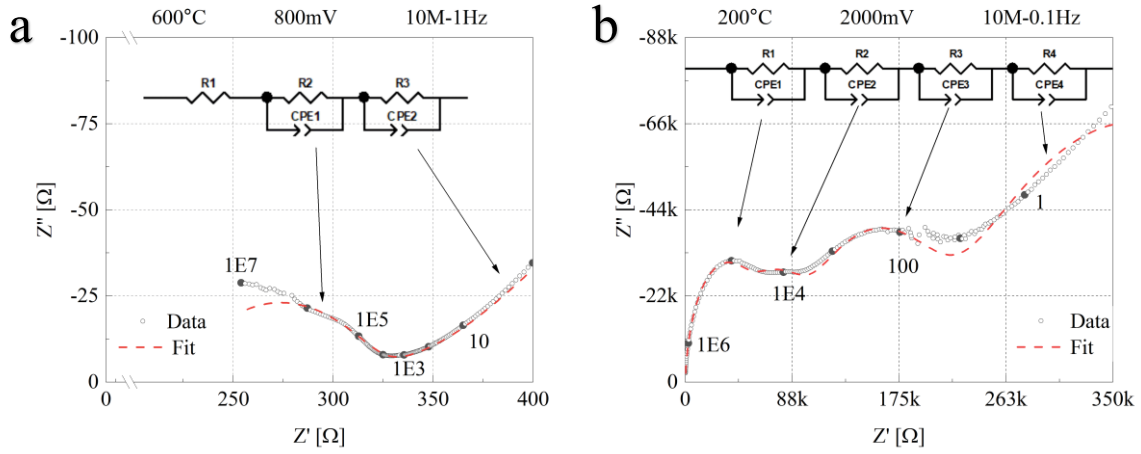

Figure 43: Nyquist plots for representative impedance sweeps at high- (a - 600°C) and low-temperature (b - 200°C) in humid argon for BSZCYNi1.

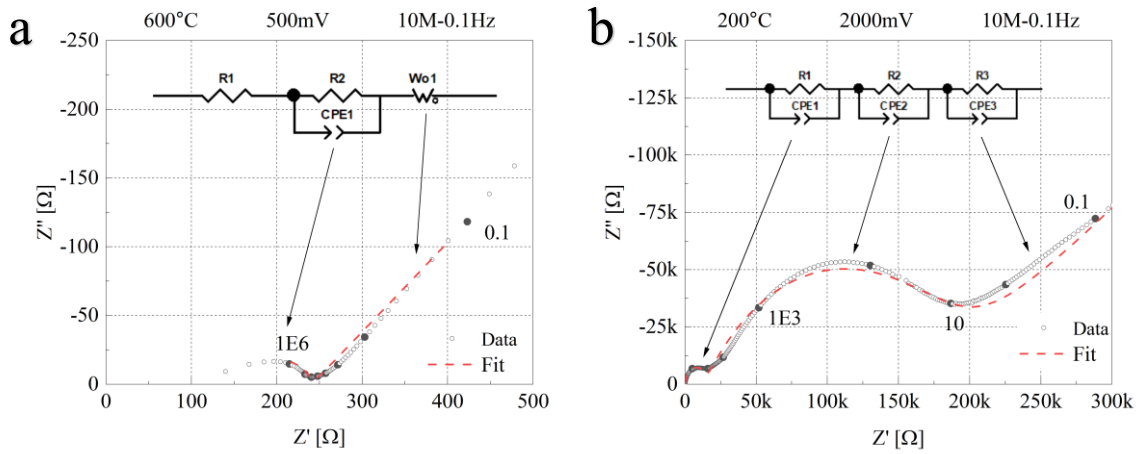

Figure 44: Nyquist plots for representative impedance sweeps at high- (a - 600°C) and low-temperature (b - 200°C) in humid argon for BSZCYCu1.

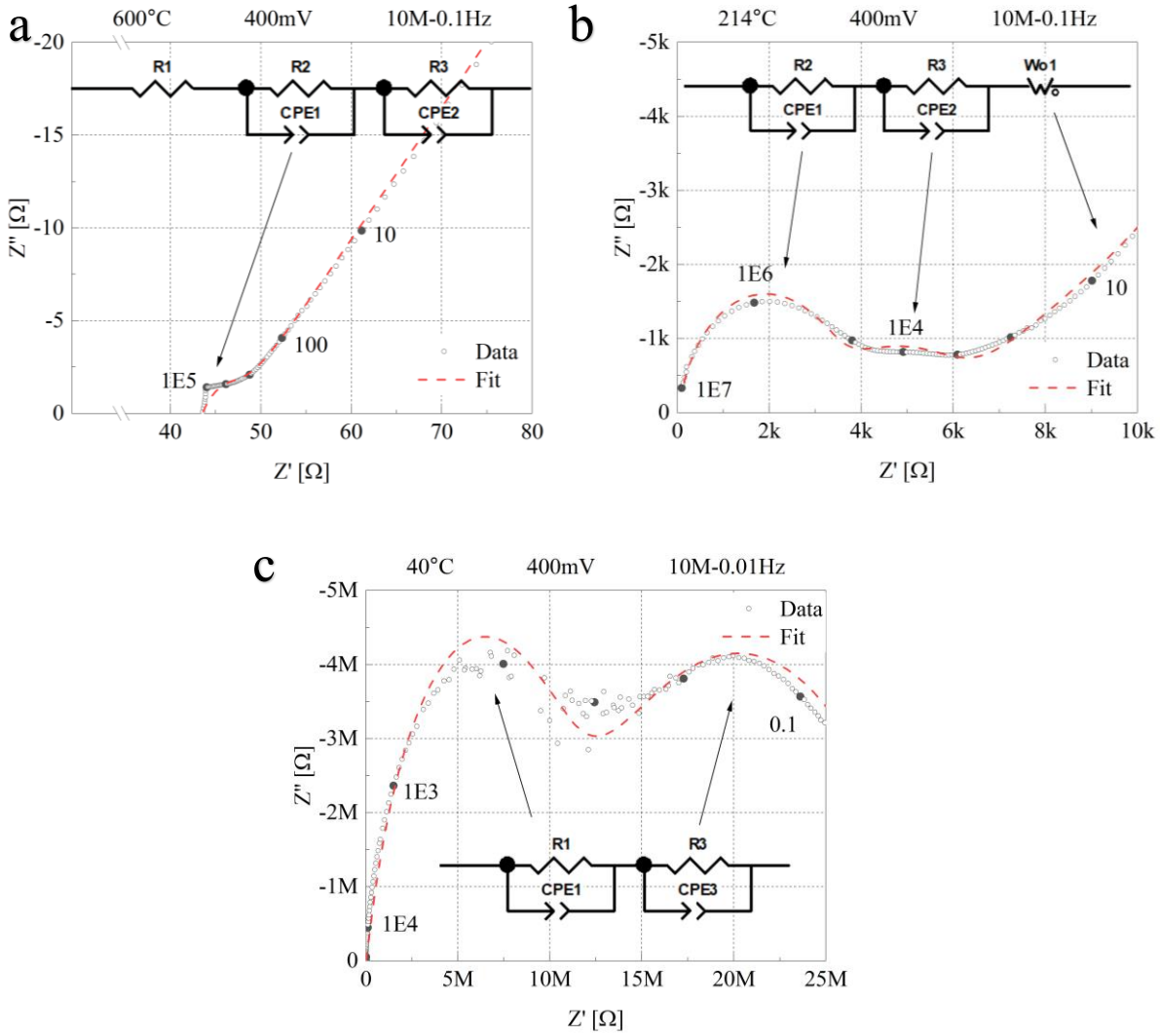

Figure 45: Nyquist plots for representative impedance sweeps at high (a - 600°C), low (b - 214°C) and very low (c - 40°C) temperatures for BS(YSZ)CYCu05 in humid argon.

Impedance spectra for dry air measurements are not presented as they consisted of the same characteristic seen in humid argon at high temperature. Generally, these contained an ohmic contribution from bulk (R), a mid- and high- frequency response for grain boundary and electrode (RCPE), respectively.

5.6.2 Capacitance

The parasitic capacitance of the ProboStat™ was measured with a dense alumina pellet between the current collectors at room temperature. The measured capacitance was ~7 *pF* which is way below that expected from the dielectric of alumina, which means that the alumina pellet acted as an insulator.

The mean value of the apparent bulk and GB capacitances specific to the area and length of the sample are presented in Table 22.

Table 22: Mean value for bulk and GB capacitances obtained from EIS spectra at low temperature.

Sample	$\boldsymbol{C_{bulk}}$ $\boldsymbol{[Fcm^{-1}] \times 10^{-11}}$	$\boldsymbol{C_{G.B.}}$ $\boldsymbol{[Fcm^{-1}] \times 10^{-10}}$
BSZCYNi1 (350-100°C)	2.07	2.24
BSZCYCu1 (300-100°C)	3.17	5.89
BS(YSZ)CYCu05 (214-30°C)	4.89	9.29

5.6.3 Conductivity

All conductivities in humid argon are presented together with data from Dayaghi et al. [4] on the same composition to outline difference between the two studies, and possibly the effects of sintering aids. The reference electrolyte is pristine BSZCY151020 sintered for 48hours at 1650°C and measured in humid 5% H_2 – Argon mixture ($p_{H_2O} = 0.026atm$).

Activation energies extracted in different temperature intervals are summarised in appendix B (10.6).

The total conductivity as a function of temperature of BSZCYNi1 (blue) and BSZCYCu1 (red) in humid argon (a) and dry air (b) are presented in Figure 46. The conductivities in humid argon show two domains, at low temperature, the conductivity is linear with inverse temperature ($\Delta H_a \approx \Delta H_{mob}$), while at high temperature dehydration is observed by the shift in slope ($\Delta H_a \approx \Delta H_{mob} + \Delta H_f$). The dry air measurements are within one linear domain, which suggest that the conductivity is dominated by the increase in hole and oxygen vacancy mobility. At 500°C, $\sigma_{humid\ argon} > \sigma_{dry\ air}$ which is indicative to the absence of protons in the dry air and the lowered mobility of oxygen vacancies ($\Delta H_{OH_O^{\cdot},mob} < \Delta H_{v_O^{\cdot\cdot},mob}$).

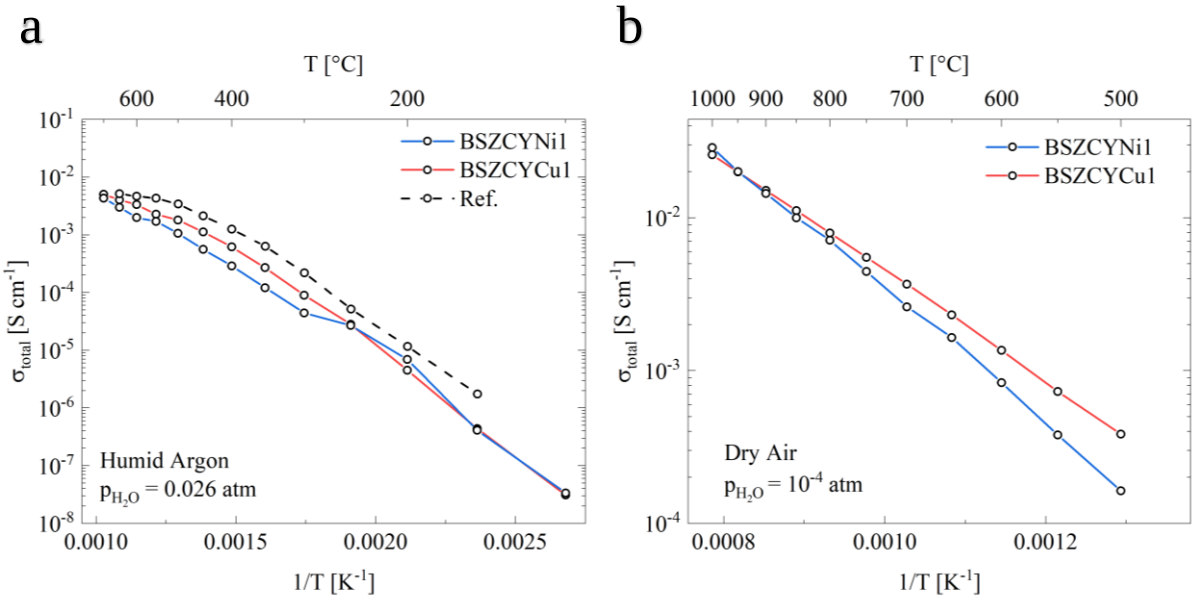

Figure 46: Total Conductivity in humid argon (a) and dry air (b).

The GB conductivity for BSZCYNi1 (blue) and BSZCYCu1 (red) in humid argon (a) and dry air (b) are presented in Figure 47. For both samples C_{bulk} and C_{gb} were extracted from the EIS spectra below 350°C, which was then used according to BLM (2.226) to calculate the spesific grain boundary conductivity. Furthermore the mean value of $\frac{C_{bullk}}{C_{gb}}$ was used to extrapolate the spesific grain boundary conductivity above 350°C, the result are shown in Figure 47a as BLM. The spesific grain boundary conductivity is approx. one order of magnitude lower than the unspesific for both BSZCYNi1 and BSZCYCu1. The GB conductivity in dry air (Figure 47b)

is two times higher for BSZCYCu1 compared to BSZCYNi1 at 500°C and 20 times higher at 1000°C.

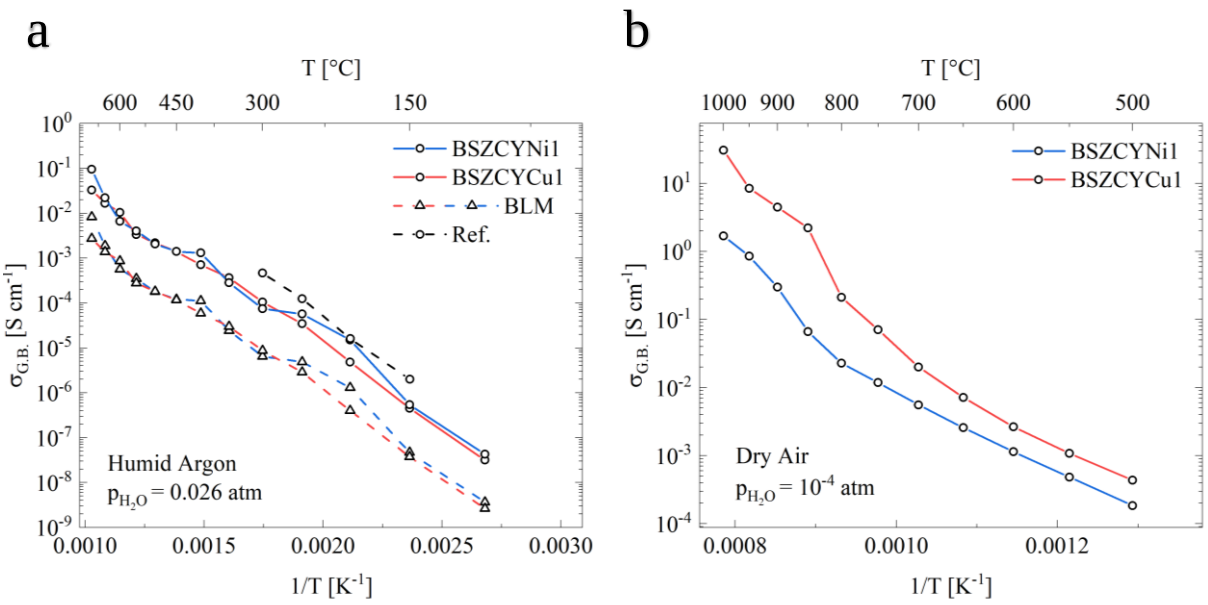

Figure 47: Grain boundary conductivity of BSZCYNi1 (blue) and BSZCYCu1 (red) in humid argon (a) and dry air (b), with reference.

The bulk conductivity for BSZCYNi1 (blue) and BSZCYCu1 (red) in humid argon (a) and dry air (b) are presented in Figure 48. The bulk conductivity of BSZCYCu1 is approx. 5 times higher compared to BSZCYNi1 in humid argon, while in dry air the bulk conductivity is roughly the same.

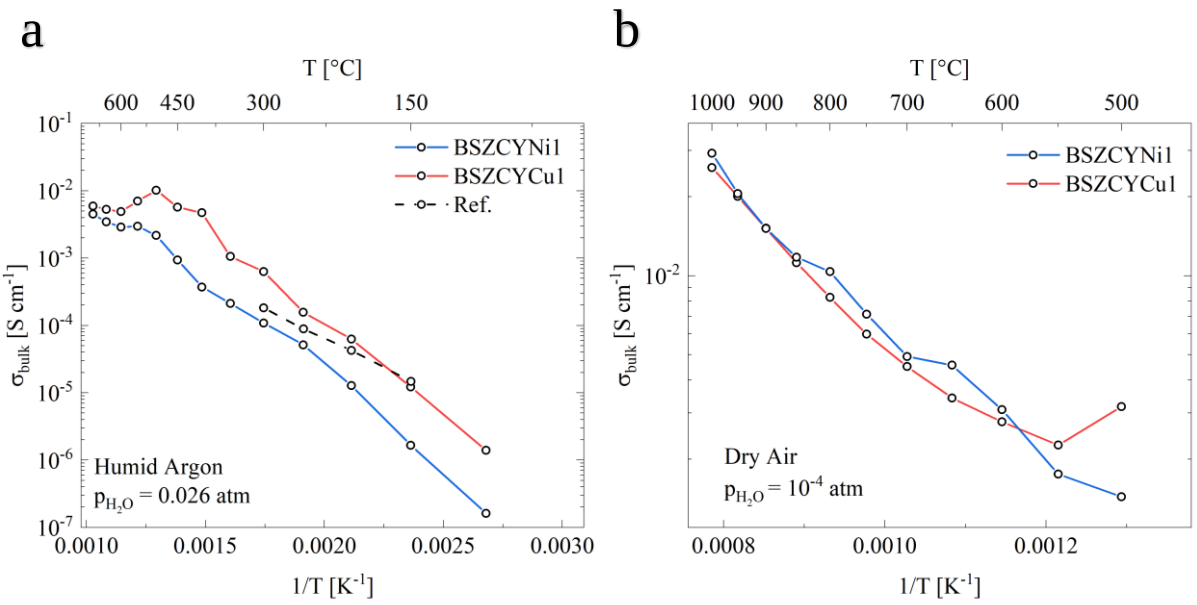

Figure 48: Bulk conductivity of BSZCYNi1 (blue) and BSZCYCu1 (red) in humid argon (a) and dry air (b), with reference.

The total, bulk, GB, and specific GB conductivity in humid argon for BS(YSZ)CYCu05 are presented in Figure 49. Two dominating domains are observed, namely where proton concentration is constant and where dehydration occurs. Closer to room temperature a slight increase in conductivity is observed possibly because of surface transport of protons.

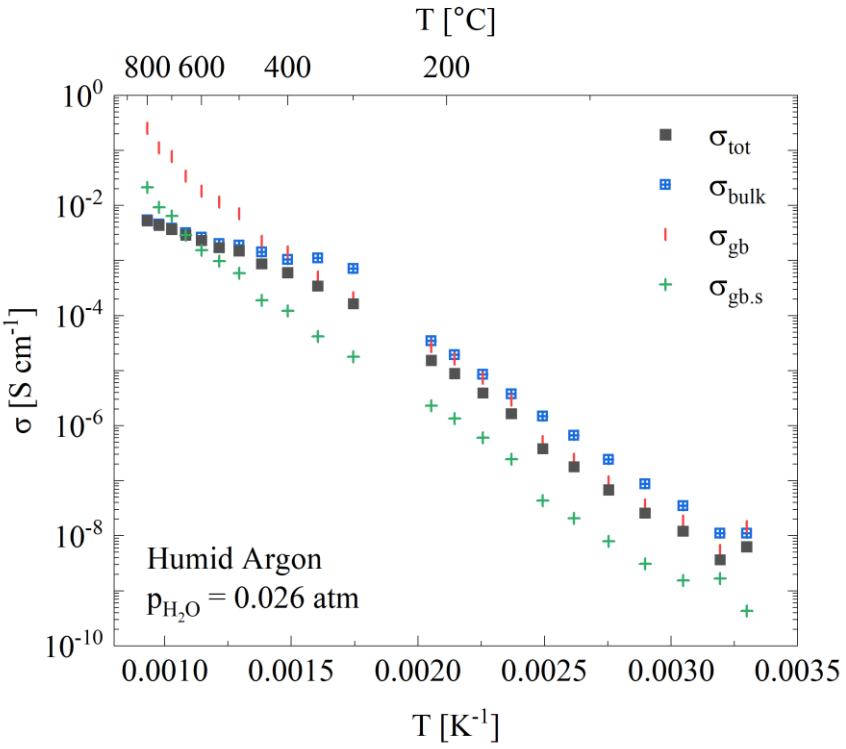

Figure 49: Total, bulk, GB, and specific GB conductivity for BS(YSZ)CYCu05 in humid argon.

5.6.4 Oxygen dependencies

The conductivity as function of partial pressure of oxygen was measured by EIS at 400, 600, 800 and 1000°C. A representative set of EIS spectra under varying pO_2 at 1000°C is presented in Figure 50 obtained from measurements on BSZCYCu1. At high pO_2 (b) the low frequency capacitance is barely visible as hole conduction is dominating and leaking through the sample. At low pO_2 (a) the intersection point of the X-axis remains roughly constant, indicating no change in bulk resistance. The mid to low frequency response of the grain boundary and electrode, respectively, show a varying response with partial pressure of oxygen.

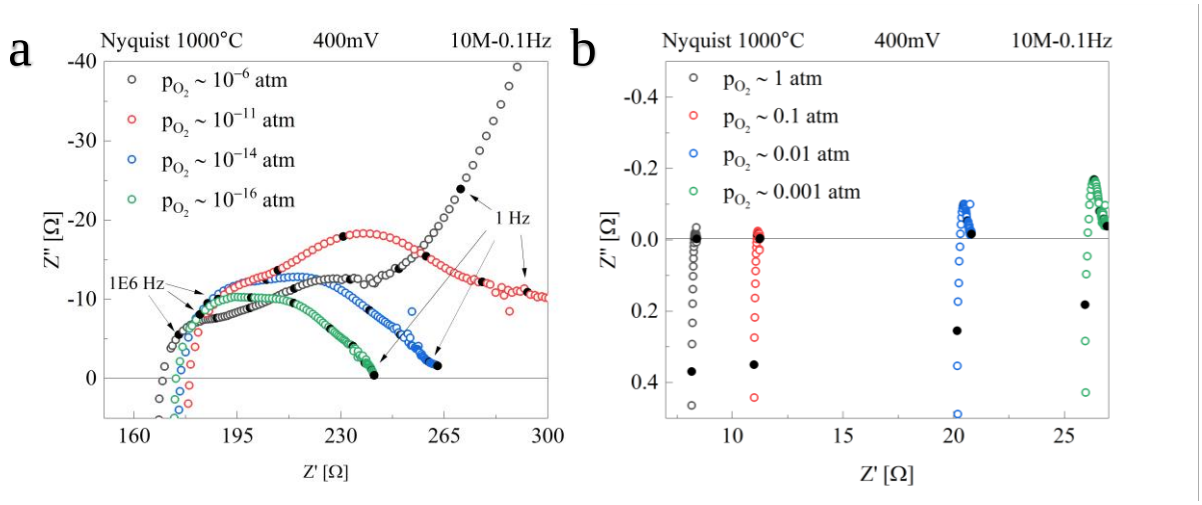

Figure 50: EIS spectra under varying pO_2 at 1000°C for BSZCYC1.

The results for BSZCYCu1 and BSZCYNi1 are presented as conductivity versus pO_2 in Figure 51 and Figure 52, respectively. Each graph contains the experimental values obtained in atmospheres ranging from pure oxygen to harmix.

The total conductivity for each isothermal in Figure 51 and Figure 52 was fitted as $\log(\sigma)$ versus $\log(p_{O_2})$ in accordance with the approach explained in 4.4.3. In this instance a ionic contribution was used instead of protons and oxygen vacancies separately. Subsequently, the pre-exponential and enthalpy of mobility for ions are defined as u^0_{ionic} and $\Delta H_{ionic,mob}$ and will fit to the region independent of partial pressure of oxygen. The fittings were done in TableCurve 2D and the result is presented as total and hole conductivity as dashed lines in the plots. The parameters for holes obtained from the fittings for both BSZCYNi1 and BSZCYCu1 are presented in Table 23.

Furthermore, it's evident that total conductivity conforms to a ¼ $\log(p_{O_2})$ dependency at 1000°C for both samples. There is a slight difference at 800°C, where BSZCYNi1 follows ¼ dependency to a higher degree then BSZCYCu1.

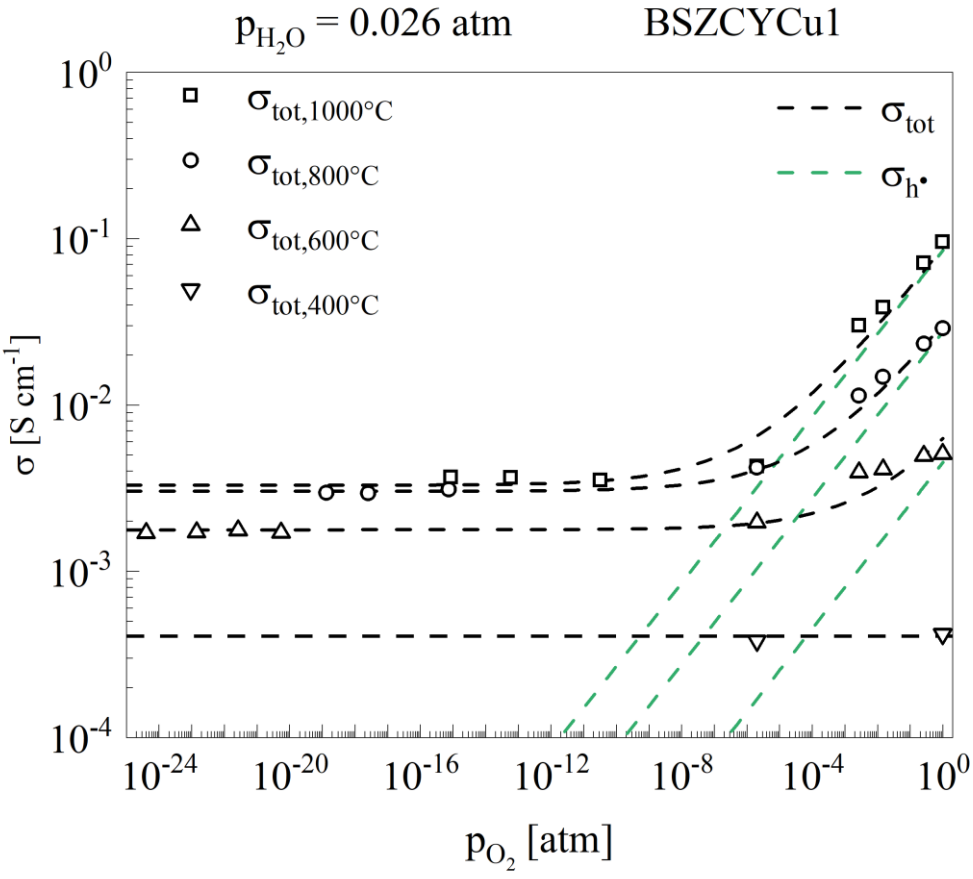

Figure 51: Conductivity for BSZCYCu1 in humid atmosphere as a function of partial pressure of oxygen.

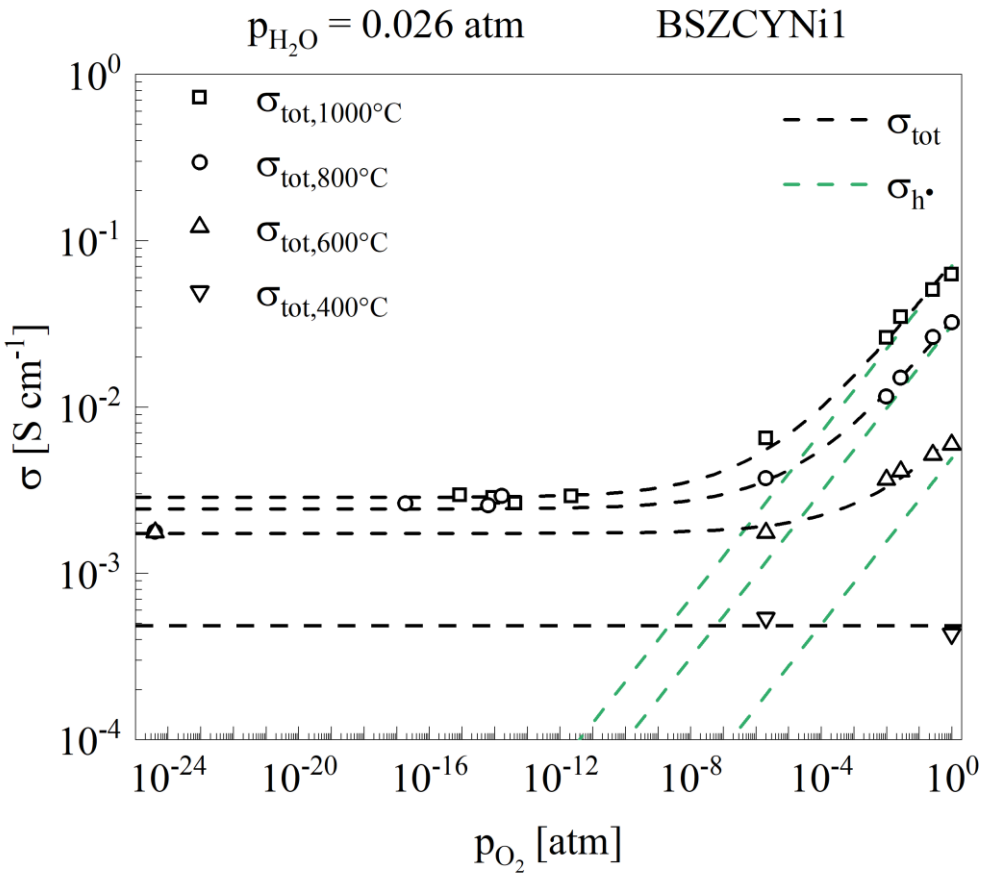

Figure 52: Conductivity for BSZCY151020 w/ 1wt.% NiO in humid atmosphere with changing partial pressure of oxygen for selected isotherms.

Table 23: Values for pre-exponential and activation energy for the two samples of BSZCY151020 containing 1wt.% NiO and CuO obtained by multifunction fitting.

Sample	BSZCYNi1			BSZCYCu1		
T [°C]	σ_p^0 $\left[Kcm^2\,V^{-1}s^{-1}\,atm^{-\frac{1}{4}}\right]$	$\Delta H'_{a,ox}$ $\left[\frac{kJ}{mol}\right]$	R^2	σ_p^0 $\left[Kcm^2\,V^{-1}s^{-1}\,atm^{-\frac{1}{4}}\right]$	$\Delta H'_{a,ox}$ $\left[\frac{kJ}{mol}\right]$	R^2
600	412	70.4	0.969	407	70.8	0.944
800	407	70.3	0.984	402	70.9	0.998
1000	349	72.8	0.990	338	69.1	0.996

5.6.5 Model parameters and partial conductivities

Conductivity models were obtained by multifunction fitting parameters for mobility with conductivity data for each charge carrier, where proton and oxygen concentrations were obtained from hydration measurements with thermogravimetry. The fitting was executed with conductivity data in varying conditions, namely humid argon, humid oxygen, and dry air versus inverse temperature. The obtained parameters for BSZCYNi1 and BSZCYCu1 are presented in Table 24, where the R-square error is from the final fit in humid argon. The fitting curve (total conductivity) and the resulting partial conductivities for BSZCYNi1 and BSZCYCu1 are presented in 5.6.5.1 and 5.6.5.2, respectively.

Table 24: Fitting results for BSZCYNi1 and BSZCYCu1 from all conditions. The R square error value is obtained from the final fit in humid argon. *Star indicates fixed parameters.

Parameters	**Units**	**BSZCYNi1** $R^2 = 0.9945$	**BSZCYCu1** $R^2 = 0.9972$
$S\%^*$	$unitless$	7	7
ΔS^*_{hydr}	$[kJ\ mol^{-1}]$	-132	-128
ΔH^*_{hydr}	$[kJ\ mol^{-1}]$	-114	-109
$u^0_{OH_O^\cdot}$	$[cm^2\ K\ V^{-1}s^{-1}]$	181	1072
$\Delta H_{OH_O^\cdot,mob}$	$[kJ\ mol^{-1}]$	65	72
σ_p^0	$\left[cm^2\ K\ V^{-1}s^{-1}\ atm^{-\frac{1}{4}}\right]$	850	2149
$\Delta H_{p,a}$	$[kJ\ mol^{-1}]$	86	93

$u^{0}_{v_O^{\cdot\cdot}}$	$[cm^2\ K\ V^{-1}s^{-1}]$	91	241
$\Delta H_{v_O^{\cdot\cdot},mob}$	$[kJ\ mol^{-1}]$	89	92

5.6.5.1 BSZCY151020 – 1wt.%NiO - 1400°C -12h (BSZCYNi1)

The modelled partial conductivities with transport numbers for BSZCYNi1 are presented in humid argon, dry air and humid oxygen in Figure 53, Figure 54, and Figure 55, respectively.

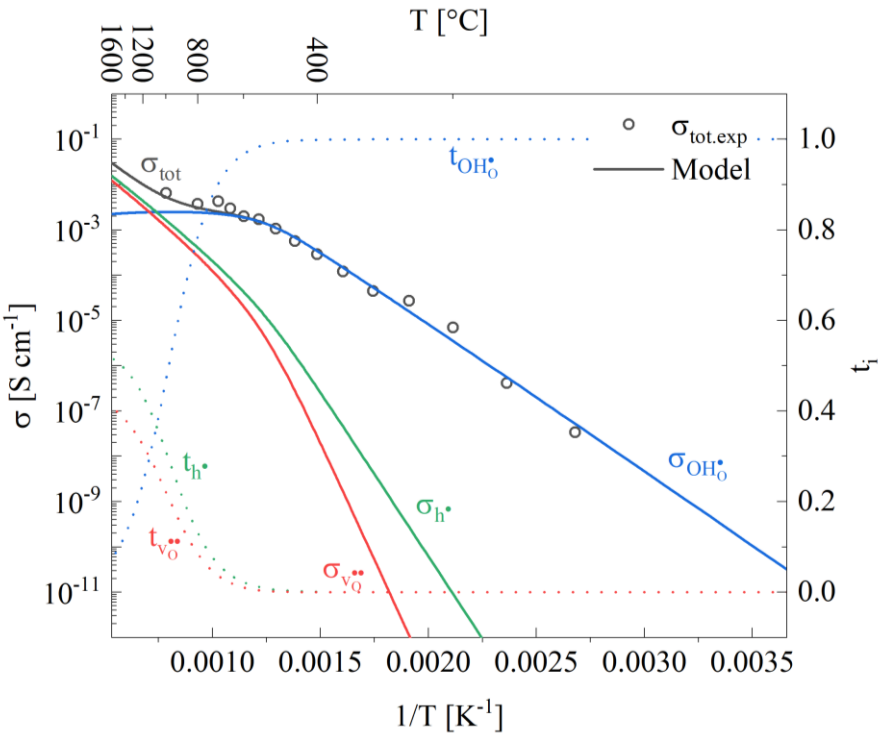

Figure 53: Partial conductivity for protons, oxide ions and holes in humid argon ($p_{H_2O} = 0.026\ atm$ & $p_{O_2} = 2 * 10^{-6}\ atm$) with transport numbers for BSZCYNi1

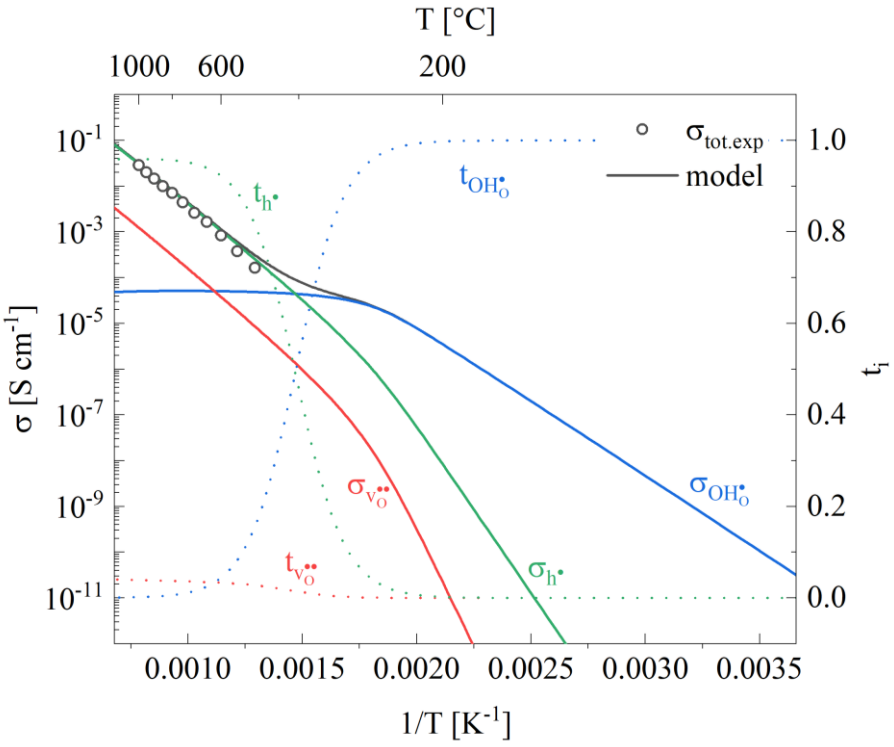

Figure 54: Partial conductivity for protons, oxide ions and holes in dry air ($p_{H_2O} = 10^{-5}\ atm\ \&\ p_{O_2} = 0.21\ atm$) with transport numbers for BSZCYNi1

The discrepancies of the model are most visible in humid oxygen in Figure 55, where hole and oxygen vacancy conductivity slightly deviate from the measured data.

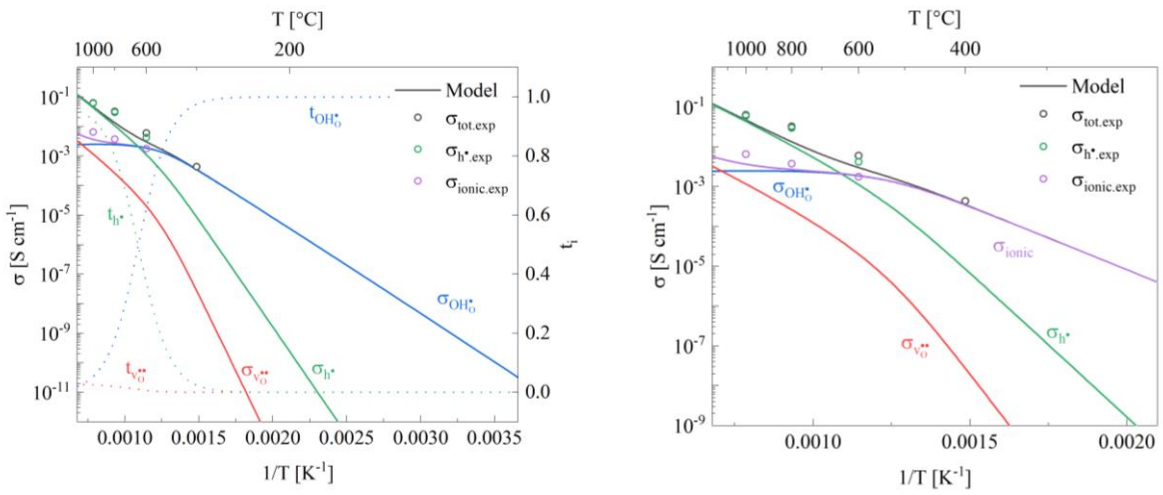

Figure 55: Partial conductivity for protons, oxide ions and holes in humid oxygen ($p_{H_2O} = 0.026\ atm$ & $p_{O_2} = 0.97\ atm$) with transport numbers for BSZCYNi1.

5.6.5.2 BSZCY151020 – 1wt.%CuO - 1400°C – 12h (BSZCYCu1)

The modelled partial conductivities with transport numbers for BSZCYCu1 are presented in humid argon, dry air and humid oxygen in Figure 56, Figure 57, and Figure 58, respectively.

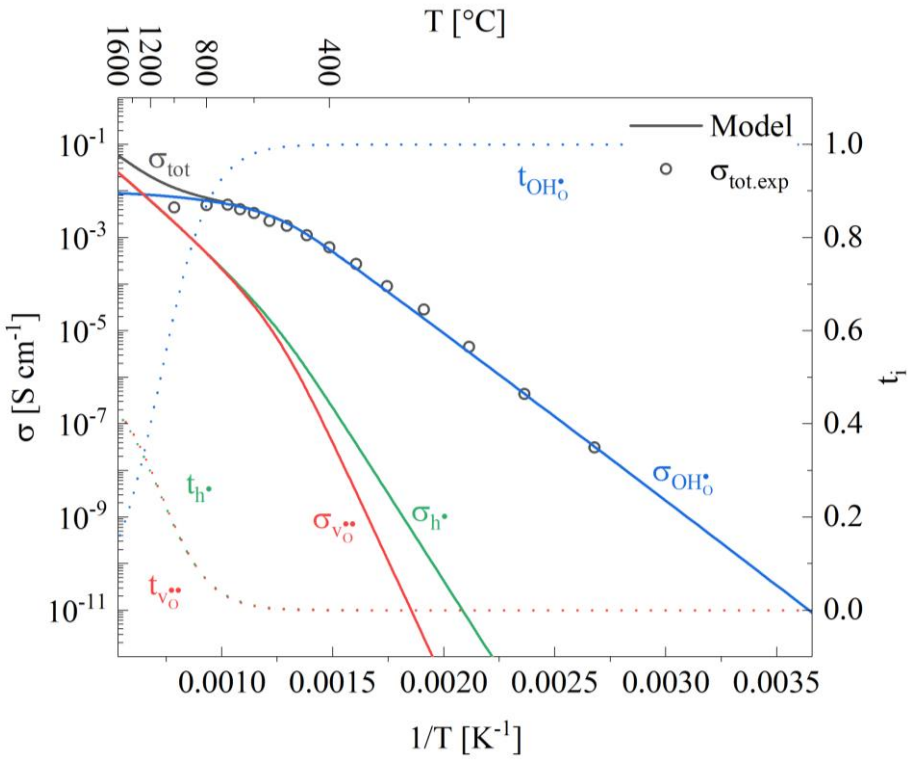

Figure 56: Partial conductivity for protons, oxide ions and holes in humid argon ($p_{H_2O} = 0.026\ atm$ & $p_{O_2} = 2 * 10^{-6}\ atm$) with transport numbers for BSZCYCu1.

For the BSZCYCu1 sample the deviation in the fitting is most prominent with the data obtained in dry air in Figure 57, where the partial conductivities don't add up to a perfect representation of the slope of the data points.

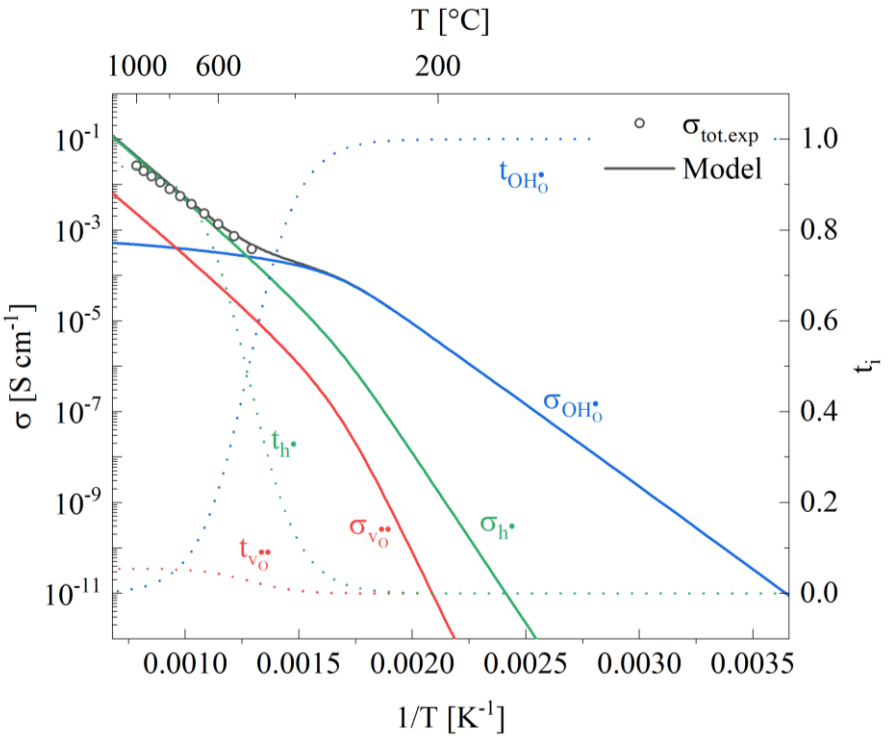

Figure 57: Partial conductivity for protons, oxide ions and holes in dry air ($p_{H_2O} = 10^{-5}\ atm\ \&\ p_{O_2} = 0.21\ atm$) with transport numbers for BSZCYCu1.

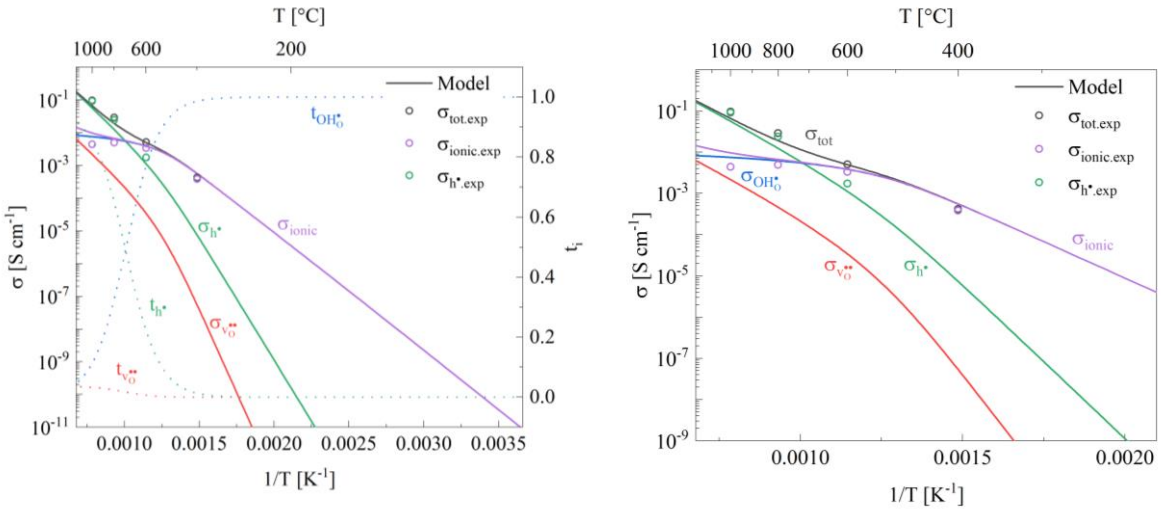

Figure 58: Partial conductivity for protons, oxide ions and holes in humid oxygen ($p_{H_2O} = 0.026\ atm\ \&\ p_{O_2} = 0.97\ atm$) with transport numbers for BSZCYCu1.

5.6.6 Schottky barrier

The Schottky barrier height or potential for the grain boundaries was found using Mott-Schottky theory for space charge layers, solved for protons (2.234). The expression was solved numerically with python (9.1) with bulk and specific grain boundary conductivities. The results for barrier height and correlating space charge length are presented in Table 25 and Table 26, respectively. The space charge layer length (λ^*) was found with the correlating values for $[Y'_{Zr,eff}]$, $\Delta\varphi$ (0), and ε_{gb} (C_{gb}) for the two samples by expressions (2.235) and (2.237).

Table 25: Schottky barrier height for samples characterized by EIS, calculated numerically.

Sample	*$\Delta\varphi$ (0) [V]*				*Atmosphere*
Temperature	30°C	100°C	200°C	300°C	
BSZCYCNi1	--	0.20	0.18	0.25	Humid Ar
BSZCYCu1	--	0.30	0.31	0.34	Humid Ar
BS(YSZ)CYCu05	0.15	0.19	0.20	0.31	Humid Ar

Table 26: Space charge layer length for corresponding space charge potentials.

Sample	*λ^* [nm]*				*Atmosphere*
Temperature	30°C	100°C	200°C	300°C	
BSZCYNi1	--	1.41	1.13	1.43	Humid Ar
BSZCYCu1	--	3.41	3.26	3.18	Humid Ar
BS(YSZ)CYCu05	2.22	2.61	2.41	3.34	Humid Ar

5.7 Dielectric loss and trapping

The dielectric loss was calculated from impedance according to the relationship (3.600) for each EIS measurement in humid argon at temperatures below 550°C:

$$\tan(\delta) = \left|\frac{Z'}{Z''}\right| \tag{5.700}$$

The dielectric loss tangent for all samples contains two sets of relaxations that result in heat loss. The two mechanisms are associated with the two peaks observed in Figure 59, which for BSZCYCu1 (b) are more isolated than for the BSZCYNi1 (a) and BS(YSZ)CYCu05 (c) which show a slight overlap at higher temperatures. The latter shows a static behaviour at low temperatures for the high frequency peak, and then at 30°C (red) the peak becomes very prominent.

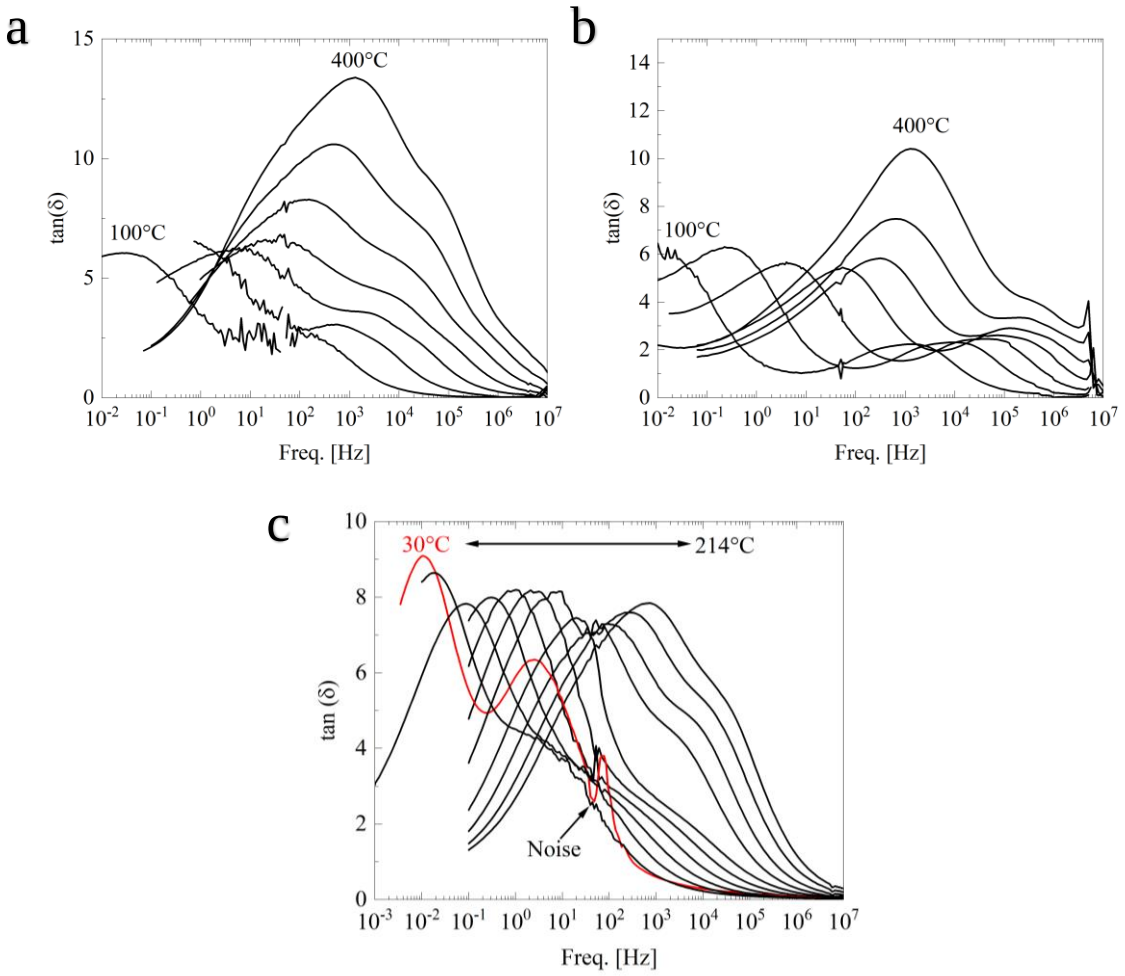

Figure 59: Dielectric loss tangent for a) BSZCYNi1, b) BSZCYCu1 and c) BS(YSZ)CYCu05 as a function of frequency and temperature.

All processes are getting faster as temperature increases, that is moving to higher frequencies. In addition, dielectric loss tangent for bulk disappears above 400°C, which is probably indicative to the relaxation mechanism being too fast (to high frequency). The dielectric loss is converging at low temperature, in the case of low frequency peak for BSZCYCu1 a slight increase is observed.

The peak value $\tan(\delta)_{max}$ and the correlating resonance frequency (f_{max}) were extracted to the best ability graphically from the plots in Figure 59 for each temperature. These values were plotted separately as ($\tan(\delta)_{max} \times T$) and ($f_{max} \times T$) versus temperature to extract, association and migration enthalpies, respectively.

The dielectric loss tangent peak values for high frequency for the three samples are presented in Figure 60 in an Arrhenius plot. BSZCYNi1 and BSZCYCu1 show a transition in linearity at 200°C, while BS(YSZ)CYCu05 show a deviation under 150°C which may be due to inaccurate extraction of peak values.

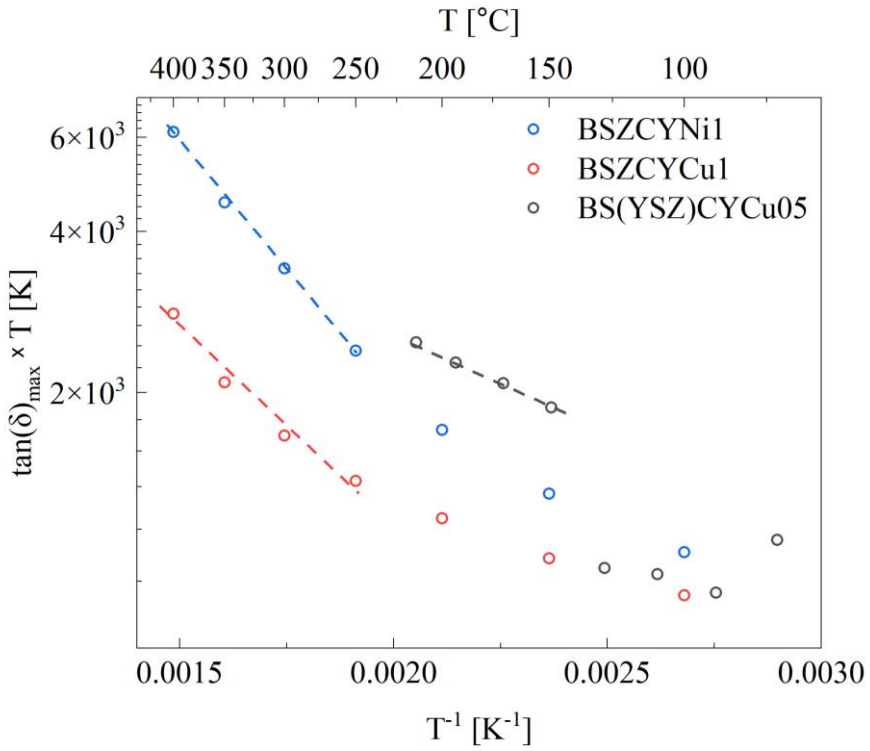

Figure 60: High frequency (bulk) dielectric loss versus temperature for BS(YSZ)CYCu05 (black), BSZCYNi1 (blue) and BSZCYCu1 (red) with dashed lines illustrating linear regressions.

The same shift in slope is more identifiable in the loss peaks for low frequency peaks in Figure 61, where the $\tan(\delta)_{max}$ virtually flattens out under 250°C.

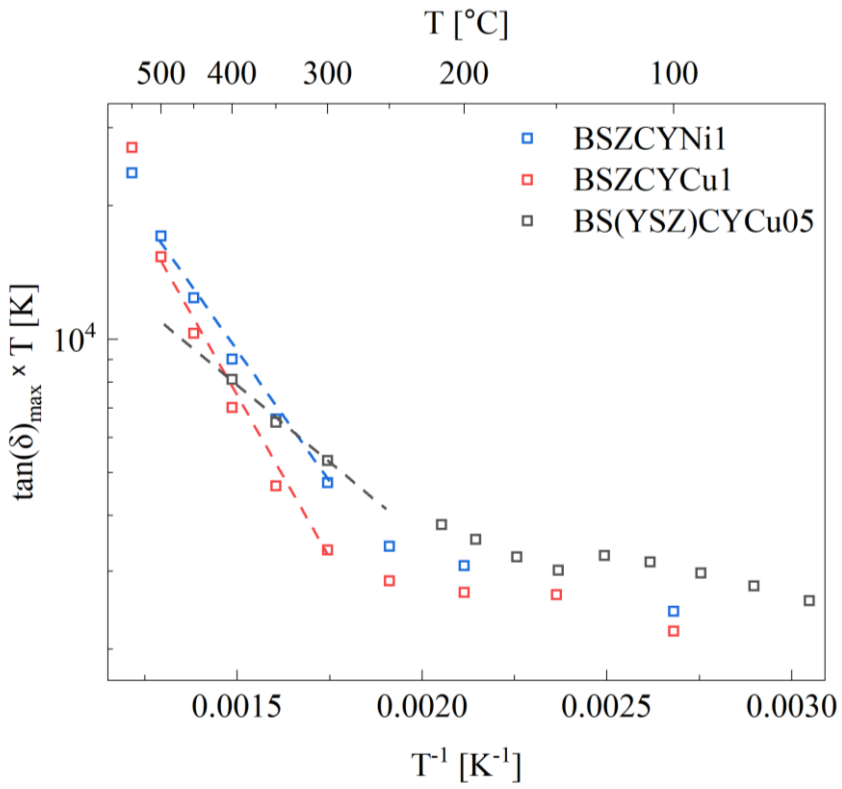

Figure 61: Low frequency (GB) dielectric loss versus temperature for BS(YSZ)CYCu05 (black), BSZCYNi1 (blue) and BSZCYCu1 (red) with dashed lines illustrating linear regressions.

The resonance frequencies associated with the dielectric loss maximum are presented in Figure 62 in an Arrhenius plot. The resonance frequencies follow a linear trend.

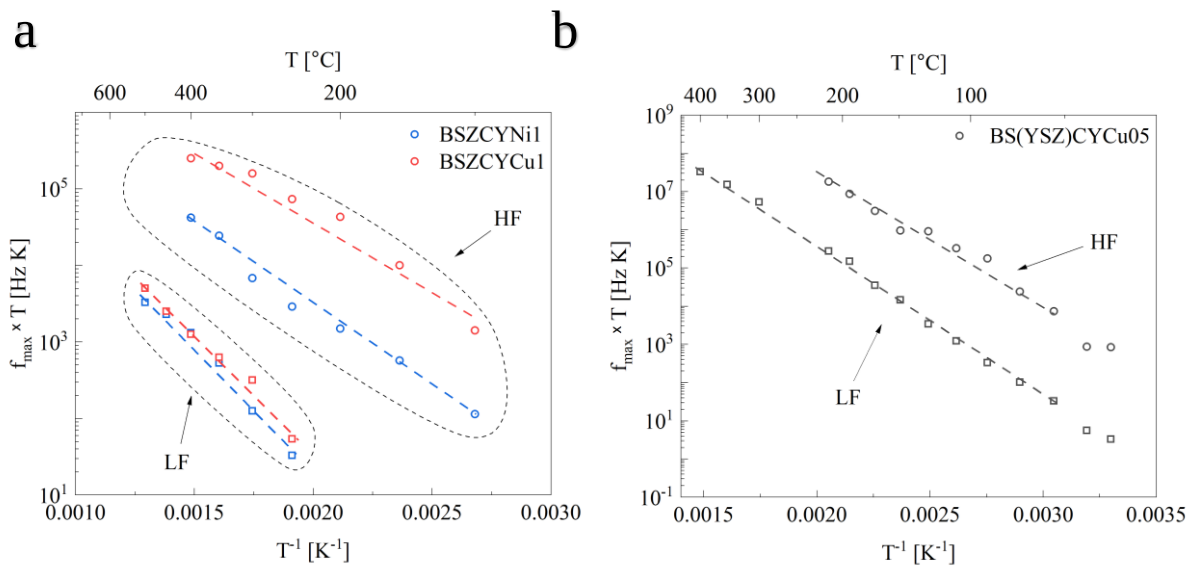

Figure 62: Peak (resonance) frequencies obtained from $\max(\tan(\delta))$ for a) BSZCYNi1 (blue) and BSZCYCu1 (red), and b) BS(YSZ)CYCu05 for both bulk and grain boundary.

The activation energies for the dielectric loss tangent and frequencies presented above were extracted with Arrhenius expression for tan(δ) (3.602) and frequency (3.603). The extracted values are presented in Table 27 and

Table 28, respectively for high and low frequency relaxation processes. For comparison, the bulk and grain boundary activation energies are presented with HF and LF association and migration energies, respectively. In addition, the expression $E_{a,aperant} = E_{a,mig} - E_{a,ass}$ is tested in the right columns.

Table 27: Activation energies for migration and association, obtained from resonance frequencies and tan(δ)-peak values for high frequency relaxation. The bulk activation energies are obtained from conductivity in humid argon.

Sample	$\boldsymbol{E_{a,bulk}}$ $[\boldsymbol{kJ\ mol^{-1}}]$	$\boldsymbol{HF - E_{a,mig}}$ $[\boldsymbol{kJ\ mol^{-1}}]$	$\boldsymbol{HF - E_{a,ass}}$ $[\boldsymbol{kJ\ mol^{-1}}]$	$\boldsymbol{E_{a,mig} - E_{a,ass}}$ $[\boldsymbol{kJ\ mol^{-1}}]$
BSZCYNi1	58 ± 3 $(400 - 100°C)$	44 ± 2 $(400 - 100°C)$	-18 ± 1 $(400 - 250°C)$	62 ± 4
BSZCYCu1	58 ± 2	40 ± 3	-14 ± 2	54 ± 5

	$(400-100°C)$	$(400-100°C)$	$(400-250°C)$	
BS(YSZ)CYCu05	63 ± 2 $(400-55°C)$	62 ± 3 $(400-55°C)$	-7 ± 1 $(214-149°C)$	70 ± 4

Table 28: Low frequency and GB activation energies.

Sample	$E_{a,gb}$ $[kJ\ mol^{-1}]$	$LF-E_{a,mig}$ $[kJ\ mol^{-1}]$	$LF-E_{a,ass}$ $[kJ\ mol^{-1}]$	$E_{a,mig}-E_{a,ass}$ $[kJ\ mol^{-1}]$
BSZCYNi1	73 ± 5 $(400-100°C)$	54 ± 5 $(500-350°C)$	-23 ± 1 $(500-300°C)$	78 ± 6
BSZCYCu1	75 ± 2 $(400-100°C)$	61 ± 3 $(500-350°C)$	-28 ± 2 $(500-300°C)$	89 ± 5
BS(YSZ)CYCu05	66 ± 2 $(400-55°C)$	76 ± 1 $(400-55°C)$	-9 ± 1 $(400-149°C)$	85 ± 2

6 Discussion

This chapter consist of discussion centred around three subjects. The first subject is that of the applied fabrication method, SSRS, the second is the impression of the electrochemical transport properties, fittings and obtained parameters, and the last considers the dielectric loss tangent, trapping and their correlation.

6.1 SSRS

Considering the dilatometry studies, the trends when using YSZ indicate a slight increased densification compared to only using binary oxides and carbonates, which is further confirmed by SEM studies. This may be related to the kinetics of grain growth:

$$\frac{dD}{dt} = \frac{k}{D} \tag{6.100}$$

where D is the grain diameter and k is the rate constant. Indicating that small particles of YSZ (<40nm) contribute to increased sintering compared to using zirconia (<5μm) and yttria (<20μm). This applies for all samples, also those without sintering aid.

The initial shrinkage (Figure 63 at 1100°C), which is ranging from -0.5 to -1%, for pristine and NiO added samples was believed to be the allotropic change of zirconia from monoclinic to tetragonal. This was confirmed by measuring dilation on a pure pre sintered zirconia sample, which showed the same amount of shrinkage (Figure S 1). However, the onset was about 150°C higher than that observed for the green powders and corresponds to the phase transition temperature reported in literature [56]. Due to partial substitution of yttria in zirconia the martensitic transition can be expected at a lower temperature, which is observed in a thermal cycling study by Tsubakino et al. [59] for a pre sintered 3mol% yttrium stabilized composition. This composition exhibits the M → T when heating at approximately 600°C. Many factors may affect the degree of M → T, of these CeO_2, alumina, and grain size. The tetragonal phase change is not observed when utilizing YSZ as a precursor as it is stabilized in the tetragonal phase from the beginning.

The following expansion is due to the decomposition of carbonates, where the phase of cubic $BaCO_3$ in the HT-XRD patterns is disappearing at similar temperature. In addition, this peak is not observed for pre calcined (1250°C) green powders of BZY20 [60], which supports why carbon dioxide evolution is associated with the expansion.

The CuO containing samples do not portray the initial shrinkage of the monoclinic to tetragonal phase transition of zirconia. Instead, it shows an expansion with onset at approx. 950°C. This expansion is attributed the reduction of copper as found in the oxidation phase diagram [57]:

$$CuO \rightarrow Cu_2O + \frac{1}{2}O_2 \tag{5.200}$$

The expansion might be inherent to the monoclinic to cubic phase transition of the reduction, which almost doubles the volume of the unit cell. Figure 63 summarises the macroscopic changes observed for NiO and pristine samples, with the M → T transition and carbonate decomposition, and the changes for CuO samples.

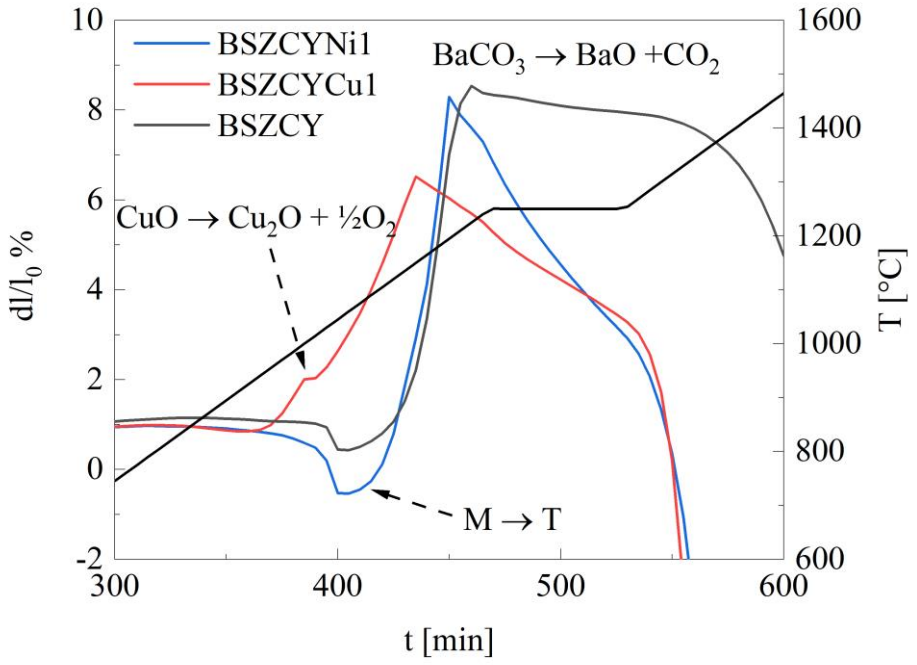

Figure 63: Macroscopic changes attributed the dilation curves for pristine BSZCY, with NiO and with CuO.

Although the effective acceptor concentration was improved from an average of $\left[Y'_{Zr,eff}\right] \approx$ 8% in batch 1 to 12% in batch 3 and 4, the effective acceptor concentration was relatively low compared to that of nominal BZY [35-37]. The improvement is a result of three factors: correct stoichiometry of sacrificial powders with excess barium carbonate, less sintering additive and longer sintering time for the pristine samples. There are probably more factors that can and should be optimized in the fabrication method to reach an overall higher effective acceptor concentration. One of the reasons for utilizing YSZ as a precursor was with the hypothesis of

increased hydration, because it is already doped with yttrium. The results indicate that it does not affect hydration to any notable degree, in fact BS(YSZ)CY showed a lower proton concentration than BSZCY.

The relative increase in effective acceptor concentration from BSZCYNi1 to BSZCYNi1(O2) is probably due to excess barium carbonate in the sacrificial powder in combination with the flow of gas. The latter will contribute to the removal of carbon dioxide, thus decreasing the volatility of barium. Including carbon dioxide in the proposed expression from theory (2.112) gives the equilibrium that should be affected by flow of oxygen:

$$CO_2 + Ba_{Ba}^{x} + O_O^{x} = v_{Ba}'' + v_O^{\cdot\cdot} + BaCO_3 \tag{5.201}$$

6.2 Transport properties of BSZCY151020

In the present work, only samples with sintering additives were measured by EIS, as the ones without tended to crack upon removal from the furnace. EIS measurements revealed a lowered total conductivity compared to Dayaghi's results [4] in humid argon (Figure 46a) for pristine BSZCY151020. At 600°C the three samples from this work exhibit a total conductivity of $(2-3) mS\ cm^{-1}$ in humid argon, while the pristine reference sample exhibit $5 mS\ cm^{-1}$[4]. For discussion purposes, the total conductivity for a fully substituted yttrium sample could yield a $\sim 1.5\ mScm^{-1}$ increase to the total conductivity at 600°C. This was estimated by using the model (Table 24) for BSZCYNi1, but with $\left[Y'_{Zr,eff}\right] = 0.2$ (20mol%) instead of the one found by TG. This indicates that the difference in conductivity could be explained by different proton concentrations.

Total conductivities for selected samples in humid conditions ($p_{O_2} = 2 \times 10^{-6} atm$) at 600°C are presented in Table 29. The activation energy in the interval 400-150°C for the pristine sample [4] is approximately $68\ kJ\ mol^{-1}$, which would be an estimate of the proton mobility enthalpy. The difference is small when compared to BSZCYNi1 ($\sim 65\ kJ\ mol^{-1}$), BSZCYCu1 ($\sim 72\ kJ\ mol^{-1}$) and BS(YSZ)CYCu05 ($\sim 63\ kJ\ mol^{-1}$) from this work. For BZY10 the mobility enthalpy of protons is found to be around $42\ kJ\ mol^{-1}$ [19, 37, 44] and for BZY20 $43\ kJ\ mol^{-1}$ [61]. Comparing BSZCY151020 with BZY its evident that the mobility of protons is the limiting factor for conductivity in BSZCY151020. Suggesting that proton hopping in BSZCY requires more energy. This could be inherent to the strontium content, as the Sr – Y bond has a higher binding energy than Ba – Y bond [62], which in turn means that protons will exhibit a stronger columbic attraction to a yttrium bonded with strontium. Which would

increase the association energy of the trapped defect pair that is described by Yamazaki [9], thus impeding the proton mobility more. From HT-XRD its evident that perovskite formation consists of several compositions, where $SrZrO_3$ is proposed as one.

Table 29: Total conductivity at 600°C in humid conditions.

Composition	**Sintering temp.**	**Total conductivity at 600°C** $[mScm^{-1}]$	**Atmosphere**	**Reference**
BSZCYNi1	1400°C – 12h	2.0	Wet Ar	This work
BSZCYCu05	1400°C – 12h	2.5	Wet Ar	This work
BSZCYCu1	1600°C – 12h	3.3	Wet Ar	This work
BSZCY151020	1650°C – 24h	5	Wet Ar / 5% H_2	[4]
BZY20	1600°C – 24h	7.9	Wet N_2	[61]

6.2.1 The effects of sintering additives on BSZCY

Copper may impose alternating properties in BSZCY151020 as measurements were conducted in both reducing and oxidising atmospheres. Phase diagram for copper as a function of partial pressure oxygen (Torr) and temperature (Celsius) is presented in Figure 64 and is used as support for this discussion.

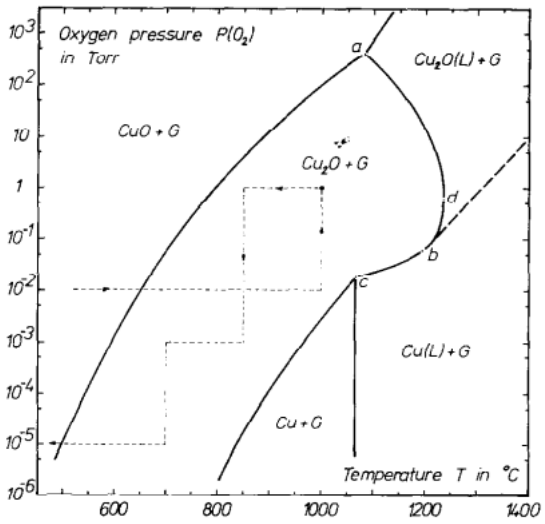

Figure 64: Copper Oxide phase diagram by degrees Celsius and oxygen pressure in Torr from R. D. Schmidt-Whitley [57].

Firstly, copper is expected to be reduced at high temperatures during sintering and probably forms a liquid-phase, as is indicated by the pores in Figure 31, which is also seen in the study by Nikodemski et al. [32]. Because of the high content of copper in BSZCYCu1 (1wt.%), segregation of CuO might be present, as observed in SEM (Figure 29). The segregates are mostly situated around the grain boundary, which correlates to the observation by Han et al. [6] where $at.\%_{Cu\ in\ GB} > at.\%_{Cu\ in\ grain\ interior}$ for BZY20. If we assume that the oxidation and reduction reactions apply for the grain boundary, the reduction and oxidation of CuO may result in dissolution and possibly re-segregation, respectively. The redox reaction could be presented as:

$$2CuO_{seg} + v_O^{\cdot\cdot} = 2O_O^x + 2Cu_{GB}^{\cdot} \tag{5.202}$$

where GB is treated as a general site for copper, for simplicity. To elaborate, the electrochemical gradient between the grain boundary and atmosphere induces diffusion of copper, which is also supported by the high temperature under EIS measurements and under sintering. Still, this would happen at a relatively slow rate, which would explain why segregates are not observed post EIS measurements. Indicating that the system was cooled too quickly and/or cooled in reducing atmosphere.

Coincidently, the reduction of copper in argon ($1.5 \times 10^{-3}\ Torr$) at 600°C seem to align with a decrease in bulk conductivity for BSZCYCu1, as indicated in Figure 65 (with reference from low to high temperature). This decrease in conductivity is too abrupt when considering the nature of dehydration. However, calculating $\Delta G = 0$ ($K_{hydr} = 1$) from the enthalpy and

entropy of hydration for BSZCYCu1 yields $T = \sim 550°C$, which means that BSZCYCu1 is expected to start dehydrating at temperatures $> 550°C$. The same abrupt change in bulk conductivity for BSZCYNi1 and BS(YSZ)CYCu05 is not observed, even though the initial dehydration temperature is virtually equal. To give an overinterpretation, this artifact could be associated with redox reaction proposed for CuO (5.202), but with dissolution into grain interiors. Which then may act impeding due to oxygen vacancy annihilation.

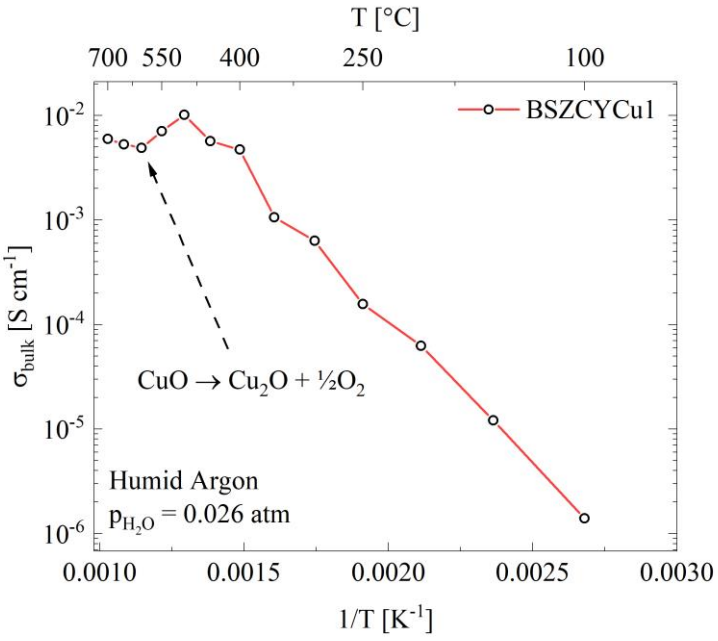

Figure 65: Proposed mechanism of copper oxide in BSZCY151020.

The difference in proton concentration in samples with CuO compared to NiO in Figure 42 might correlate to the fact that CuO dissolves to a lesser degree into the grain interior than NiO as found by Han et al. [6]. This suggests that nickel contribute to the annihilation of oxygen vacancies by formation of nickel interstitials (2.115) or as suggested by Polfus et al. [33], by association with barium vacancies (3.201), to a higher degree then CuO. As a result, Cu does not affect proton concentration to the same extent as Ni, which has been observed in Figure 42 & Figure 41.

Further studies need to be conducted to reveal the full scope of CuO in BZY or BSZCY perovskites, both under fabrication and under electrochemical performance in varying conditions.

6.2.2 Transport model

The obtained parameters through fitting of conductivity in different atmospheres have yielded two models for transport in BSZCYNi1 and BSZCYCu1. The resulting parameters show reasonable values compared with other compositions from literature [38, 40-45]. However, there are some uncertainties not portrayed by the R-square error values from the final fitting in humid argon. Firstly, this error value is not inherent to the conductivity data in dry air and humid oxygen, which means there is no quantitative value to explain the interrelations of the fit with respect to the data in these conditions. Secondly, there are no precise way to add the discrepancies and errors of the data collecting procedures, which means errors from TG, EIS and subsequent deconvolutions will factor into the result. In addition, the conductivity data portrayed an oxygen vacancy and hole activation energy of similar magnitude, this will lower the accuracy of the fittings as they are dependent on characteristics in the curves.

The highest uncertainty must be expected for the pre-exponential values as these are dependent on boundaries in the fitted data, which may lay outside the temperature range of the collected conductivities. The pre-exponentials and enthalpies are compared with values for BZCYYb1711 from Kim et al. [45] in Table 30 to evaluate the feasibility of the obtained parameters. The values for oxygen vacancies and holes seem to be reasonable with respect to that observed in BZCYYb1711 and suggest that the modelling is executed within acceptable boundaries with respect to different saddle points in the functions. To elaborate, the parameters can have several sets of values that would correspond to a good fitting.

Table 30: Comparison of mobility parameters for BSZCYNi1, BSZCYCu1 and BZCYYb1711.

Parameter	**Units**	**BSZCYNi1**	**BSZCYCu1**	**BZCYYb1711 [45]**
$u^0_{OH_O^\cdot}$	$[cm^2\ K\ V^{-1}s^{-1}]$	181	1072	33
$\Delta H_{OH_O^\cdot,mob}$	$[kJ\ mol^{-1}]$	65	72	48

σ_p^0	$\left[cm^2\ K\ V^{-1}s^{-1}\ atm^{-\frac{1}{4}}\right]$	850	2149	1666
$\Delta H_{p,a}$	$[kJ\ mol^{-1}]$	86	93	76
$u_{v_O^{\cdot\cdot}}^0$	$[cm^2\ K\ V^{-1}s^{-1}]$	91	241	263
$\Delta H_{v_O^{\cdot\cdot},mob}$	$[kJ\ mol^{-1}]$	89	92	76

It must be stated that the values for holes from Kim et al. are obtained by fittings of conductivity versus partial pressure of oxygen, which make them more comparable to the values obtained by the same fitting in this work (5.6.4). These values are very similar, with an average of $\sim 70 kJ\ mol^{-1}$ for BSZCYNi1 and BSZCYCu1 in this work compared to $76 kJ\ mol^{-1}$ for BZCYYb1711 [45]. The pre-exponential and mobility enthalpy values for holes in BSZCYNi1 and BSZCYCu1 obtained by fitting versus temperature (Table 30) are slightly higher than those obtained from fitting versus partial pressure of oxygen (Table 23). This is inherent to the increased mobility of holes at higher temperatures, which is not extracted in isothermal fitting.

An empirical ratio between proton mobility and oxygen vacancy mobility can be deduced from results in literature:

$$\frac{\Delta H_{OH_O^{\cdot},mob}}{\Delta H_{v_O^{\cdot\cdot},mob}} \approx \frac{2}{3} \tag{6.201}$$

This estimate is also seen in the obtained values (Table 30) and lay between $\frac{7}{10}$ to $\frac{8}{10}$ for protons and oxygen vacancies in BSZCYNi1 and BSZCYCu1. The relationship has to do with the mechanisms of transport and the difference in charge. The jump distance is shorter for protons then oxygen ions and the charge is smaller, thus transport requires less energy. Since the two are affected by the same framework of neighbouring ions the approximate ratio can be observed for several mixed proton-oxide ion conductors in literature.

6.2.3 Schottky barrier

The grain boundary core consists of higher concentrations of positive cations than anions, in which the most displaced cations in the nominal lattice are expected to dominate, such as yttrium, copper and nickel. The segregation in BSZCYCu1 might affect the grain boundary space charge as it is situated in and around the grain boundary. If the segregation is copper

oxide, it might act as an insulating phase for protons which then contributes a decrease in measured grain boundary conductivity. Thus, the space charge potential is increased. Since space charge potential for BS(YSZ)CYCu05 and BSZCYNi1 are more similar, it might indicate that the segregates act impeding on protons in BSZCYCu1.

The results at 200°C are compared with literature values at the same temperature for BZY and a BSCZGdY composition in Table 31. The space charge layer length is reasonable compared to the other studies, while the space charge potential is generally lower in this study. The reason for this might be inherent to the composition or the sintering method. The latter is indicated by the relatively high variation of potentials with respect to fabrication of BZY in Table 31.

Table 31: Space charge potential and length at 200°C for selected samples. Sintering methods with sintering temperature are abbreviated SSR, SPS, HP and SSRS, respectively solid-state reaction, spark plasma sintering, hot press, and solid-state reactive sintering. If not stated, the partial pressure of water is $p_{H_2O} = 0.026atm$.

Composition / reference	**Atmosphere**	$\Delta\varphi(0)$ $[V]$	λ^* $[nm]$
BSZCYNi1 This work (1400°C)	Humid argon	0.18	1
BSZCYCu1 This work (1400°C)	Humid argon	0.31	3
BS(YSZ)CYCu05 This work (1600°C)	Humid argon	0.20	2
$Ba_{0.5}Sr_{0.5}Ce_{0.6}Zr_{0.2}Gd_{0.1}Y_{0.1}O_{3-\delta}$ [52] (SSR-1300°C)	3% H_2O / H_2	0.35	2
$Ba_{0.5}Sr_{0.5}Ce_{0.6}Zr_{0.2}Gd_{0.1}Y_{0.1}O_{3-\delta}$ [52] (SSR-1400°C)	3% H_2O / H_2	0.40	2
BZY10 [10] (SPS-1600°C)	Humid oxygen	0.51	4.3

BZY10 [10] (HP-1650°C)	Humid oxygen	0.63	4
BZY10 + 1wt.% NiO [63] (SSR-1600°C)	3% H_2O/ 5% H_2 / N_2	0.20	1.3
BZY10 + 1wt.% NiO [63] (SSRS-1535°C)	3% H_2O/ 5% H_2 / N_2	0.04	0.5
BZY20 [64] (SSR-1600°C)	3.2% H_2O / N_2	0.37	4.9

6.3 Dielectric loss tangent and trapping

The dielectric loss tangent is not the most intuitive property too study, but with reference to literature it is possible to discuss the results that is obtained. Thus, the framework of this discussion centres around comparison to literature. In literature the dielectric loss tangent is typically used to extract association energies of trapped ionic charge carriers that exhibit relaxation. It must be noted that because of the estimation of $\tan(\delta) \propto \varepsilon''$ association energies rarely have a concluding association to a particular relaxation mechanism.

Firstly, the plot of $\tan(\delta)$ versus frequency reveals two peaks, one at high frequency (HF) and one at low frequency (LF) for the three samples (Figure 59). The HF and LF peaks may be correlated to bulk and grain boundary region, respectively. This can be investigated by evaluating the proportionality of resonance frequency from impedance ($f\ at\ Z''_{max}$) to that of dielectric loss tangent ($f\ at \tan(\delta)_{max}$) versus temperature, if they are proportional they should be inherent to the same region in the material [46]. The proportionalities were checked, and showed for all samples that the activation energy of $f_{Z''}\ and\ f_{\tan(\delta)}$ versus temperature is similar according to Arrhenius expression (3.603), which is visualised in Figure 66 for one sample (BSZCYCu1).

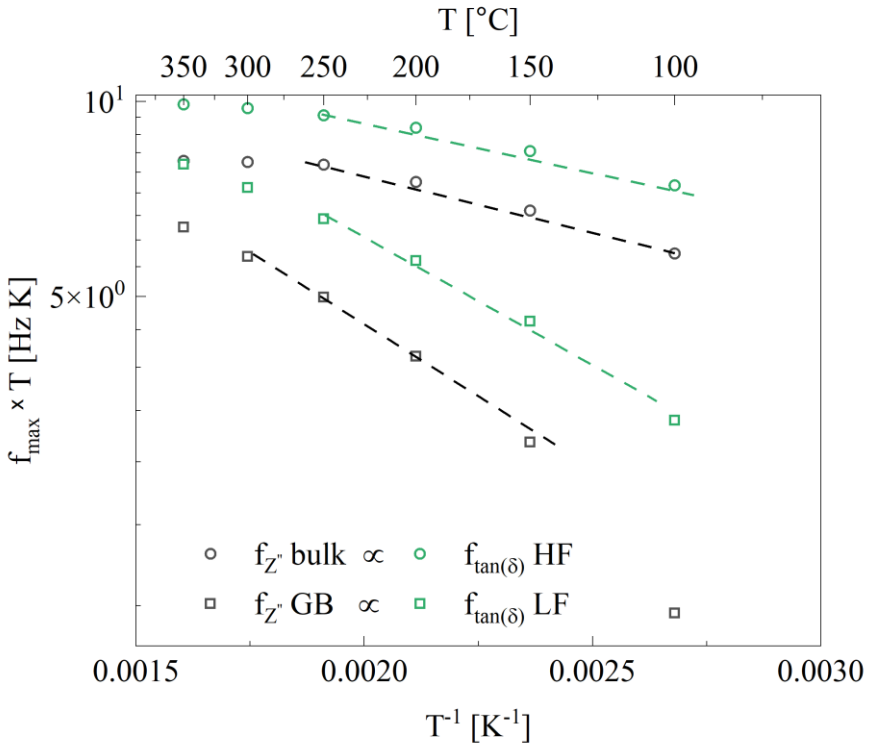

Figure 66: Proportional resonance frequencies for impedance and dielectric loss tangent for BSZCYCu1.

Therefore, we can attribute the high frequency loss peak with bulk and the low frequency loss peak with grain boundary for all samples. This indicates that the energy loss for the two mechanisms is inherent to relaxation in bulk and grain boundary. The discussion is then ultimately about which relaxation mechanism is responsible for each extracted association energy and if at all that can be determined. The goal was to determine association energies for a particular permanent dipole in bulk, namely the yttrium-proton association.

The association values obtained for BSZCYNi1, BSZCYCu1 and BS(YSZ)CYCu05 are compared with literature values in Table 32. From the comparison its evident that the values obtained have reasonable magnitude. If we assume that association energy decreases with yttrium content as observed from the values in literature ($E_{ass}\ (BZY20) > E_{ass}(BZY3.7)$), the low effective acceptor concentration in the present study may be an indication of lowered association energy for the yttrium-proton trap. This can be inherent to the lowered possibility of forming clusters of yttrium octahedra, which could increase the binding to the proton that is trapped. The difference between the association energies associated with bulk and grain

boundary region could be indicative of increased acceptor concentration in the region or it could be related to other mechanisms. Polarisation of free charge in the space charge region might be related to a relaxation and could be one of the mechanisms in GB.

Table 32: Association energy values for Y – OH trap.

Composition	**E_{ass} [kJ mol^{-1}] (mechanism)**	**Reference / method**
BSZCYNi1	18 (bulk) 23 (GB)	This work / tan(δ)
BSZCYCu1	14 (bulk) 28 (GB)	This work / tan(δ)
BS(YSZ)CYCu05	7 (bulk) 9 (GB)	This work / tan(δ)
BZY20	29 (Y -OH)	[9] / Diffusivity calculations
BZY	25 (Y -OH)	[53] / calculations
BZY3.7	15 (Y -OH)	[54] / calculations

The results suggest a relatively high deviation in the relationship $\left(E_{a,mobility} = E_{a,migration} - E_{a,association}\right)$ as presented earlier (Table 27 & Table 28), especially for the sample BS(YSZ)CYCu05 where the migration and apparent activation (mobility) energy in bulk are virtually similar. In addition, the relation does not seem to apply for the grain boundary results (Table 28). One can argue that three different linear regression will amount to considerable error and that the extraction of values graphically for dielectric loss tangent is not very precise, especially where peaks are overlapping. Furthermore, the temperature range chosen for linear regression to obtain E_{ass} and E_{mig} may have a big impact on the extracted values and on the earlier mentioned relation, as small shifts in temperature may lead to large variations in the activation energy.

In summary, the association energy related to bulk region may be inherent to the yttrium-proton, while the value for grain boundary is higher and may indicate either increase in traps or other relaxation mechanisms. Further work is needed.

6.4 Further work

The electrochemical transport properties for BSZCY151020 have been exposed with estimates of enthalpy of mobility for protons and oxygen vacancies, and activation enthalpy for holes. These parameters model conductivity as a function of temperature and partial pressure of oxygen with high precision. However, the proton conducting abilities are to a degree limited by low hydration. Thus, further studies on the limiting factor of hydration should be conducted to interpret the challenges with this electrolyte contender.

Furthermore, mobility values for protons are relatively high compared to that of nominal yttrium doped barium zirconate. As proposed, this might be an effect of increased bond strength between strontium and yttrium, which may also increase the trapping effect as discussed. The latter phenomenon requires further understanding, especially in relation to dipole relaxation. A thorough investigation of dielectric loss tangent should be studied at medium to low temperatures with smaller temperature intervals for more precision. Such a study would also benefit from DFT calculations of similar compositions for comparison. A further bridging between complex permittivity, relaxation, and EIS should be in focus for further studies regarding proton conductors, as it might reveal trapping dynamics in an already conventional measuring technique (EIS).

Further in situ XRD studies should be done to reveal the phase transitions involved during sintering of samples with YSZ, NiO and CuO. These effects should also be studied for precursor mixtures with similar grain size to determine effects on densification.

Further experiments should be conducted to uncover the effects of CuOs possible alternating properties in reducing and oxidising conditions.

7 Conclusion

The electrochemical transport properties of BSZCY151020 with sintering additives have been investigated by a model fitting of conductivity versus temperature and partial pressure of oxygen in humid and dry conditions. Between the three samples that were measured a conductivity around 2 to 3 $mScm^{-1}$ in humid argon at 600°C was found, with indication of limiting factors being proton mobility enthalpy. Which was found to be higher compared to nominal BZY, and is proposed to reflect increased association energy from hydroxide – yttrium pairs bonded to strontium instead of bonded to barium. Furthermore, the oxygen vacancy mobility enthalpy conformed to the 2/3 empirical relationship with protons. The electron hole conductivity showed a ¼ dependency of $\log(p_{O_2})$ at elevated temperatures, similarly to BZY.

Relaxation properties were extracted by estimating $\tan(\delta) \propto \varepsilon''$. Two relaxation mechanisms were observed as peak values for the dielectric loss tangent. The change in resonance frequency of impedance and $\tan(\delta)$ with temperature was proportional, thus the two peaks were attributed to grain boundary and bulk region. The latter showed similar magnitude in association energy to that reported in literature, which suggests that the relaxation is due to trapped protons around YO_6 octahedra.

The effects of sintering additives and sintering conditions in SSRS were studied. HT-XRD technique revealed that the $BaCO_3$ decomposition is the initial stage of the perovskite formation, in which several phases of the Pm-3m structure are present. This observation may be supported by the $SrZrO_3$ secondary phase seen in sintered samples. NiO added as a sintering aid reduced the effective acceptor concentration, while CuO had next to no effect, compared to pristine samples. Using YSZ as a precursor had no significant effect on the proton concentration, only a small increase in grain size diameter was observed.

8 Bibliography

1. Stambouli, A.B. and E. Traversa, *Solid oxide fuel cells (SOFCs): a review of an environmentally clean and efficient source of energy.* Renewable and Sustainable Energy Reviews, 2002. **6**(5): p. 433-455.
2. Biswas, M., *Solid Oxide Fuel Cell.* Journal of Powder Metallurgy & Mining, 2013. **02**(03).
3. Shim, J.H., *Ceramics breakthrough.* Nature Energy, 2018. **3**(3): p. 168-169.
4. Dayaghi, A.M., et al., *Increasing the thermal expansion of proton conducting Y-doped $BaZrO_3$ by Sr and Ce substitution.* Solid State Ionics, 2021. **359**: p. 115534.
5. Kim, E., et al., *Effect of NiO sintering-aid on hydration kinetics and defect-chemical parameters of $BaZr_{0.8}Y_{0.2}O_{3-\Delta}$.* Solid State Ionics, 2015. **275**: p. 23-28.
6. Han, D., et al., *Detrimental Effect of Sintering Additives on Conducting Ceramics: Yttrium-Doped Barium Zirconate.* ChemSusChem, 2018. **11**(23): p. 4102-4113.
7. Huang, Y., R. Merkle, and J. Maier, *Effects of NiO addition on sintering and proton uptake of $Ba(Zr,Ce,Y)O_{3-\delta}$.* Journal of Materials Chemistry A, 2021. **9**(26): p. 14775-14785.
8. Li, J., et al., *Sintering aids for proton-conducting oxides – A double-edged sword? A mini review.* Electrochemistry Communications, 2020. **112**: p. 106672.
9. Yamazaki, Y., et al., *Proton trapping in yttrium-doped barium zirconate.* Nature Materials, 2013. **12**(7): p. 647-651.
10. Kjølseth, C., et al., *Space–charge theory applied to the grain boundary impedance of proton conducting $BaZr_{0.9}Y_{0.1}O_{3-\delta}$.* Solid State Ionics, 2010. **181**(5-7): p. 268-275.
11. Shannon, R.D., *Revised effective ionic radii and systematic studies of interatomic distances in halides and chalcogenides.* Acta Crystallographica Section A, 1976. **32**(5): p. 751-767.
12. Bauerle, J.E., *Study of solid electrolyte polarization by a complex admittance method.* Journal of Physics and Chemistry of Solids, 1969. **30**(12): p. 2657-2670.
13. Beekmans, N.M. and L. Heyne, *Correlation between impedance, microstructure and composition of calcia-stabilized zirconia.* Electrochimica Acta, 1976. **21**(4): p. 303-310.
14. Verkerk, M., B. Middelhuis, and A. Burggraaf, *Effect of grain boundaries on the conductivity of high-purity ZrO_2 · Y_2O_3 ceramics.* Solid State Ionics, 1982. **6**(2): p. 159-170.
15. Haile, S.M., D.L. West, and J. Campbell, *The role of microstructure and processing on the proton conducting properties of gadolinium-doped barium cerate.* Journal of Materials Research, 1998. **13**(6): p. 1576-1595.
16. De Souza, R.A. and E.C. Dickey, *The effect of space-charge formation on the grain-boundary energy of an ionic solid.* Philosophical Transactions of the Royal Society A: Mathematical, Physical and Engineering Sciences, 2019. **377**(2152): p. 20180430.
17. De Souza, R.A., *The formation of equilibrium space-charge zones at grain boundaries in the perovskite oxide $SrTiO_3$.* Physical Chemistry Chemical Physics, 2009. **11**(43): p. 9939.
18. Guo, X. and R. Waser, *Electrical properties of the grain boundaries of oxygen ion conductors: Acceptor-doped zirconia and ceria.* Progress in Materials Science, 2006. **51**(2): p. 151-210.
19. Kreuer, K.D., *Proton-Conducting Oxides.* Annual Review of Materials Research, 2003. **33**(1): p. 333-359.

20. Souza, E.C.C.D. and R. Muccillo, *Properties and applications of perovskite proton conductors.* Materials Research, 2010. **13**(3): p. 385-394.
21. Goldschmidt, V.M., *Die Gesetze der Krystallochemie.* Die Naturwissenschaften, 1926. **14**(21): p. 477-485.
22. Yamada, I., A. Takamatsu, and H. Ikeno, *Complementary evaluation of structure stability of perovskite oxides using bond-valence and density-functional-theory calculations.* Science and Technology of Advanced Materials, 2018. **19**(1): p. 101-107.
23. Gonçalves, M.D., et al., *Enthalpy of formation and thermodynamic insights into yttrium doped $BaZrO_3$.* J. Mater. Chem. A, 2014. **2**(42): p. 17840-17847.
24. Stavrakakis, E., et al., *Hydration, CO2 stability and wireless electrochemical promotion studies on yttria-doped Ba (Ce, Zr) O_3 perovskites.* Ionics, 2019. **25**(3): p. 1243-1257.
25. Yamanaka, S., et al., *Thermophysical properties of $BaZrO_3$ and $BaCeO_3$.* Journal of Alloys and Compounds, 2003. **359**(1-2): p. 109-113.
26. Tolchard, J. and T. Grande, *Chemical compatibility of candidate oxide cathodes for $BaZrO_3$ electrolytes.* Solid State Ionics, 2007. **178**(7-10): p. 593-599.
27. Hudish, G., et al., *Chemical expansion in $BaZr_{0.9-x}Ce_xY_{0.1}O_{3-\delta}$ (x = 0 and 0.2) upon hydration determined by high-temperature X.* Journal of the American Ceramic Society, 2018. **101**(3): p. 1298-1309.
28. Yamazaki, Y., R. Hernandez-Sanchez, and S.M. Haile, *Cation non-stoichiometry in yttrium-doped barium zirconate: phase behavior, microstructure, and proton conductivity.* Journal of Materials Chemistry, 2010. **20**(37): p. 8158.
29. Loureiro, F.J.A., et al., *A review on sintering technology of proton conducting $BaCeO_3$-$BaZrO_3$ perovskite oxide materials for Protonic Ceramic Fuel Cells.* Journal of Power Sources, 2019. **438**: p. 226991.
30. Han, D., et al., *Strategy to improve phase compatibility between proton conductive $BaZr_{0.8}Y_{0.2}O_{3-\delta}$ and nickel oxide.* RSC Advances, 2016. **6**(23): p. 19288-19297.
31. Burtsev, V.T., V.V. Sidorov, and V.E. Rigin, *Interaction of barium oxyfluorochloride melts with refractories based on aluminum and magnesium oxides.* Russian Metallurgy (Metally), 2014. **2014**(11): p. 861-864.
32. Nikodemski, S., J. Tong, and R. O'Hayre, *Solid-state reactive sintering mechanism for proton conducting ceramics.* Solid State Ionics, 2013. **253**: p. 201-210.
33. Polfus, J.M., et al., *Solubility of transition metal interstitials in proton conducting $BaZrO_3$ and similar perovskite oxides.* Journal of Materials Chemistry A, 2016. **4**(21): p. 8105-8112.
34. Tong, J., et al., *Solid-state reactive sintering mechanism for large-grained yttrium-doped barium zirconate proton conducting ceramics.* Journal of Materials Chemistry, 2010. **20**(30): p. 6333.
35. Kreuer, K.D., et al., *Proton conducting alkaline earth zirconates and titanates for high drain electrochemical applications.* Solid State Ionics, 2001. **145**(1-4): p. 295-306.
36. Kreuer, K.D., et al., *Water solubility, proton and oxygen diffusion in acceptor doped BaCeO3: A single crystal analysis.* Solid State Ionics, 1996. **86-88**: p. 613-620.
37. Kreuer, K.D., *Aspects of the formation and mobility of protonic charge carriers and the stability of perovskite-type oxides.* Solid State Ionics, 1999. **125**(1-4): p. 285-302.
38. Ricote, S., et al., *Conductivity, transport number measurements and hydration thermodynamics of $BaCe_{0.2}Zr_{0.7}Y_{(0.1-\xi)}Ni_{\xi}O_{(3-\delta)}$.* Solid State Ionics, 2011. **185**(1): p. 11-17.
39. Norby, T. and Y. Larring, *Concentration and transport of protons in oxides.* Current Opinion in Solid State and Materials Science, 1997. **2**(5): p. 593-599.
40. Tsvetkov, et al., *Thermoelectric Behavior of $BaZr_{0.9}Y_{0.1}O_{3-d}$ Proton Conducting Electrolyte.* Membranes, 2019. **9**(9): p. 120.

41. Zhu, H., et al., *Defect Incorporation and Transport within Dense $BaZr_{0.8}Y_{0.2}O_{3-\delta}$ (BZY20) Proton-Conducting Membranes.* Journal of The Electrochemical Society, 2018. **165**(9): p. F581-F588.
42. Grover, W., *Co-Ionic Conduction in Protonic Ceramics of the Solid Solution, $BaCe_{(x)}Zr_{(y-x)}Y_{(1-y)}O_3$-Ω Part II: Co-Ionic Conduction*, in *Advances in Ceramics - Synthesis and Characterization, Processing and Specific Applications*. 2011, InTech.
43. Wang, W. and A.V. Virkar, *Ionic and electron–hole conduction in $BaZr_{0.93}Y_{0.07}O_{3-\delta}$ by 4-probe dc measurements.* Journal of Power Sources, 2005. **142**(1-2): p. 1-9.
44. Bohn, H.G. and T. Schober, *Electrical Conductivity of the High-Temperature Proton Conductor $BaZr_{0.9}Y_{0.1}O_{2.95}$.* Journal of the American Ceramic Society, 2004. **83**(4): p. 768-772.
45. Kim, I.-H., et al., *Determination of partial conductivities and computational analysis of the theoretical power density of $BaZr_{0.1}Ce_{0.7}Y_{0.1}Yb_{0.1}O_{3-\delta}$ (BZCYYb1711) electrolyte under various PCFC conditions.* Journal of Materials Chemistry A, 2019. **7**(37): p. 21321-21328.
46. Gerhardt, R., *Impedance and dielectric spectroscopy revisited: Distinguishing localized relaxation from long-range conductivity.* Journal of Physics and Chemistry of Solids, 1994. **55**(12): p. 1491-1506.
47. León, C., et al., *Origin of Constant Loss in Ionic Conductors.* Physical Review Letters, 2001. **86**(7): p. 1279-1282.
48. Rivera, A., et al., *Origin and properties of nearly constant loss in crystalline and glassy ionic conductors.* Journal of Non-Crystalline-Solids, 2002. **307-310**.
49. Iguchi, E., et al., *Ionic conduction due to oxygen diffusion in $La_{0.8}Sr_{0.2}GaO_{3-\delta}$ electrolyte.* Journal of Applied Physics, 2003. **93**(6): p. 3662-3664.
50. Kurumada, M., H. Hara, and E. Iguchi, *Oxygen vacancies contributing to intragranular electrical conduction of yttria-stabilized zirconia (YSZ) ceramics.* Acta Materialia, 2005. **53**(18): p. 4839-4846.
51. Anirban, S. and A. Dutta, *Structure, ionic transport properties and ion dynamics of $Ce_{0.8}Y_{0.2}O_{1.9}$ oxygen ion conductor: Understanding the impact of sintering temperature.* Journal of Solid State Chemistry, 2021. **303**: p. 122451.
52. Singh, K., A.K. Baral, and V. Thangadurai, *Grain Boundary Space Charge Effect and Proton Dynamics in Chemically Stable Perovskite-Type $Ba_{0.5}Sr_{0.5}Ce_{0.6}Zr_{0.2}Gd_{0.1}Y_{0.1}O_{3-\delta}$.* Journal of the American Ceramic Society, 2016. **99**(3): p. 866-875.
53. Islam, M.S., et al., *Doping and defect association in AZrO3(A = Ca, Ba) and LaMO3(M = Sc, Ga) perovskite-type ionic conductors.* Dalton Transactions, 2004(19): p. 3061.
54. Björketun, M.E., P.G. Sundell, and G. Wahnström, *Effect of acceptor dopants on the proton mobility in$BaZrO_3$: A density functional investigation.* Physical Review B, 2007. **76**(5).
55. Norby, T. and P. Kofstad, *Electrical Conductivity and Defect Structure of Y_2O_3 as a Function of Water Vapor Pressure.* Journal of the American Ceramic Society, 1984. **67**(12): p. 786-792.
56. Chevalier, J., et al., *The Tetragonal-Monoclinic Transformation in Zirconia: Lessons Learned and Future Trends.* Journal of the American Ceramic Society, 2009. **92**(9): p. 1901-1920.
57. Schmidt-Whitley R D, M.-C.M.a. and R. A, *Growth and microstructural control of single crystal cuprous oxide Cu_2O.* J. Cryst. Growth, 1974. **23**: p. 113-120.
58. Shufang Nie, Y.L., Qiong Liu, Meili Wang, Hejin Wang *Phase transitions and thermal expansion of $BaCO_3$ and $SrCO_3$ up to 1413 K.* European Journal of Mineralogy, 2017. **29**: p. 433-443.

59. Tsubakino, H., M. Hamamoto, and R. Nozato, *Tetragonal-to-monoclinic phase transformation during thermal cycling and isothermal ageing in yttria-partially stabilized zirconia.* 1991. **26**(20): p. 5521-5526.
60. Muccillo, R., et al., *Thermal analyses of yttrium-doped barium zirconate with phosphor pentoxide, boron oxide and zinc oxide addition.* Journal of Thermal Analysis and Calorimetry, 2017. **130**(3): p. 1791-1799.
61. Babilo, P., T. Uda, and S.M. Haile, *Processing of yttrium-doped barium zirconate for high proton conductivity.* Journal of Materials Research, 2007. **22**(5): p. 1322-1330.
62. Rowberg, A.J.E., L. Weston, and C.G. Van De Walle, *Optimizing Proton Conductivity in Zirconates through Defect Engineering.* ACS Applied Energy Materials, 2019. **2**(4): p. 2611-2619.
63. Ricote, S., et al., *Effects of the fabrication process on the grain-boundary resistance in* $BaZr_{0.9}Y_{0.1}O_{3-\delta}$. J. Mater. Chem. A, 2014. **2**(38): p. 16107-16115.
64. Chen, C.-T., C.E. Danel, and S. Kim, *On the origin of the blocking effect of grain-boundaries on proton transport in yttrium-doped barium zirconates.* Journal of Materials Chemistry, 2011. **21**(14): p. 5435.

9 Appendix A: Derivations and expressions

9.1 Python Code for numerical solution of space charge potentials

```
import numpy as np
import matplotlib.pyplot as plt
from scipy.optimize import fsolve
from scipy.constants import e, k

# Known values

T = 573.15  #Abs temperature
Y = 42.38837649 #conductivity (bulk/GB_spesific)
k_b=k/e #boltzmann constant in eV/K

#Defining the function

func = lambda phi : (((np.exp(phi/(k_b*T)))/((2*phi)/(k_b*T))) - Y)

# Plot to check phi(0) graphically

phi = np.linspace(-0.1, 0.5, 101)

plt.plot(phi, func(phi))
plt.xlabel("phi")
plt.ylabel("expression value")
plt.grid()
plt.show()

# Using the numerical solver from scipy to find exact phi(0) value

phi_initial_guess = 0.5 #initial guess found in graphical assessment
phi_solution = fsolve(func, phi_initial_guess)

print("Solution for phi = %f" % phi_solution)
print("Value of expression is %f" % func(phi_solution))
```

9.2 Derivation of proton concentration

$$K_{hydr} = \frac{[OH_O^{\cdot}]^2}{p_{H_2O}[v_O^{\cdot\cdot}][O_O^x]} \tag{1}$$

$$[O_O^x] = 3 - [v_O^{\cdot\cdot}] - [OH_O^{\cdot}] \tag{1.1}$$

$$[v_O^{\cdot\cdot}] = \frac{(S - [OH_O^{\cdot}])}{2} \tag{1.2}$$

Here S is the effective acceptor concentration. Putting (1.1) and (1.2) into the equilibrium expression:

$$K_{hydr} = \frac{[OH_O^{\cdot}]^2}{p_{H_2O}\left(3 - \frac{S - [OH_O^{\cdot}]}{2} - [OH_O^{\cdot}]\right)\left(\frac{S - [OH_O^{\cdot}]}{2}\right)} \tag{2}$$

Solving for $[OH_O^{\cdot}]$ as x, where $K_{hydr} = K, p_{H_2O} = p$ for simplicity:

$$K = \frac{x^2}{p\left(3-\frac{S-x}{2}-x\right)\left(\frac{S-x}{2}\right)} \tag{3}$$

$$K = \frac{4x^2}{p(6-(S-x)-2x)(S-x)} \tag{4}$$

$$4x^2 = pK(6 - S - x)(S - x) \tag{5}$$

$$4x^2 = pK(6S - 6x - S^2 + Sx - Sx + x^2) \tag{6}$$

$$4x^2 = 6pKS - 6pKx - pKS^2 + pKx^2 \tag{7}$$

$$0 = 6pKS - 6pKx - pKS^2 + pKx^2 - 4x^2 \tag{8}$$

$$0 = x^2(pK - 4) - 6pKx + (6pKS - pKS^2) \tag{9}$$

$$0 = x^2 - \frac{6pKx}{pK-4} + \frac{6pKS-pKS^2}{pK-4} \tag{10}$$

$$x^2 - \frac{6pKx}{pK-4} = \frac{(pKS^2-6pKS)}{pK-4} \tag{11}$$

Where $pK = A$ for simplicity:

$$x^2 - \frac{6Ax}{A-4} = \frac{(AS^2-6AS)}{A-4} \tag{12}$$

Adding in $\frac{9A^2}{(A-4)^2}$ to both sides:

$$x^2 - \frac{6Ax}{A-4} + \frac{9A^2}{(A-4)^2} = \frac{(AS^2-6AS)}{A-4} + \frac{9A^2}{(A-4)^2} \tag{13}$$

The left side can be written as a square $\left(x - \frac{3A}{A-4}\right)^2$:

$$\left(x - \frac{3A}{A-4}\right)^2 = \frac{(AS^2-6AS)}{A-4} + \frac{9A^2}{(A-4)^2} \tag{14}$$

$$x - \frac{3A}{A-4} = \pm\sqrt{\frac{AS^2-6AS}{A-4} + \frac{9A^2}{(A-4)^2}} \tag{15}$$

Only the positive of the square root is applicable for obtaining real values for x:

$$x = \frac{3A}{A-4} + \sqrt{\frac{AS^2-6AS}{A-4} + \frac{9A^2}{(A-4)^2}} \tag{16}$$

$$x = \frac{3A}{A-4} + \sqrt{\frac{(AS^2-6AS)*(A-4)}{(A-4)^2} + \frac{9A^2}{(A-4)^2}} \quad (17)$$

$$x = \frac{3A+\sqrt{(AS^2-6AS)*(A-4)+9A^2}}{A-4} \quad (18)$$

$$x = \frac{3A+\sqrt{A^2S^2-4AS^2-6A^2S+24AS+9A^2}}{A-4} \quad (19)$$

$$x = \frac{3A+\sqrt{A(AS^2-4S^2-6AS+24S+9A)}}{A-4} \quad (20)$$

The final answer with all the constants untangled:

$$[OH_O^{\cdot}] = \frac{3K_{hydr}p_{H_2O}+\sqrt{K_{hydr}p_{H_2O}\left(9K_{hydr}p_{H_2O}-6K_{hyd}p_{H_2O}S+K_{hydr}p_{H_2O}S^2+24S-4S^2\right)}}{K_{hydr}p_{H_2O}-4} \quad (21)$$

10 Appendix B: Supplementary results

10.1 Relative densities

Table S 1: Relative densities of samples that remained in a cylindrical measurable body.

Sample	**Relative density %** **(* mean value of two samples)**
BSZCYNi05	95.6*
BSZCYCu05	96.9*
BS(YSZ)CYNi05	92.3*
BS(YSZ)CYCu05	89.0*
BSZCYNi1	95.2*
BSZCYCu1	95.4*
BSZCY1600Ni1	95.9
BSZCY1600Cu1	93.6
BSZ(YSZ)CYNi05* (~14mol% yttrium)	95.5*
BSZ(YSZ)CYNi05(O2)* (~14mol% yttrium)	88.7*
BSZCYNi1(O2)	98.5
BSZCYCu1(O2)	91.6

10.2 Dilatometry

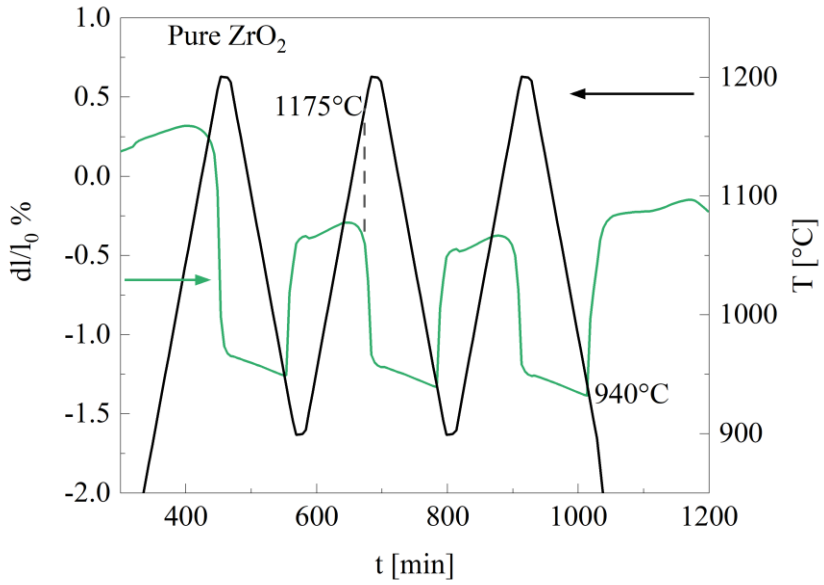

Figure S 1: Pure pre-sintered zirconia sample cycled between expected phase transition temperature.

10.3 SEM

For the thermally etched samples BS(YSZ)CYNi05(O2)* and BSZCYNi1 the grain diameter was obtained from sampling four different areas of the middle part of the polished cross section, with one representation presented along with the grain diameter distribution results in Figure S 2 and Figure S 3.

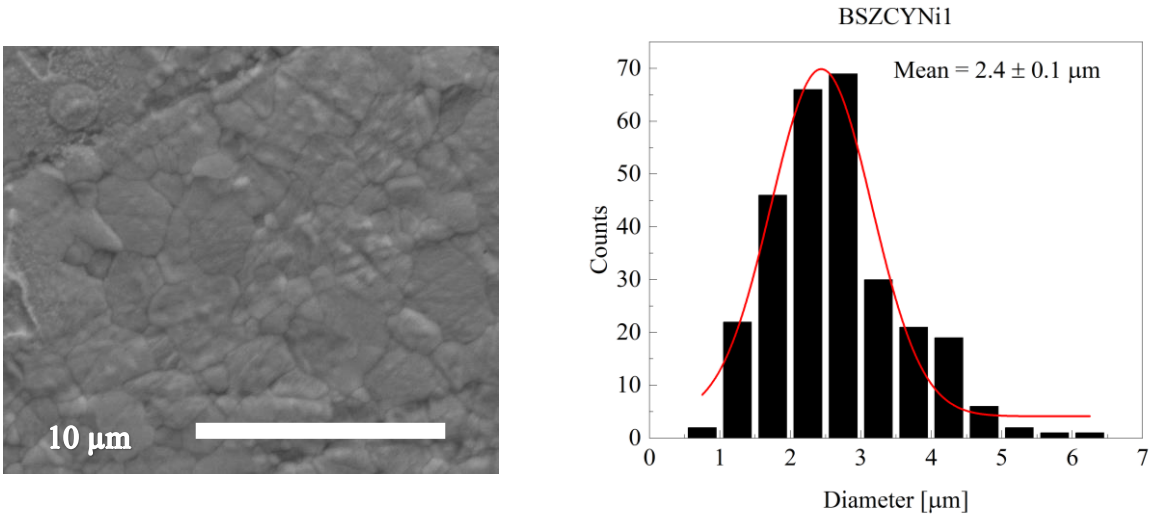

Figure S 2: Grain diameter distribution with Gaussian fit to determine mean value for BSZCYNi1.

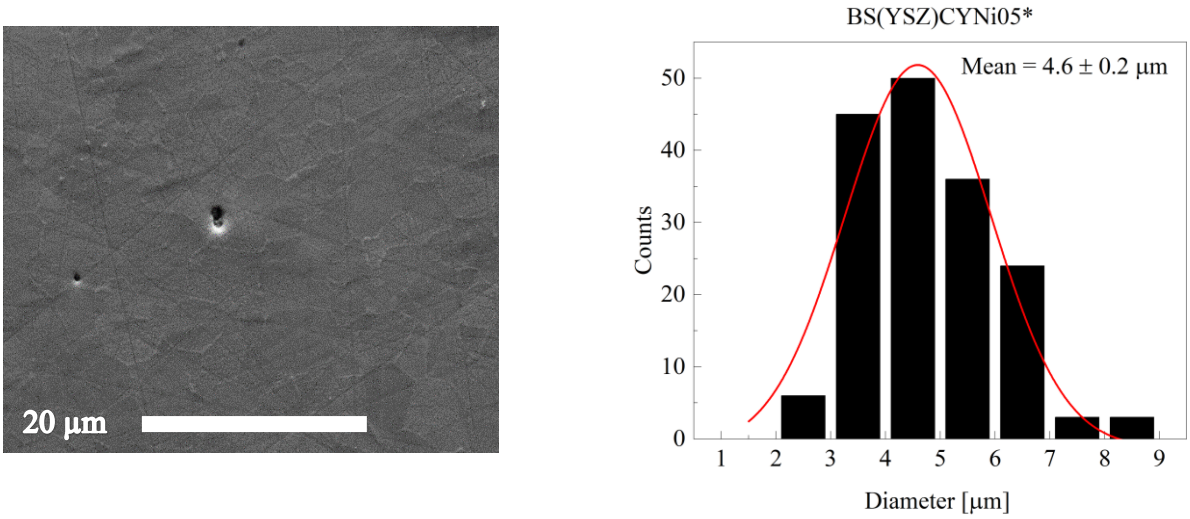

Figure S 3: Grain diameter distribution with Gaussian fit to determine mean value for BS(YSZ)CYNi05(O2)*.

10.4 HT-XRD

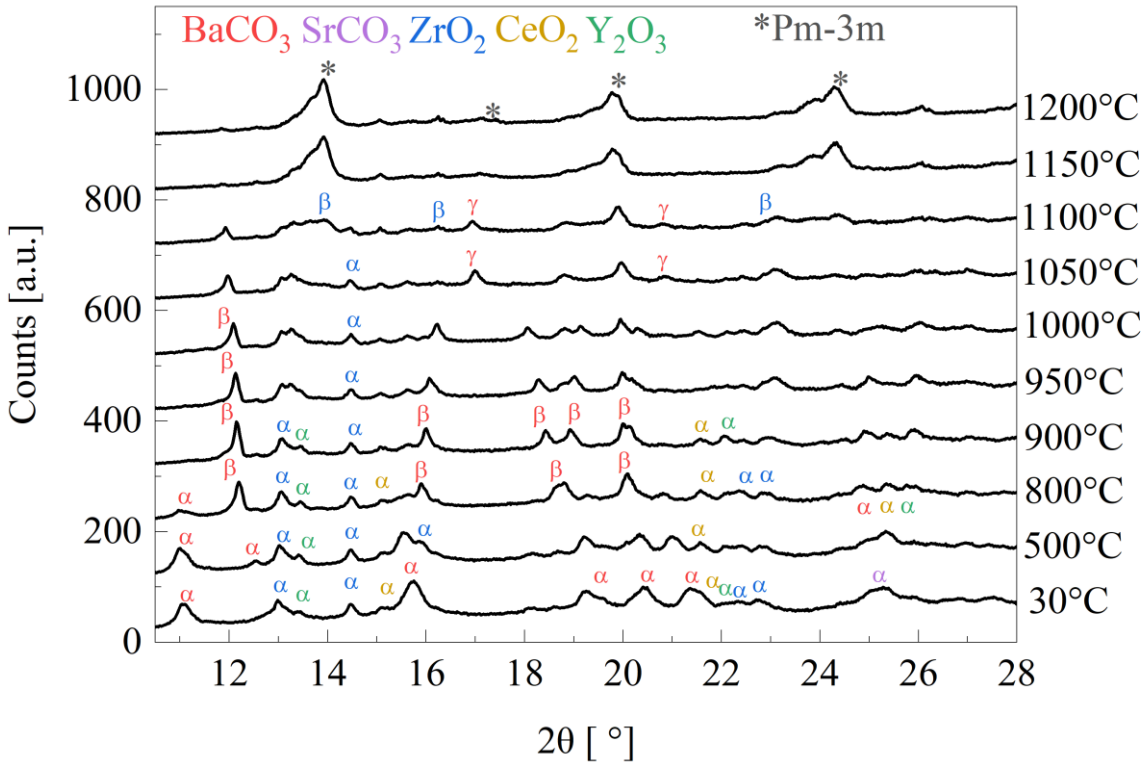

Figure S 4: Selected temperatures from HT-XRD measurement of green powders. Peaks are attributed phases colour coded with respect to the precursors.

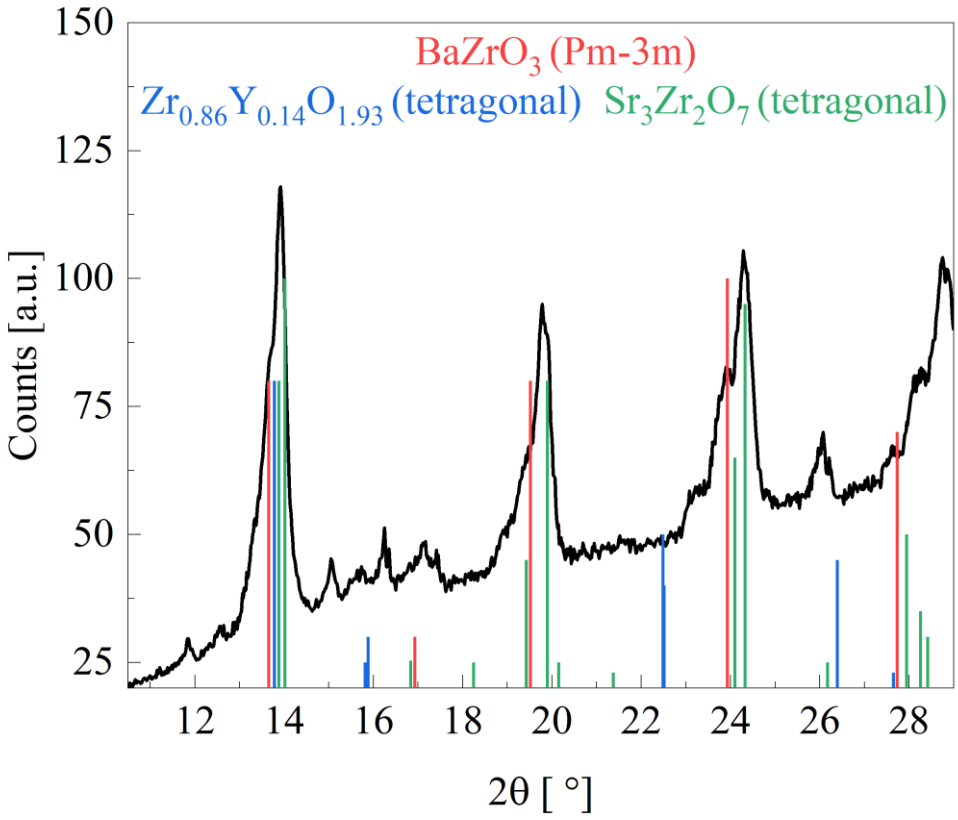

Figure S 5: XRD pattern at 1200°C with probable phases of tetragonal structures included from PDF data base.

Table S 2: PDF files used to identify phases in the HT-XRD.

Precursor	Phases	PDF/COD #
$BaCO_3$	α-$BaCO_3$	PDF 00-002-0364
	β-$BaCO_3$	COD 1539129
	γ-$BaCO_3$	PDF 00-011-0697
$SrCO_3$	α-$SrCO_3$	PDF 01-071-2393
ZrO_2	α-ZrO_2	PDF 00-001-0750
	β-ZrO_2	PDF 00-002-0733

CeO_2	α-CeO_2	PDF 00-001-0800
Y_2O_3	α-Y_2O_3	PDF 00-001-0831
$Zr_{0.84}Y_{0.16}O_{1.92}$	--	PDF 01-082-1244

10.5 Hydration thermodynamics from TG data

Table S 3: Hydration thermodynamics extracted with van't Hoff linear regression from TG data.

Sample	ΔH_{hydr}° $[kJ\ mol^{-1}]$	ΔS_{hydr}° $[J\ K^{-1} mol^{-1}]$	$S\%$	R^2
BSZCY1400	-78.6	-98.4	9.34	0.9891
BSZCY1600	-80.9	-104.6	8.65	0.9984
BSZCYNi1	-106.5	-124.8	7.67	0.9980
BSZCYCu1	-99.3	-118.2	7.15	0.9992
BSZCY1600Ni1	-86.6	-107.7	6.10	0.9959
BSZCY1600Cu1	-86.8	-105.1	10.30	0.9998
BS(YSZ)CY1600*	-81.9	-97.6	11.25	0.9996
BS(YSZ)CYNi05*	-90.2	-104.0	9.12	0.9983
BSZCYNi1(O2)	-99.1	-110.5	12.75	0.9979
BSZCYCu1(O2)	-93.9	-108.0	10.07	0.9956
BSZCY	-79.8	-93.4	12.98	0.9989
BS(YSZ)CY	-80.2	-94.5	10.69	0.9991

BSZCYNi05	-84.5	-98.5	10.65	0.9940
BS(YSZ)CYNi05	-81.9	-95.0	10.45	0.9941
BSZCYCu05				
BS(YSZ)CYCu05	-72.8	-84.0	13.65	0.9952

Table S 4: Hydration thermodynamics extracted from multi equation fitting (*Table Curve 2D*)

Sample	ΔH_{hydr}° $[kJ\ mol^{-1}]$	ΔS_{hydr}° $[J\ K^{-1} mol^{-1}]$	$S\%$	R^2
BSZCY1400	-75.8	-94.0	9.10	0.9971
BSZCY1600	-82.3	-106.2	8.58	0.9997
BSZCYNi1	-114.0	-132.1	7.38	0.9965
BSZCY1600Ni1	-95.8	-116.7	5.67	0.9979
BSZCYCu1	-108.9	-127.9	6.77	0.9932
BSZCY1600Cu1	-89.8	-108.1	9.99	0.9994
Pristine w/YSZ* 1600°C – 12h	-82.1	-97.8	11.25	0.9997

10.6 Activation energies from conductivity data

The values presented in Table S 5 and Table S 6 have a maximum standard deviation of $\pm 5\ kJ\ mol^{-1}$, but usually lower.

Table S 5: Activation energies obtained by linear regression from conductivity in humid argon at different temperature intervals for BSZCYNi1 and BSZCYCu1.

Sample	**Bulk $kJ\ mol^{-1}$**		**Grain Boundary $kJ\ mol^{-1}$**		**Total $kJ\ mol^{-1}$**	
T [°C]	100-400	100-700	100-400	100-700	100-400	100-700
BSZCYNi1	58	56	73	71	66	62
BSZCYCu1	57	49	75	72	74	65

Table S 6: Activation energies obtained by linear regression from conductivity in humid argon at different temperature intervals for BS(YSZ)CYCu05.

Sample	**Bulk $kJ\ mol^{-1}$**		**Grain Boundary $kJ\ mol^{-1}$**		**Total $kJ\ mol^{-1}$**	
T [°C]	55-400	55-800	55-400	55-800	55-400	55-800
BS(YSZ)CYCu05	63	52	66	66	63	57